

An Optical Sensor Design: Concurrent Multi-axis Force Measurement and Tactile Perception

by

Wanlin Li

A dissertation submitted to
The School of Electronic Engineering and Computer Science
in partial fulfilment of the requirements for the Degree of
Doctor of Philosophy
in the subject of
Robotics

Queen Mary University of London
Mile End Road
E1 4NS, London, UK

September, 2020

Abstract

Force and tactile sensing have experienced a surge of interest over recent decades, as they convey useful information about the direct physical interaction between the sensor and the external environment. A robot end effector is a device designed to interact with the environment. End effectors such as robotic hands and grippers can be used to pick up, place or generally manipulate objects. There is a clear need to equip such end effectors with appropriate sensing means to be able to measure tactile and force information. Work to date has explored these two modalities separately. Tactile sensors have been developed for integration with gripper fingertips or as skins embedded with the outer side of manipulators, mainly to measure normal force and its distribution across a surface patch. On the other hand, force sensors have commonly been integrated with the joints of robotic arms or fingers to measure external multi-axis forces and torques via the connected links.

We observe that a force sensor cannot measure tactile information, and current tactile sensors cannot accurately measure force information. This can become a particular issue when integrating force sensors remotely to measure forces indirectly, especially if the connecting link is flexible or, generally, difficult to model potentially impacting negatively on the force estimates. We aim to provide a solution for an integrated sensor capable of measuring tactile and force information at the point of contact, i.e., on the fingertip of a robot hand or arm.

In this thesis, we explore the idea of integrating the two sensing modalities, tactile and force sensing, in one sensor housing with the signal acquisition being performed by a single monocular camera acting as the transducer. The hypothesis is that an integrated force/tactile sensor will perform in a better way than having these sensor modalities separated. This thesis shows that an integrated sensor achieves a tactile sensing performance comparable to existing vision-based tactile sensors and at the same time proves to provide more accurate force sensor information whilst extending the field of similar vision-based sensors from 3 DoF to 6 DoF. In addition,

the tactile sensing element of our sensor is not affected by the patterns superimposed on to the flexible element of comparable vision-based sensors used to infer force information. In this thesis, we have implemented several sensor prototypes; designs and experimental analyses for each prototype are being provided. The manufactured sensor prototypes prove the validity of the proposed vision-based dual-modality sensing approach, and the proposed sensing principle and structure shows high versatility and accuracy, as well as the potential for further miniaturization, making the proposed concept suitable for integration with standard robot end effectors.

Declaration

I, Wanlin Li, confirm that the research included in this thesis is my work, that is duly acknowledged, and my contributions are indicated. I have also acknowledged previously published materials.

I attest that reasonable care has been exercised to ensure the originality of this work, and to the best of my knowledge does not break any UK law, infringe any third party's copyright or other intellectual property rights, or contain any confidential material.

I accept that the college has the right to use plagiarism detection software to check the electronic version of the thesis.

I confirm that this thesis has not been previously submitted for the award of a degree to any other university.

The copyright of this thesis rests with the author and no quotation from it or information derived from it may be published without the prior written consent of the author.

Signature: Wanlin Li

Date: August 22, 2020

Acknowledgements

First of all, I would like to express my thanks to my two joint supervisors, Prof. Kaspar Althoefer from the Centre for Advanced Robotics @ Queen Mary (ARQ) and Dr. Akram Alomainy from Antennas and Applied Electromagnetics, Queen Mary University of London. Both of them have jointly supervised my research during my PhD. I would like to thank to Prof. Kaspar for drawing my attention to the force and tactile sensing field, guiding me with a clear direction and supporting all the experiments I made. I would like to thank Dr. Akram for fully supporting my research concerning sensor building, as well as providing facilities for my experiments. I would also like to thank Dr. Khalid Rajab from the Queen Mary University of London, my independent assessor, for guiding me at the initial stage of my PhD career. Without all their guidance, I could not have completed my PhD research.

I would like to thank the help and support from my colleagues and lecturers at the Centre for Advanced Robotics @ Queen Mary. Especially I am grateful to Dr. Lorenzo Jamone, Dr. Ildar Farkhatdinov, Dr. Ketao Zhang, Dr. Ivan Vitanov, Dr. Hareesh Godaba, Dr. Claudio Coppola, Jan Fr s, Faisal Aljaber, Luis Andres Puertolas Balint, Taqi Abrar, Fabrizio Putzu, Ahmad Ali, Ahmed Hassan, Abu Bakar Dawood, Joshua Brown, Ata Otaran, Francesca Palermo, Gokhan Solak, Brice Denoun for helping me with my PhD work.

I would also like to thank Dr. Yohan Noh from Brunel University, and Dr. Jelizaveta Konstantinova from Ocado Technology, for helping me with the sensor development, and Dr. Peng Qi from Tongji University for his patience and encouragement during our collaborative work.

I would like to take this opportunity to thank my parents, Dr. Junsheng Li and Dr. Xiaolan Zhang, for their love throughout my entire life, and I am deeply thankful to Dr. Xinyuan Qian who is always by my side and makes my life sweet.

Published work

Journal paper

- [J1] **W. Li**, A. Alomainy, I. Vitanov, Y. Noh, P. Qi, K. Althoefer, “F-TOUCH Sensor: Concurrent Geometry Perception and Enhanced Force Measurement”, accepted in *IEEE Sensors Journal* 2020.

Conference paper(s)

- [C1] **W. Li**, Y. Noh, A. Alomainy, I. Vitanov, Y. Zheng, P. Qi, K. Althoefer, “F-TOUCH Sensor for Three-Axis Forces Measurement and Geometry Observation”, accepted in *IEEE Sensors Conference* 2020.
- [C2] X. Li, **W. Li**, Y. Zheng, K. Althoefer, Peng. Qi, “Criminisi Algorithm Applied on to a GelSight Fingertip Sensor for Multi-modality Perception”, accepted in *2020 IEEE/ASME International Conference on Advanced Intelligent Mechatronics (AIM 2020)*.
- [C3] **W. Li**, J. Konstantinova, Y. Noh, A. Alomainy, K. Althoefer, “Elastomer-Based Touch Sensor: Visualization of Tactile Pressure Distribution”, in *Annual Conference Towards Autonomous Robotic Systems*, pp. 87-98. Springer, Cham, Jul 2019.
- [C4] **W. Li**, J. Konstantinova, Y. Noh, Z. Ma, A. Alomainy, K. Althoefer, “An Elastomer-based Flexible Optical Force and Tactile Sensor”, in *2019 2nd IEEE International Conference on Soft Robotics (RoboSoft)*, pp. 361-366. IEEE, Apr 2019.
- [C5] **W. Li**, J. Konstantinova, Y. Noh, A. Alomainy, K. Althoefer, “Camera-based force and

- tactile sensor”, in *Annual Conference Towards Autonomous Robotic Systems*, pp. 438-450. Springer, Cham, Jul 2018.
- [C6] **W. Li**, K. Rajab, K. Alhoefer, B. Zupancic, J. Barras, “Broadband matching of nuclear quadrupole resonance detector using non-Foster circuits”, in *2016 Loughborough Antennas Propagation Conference (LAPC)*, pp. 1-5. IEEE, Nov 2016.
- [C7] D. Osman, X. Du, **W. Li**, Y. Noh, “An Optical Joint Angle Measurement Sensor based on an Optoelectronic Sensor for Robotic Manipulators”, accepted in *2020 International Conference on Control, Mechatronics and Automation (ICCMA2020)*.
- [C8] Y. Noh, L. Lindenroth, S. Wang, R. Housden, A. Wingerden, **W. Li**, K. Rhode, “A 2-piece six-axis force/torque sensor capable of measuring loads applied to tools of complex shapes”, in *2019 IEEE/RSJ International Conference on Intelligent Robots and Systems (IROS)*, pp. 7976-7981. IEEE, Nov 2019.
- [C9] Y. Noh, S. Han, P. Gawenda, **W. Li**, S. Sareh, K. Rhode, “A Contact Force Sensor based on S-shaped Beams and Optoelectronic Sensors for Flexible Manipulators for Minimally Invasive Surgery (MIS)”, in *IEEE Sensors Journal*, vol. 20, no. 7, pp. 3487-3495. IEEE, Oct 2019.
- [C10] J. Koh, T. Jeong, S. Han, **W. Li**, K. Rhode, Y. Noh, “Optoelectronic Sensor-based Shape Sensing Approach for Flexible Manipulators”, in *2019 41st Annual International Conference of the IEEE Engineering in Medicine and Biology Society (EMBC)*, pp. 3199-3203. IEEE, Jul 2019.

Contents

Abstract	ii
Declaration	iv
Acknowledgements	v
Published work	vi
1 Introduction	1
1.1 Overview and Motivation	1
1.2 Aim and Objectives	3
1.3 Contributions	4
1.4 Thesis Outline	7
2 Background	9
2.1 Introduction	9
2.2 Background of Robotic Force and Tactile Systems	11
2.3 Review of Multi-Axis Force Sensors	15
2.3.1 Strain Sensing Technology	16
2.3.2 Three DOF Cross-beam Sensing Technology	19
2.3.3 Six DOF Cross-beam Sensing Technology	20
2.3.4 Stewart Platform Sensing Technology	25
2.3.5 Optical-based Sensing Technology	27
2.4 Review of Tactile Sensors	32

2.4.1	Resistance-based Sensing Technology	34
2.4.2	Capacitance-based Sensing Technology	37
2.4.3	Piezoelectricity-based Sensing Technology	39
2.4.4	Organic Field-effect Transistors (OFETs) Sensing Technology	41
2.4.5	Magnetic-based Sensing Technology	42
2.4.6	Optical-based Sensing Technology	44
2.5	Summary	50
3	Dual-Modality Sensor Methodology	52
3.1	Introduction	52
3.2	Dual-Modality Sensor Methodology	53
3.2.1	Robotic Force and Tactile Sensing System	53
3.2.2	Dual-Modality Sensing Principle	54
3.3	Concurrent Real-time Dual-Modality Sensing Using A Single Camera	62
3.4	Miniaturisation of Dual-Modality Sensor	67
3.5	Summary	68
4	Sensor Design, Prototyping and Analysis	70
4.1	Introduction	70
4.2	ICFTS — Initial Camera-based Force/Tactile Sensor	71
4.2.1	Introduction	71
4.2.2	Sensor Design	72
4.2.3	Sensor Prototype Evaluation	77
4.2.4	Summary	84
4.3	CTS — Camera-based Tactile Sensor	84
4.3.1	Sensor Design	85
4.3.2	Working Principle of the Optical-based Tactile Sensor	92
4.3.3	Summary	94

4.4	CFTS — Camera-based Force/Tactile Sensor	94
4.4.1	Sensor Design and Development	95
4.4.2	Summary	101
4.5	F-TOUCH Sensor — Force and Tactile Optically Unified Coherent Haptics Sen- sor	103
4.5.1	Sensor Design	104
4.5.2	Summary	121
4.6	Summary of the Chapter	122
5	Experimental Validation of Sensor Performance	123
5.1	Introduction	123
5.2	CTS — Camera-based Tactile Sensor	123
5.2.1	Visualization of Tactile Information	124
5.2.2	Summary	128
5.3	CFTS1 — Camera-based Force/Tactile Sensor	128
5.3.1	Sensor Calibration and Evaluation	129
5.3.2	Visualization of Tactile Information	133
5.3.3	Simultaneous Force and Tactile Sensing	135
5.3.4	Summary	136
5.4	F-TOUCH Sensor — Force and Tactile Optically Unified Coherent Haptics Sensor	137
5.4.1	Three-Axis Forces Calibration and Evaluation	140
5.4.2	Six-Axis Forces Calibration and Evaluation	144
5.4.3	Summary	149
6	Conclusion and Future Work	151
6.1	Summary	152
6.2	Future Work and Directions	154

References**156**

List of abbreviations

ABS	acrylonitrile butadiene styrene
ANN	artificial neural networks
BH	blind hole
CAD	computer-aided design
CCD	charge-coupled device
CFTS	Camera-based Force/Tactile Sensor
CNN	convolutional neural network
CNT	carbon nanotube
CTS	Camera-based Tactile Sensor
DAQ	data acquisition
DL	deep learning
DNN	deep neural network
DOF	Degrees of Freedom
EM	electromagnetic
ERSGs	electrical resistance strain gauges
F-TOUCH	Force and Tactile Optically Unified Coherent Haptics

F/T	Force/Torque
FBGs	Fibre Bragg Gratings
FEA	finite element analysis
FoV	field of view
fps	frame per second
GF	gauge factor
GMMR	Gaussian mixture model regression
GMR	magneto-resistance
GT	ground truth
HCI	Human Robot Interaction
HDT	heat deflection temperature
ICFTS	Initial Camera-based Force/Tactile Sensor
IR	InfraRed
ISO	International Standard Organization
LED	light emitting diode
LMS	least mean square
MEMS	micro-electro-mechanical systems
MIRS	minimally invasive robotic surgery
MIS	minimally invasive surgery

MLR	multiple linear regression
MR	magnetic resonance
MRI	magnetic resonance imaging
OFETs	Organic Field-Effect Transistors
PCB	printed circuit board
PDMS	polydimethylsiloxane
PDs	photo detectors
PLA	polylactic acid
PPS	pressure profile systems
PVDF	polymer polyvinylidene fluoride
RMSE	root mean square error
ROS	robot operation system
RPM	revolutions per minute
RS	reflective surface
SMD	surface-mount-device
SoA	State-of-the-Art
SSGs	semiconductor strain gauges
TH	through hole

List of symbols

(x, y, z)	world coordinates
ν	Poisson's ratio
ρ	SSGs material resistivity
Σ	sum operator
ε	strain
ε_0	permittivity of free space
ε_r	permittivity of dielectric material
B	blue value of each pixel
C_p	capacitance
F_x	the force along the x -axis
F_y	the force along the y -axis
F_z	the force along the z -axis
G	green value of each pixel
I	current
i	target identity label
N	the total numerical value of the pixels in each sensing area
n	numerical value of each pixel
R	electrical resistance
R	red value of each pixel

t	time index
T_c	temperature
T_x	the torque along the x –axis
T_y	the torque along the y –axis
T_z	the torque along the z –axis
V	voltage

Chapter 1

Introduction

1.1 Overview and Motivation

The rise and expansion of smart industries has been accompanied by a rapidly growing demand for robot technology. Nowadays, the expectation is to bring robots closer to the human in the factory environment. Thus the development of collaborative robotic systems has advanced at high speed over the past ten years. Most if not all electronic devices and appliances, from mobile phones and laptops to vacuum cleaners and refrigerators are assembled on an automated production line [84]. In the case of vehicles, the entire production of cars where the entire manufacturing process can be achieved by automation using robots and assembly machines [18]. In the medical field, surgical robots [143] play a very important role during surgery as they enable the medical operators to execute very precise interactions, such as small size incision [14], stent insertion [28], etc. One can observe that machines are more time-efficient and can even perform more precise work than humans. However, current robots are not that "smart" - the majority of the manipulation tasks within the manufacturing are repetitive and easily programmed. In order to operate more complicated tasks, robots need to well-perceive the environment and react to it when changes occur [74]. These reactions which may come quite natural to humans, can be

very hard for a robot to achieve.

Sensor technology is a prerequisite if robots are to be able to react to the external environment; especially, force and tactile sensing [152] is one of the research areas that researchers have been putting increasing emphasis on. Force and tactile perceptions are recognized as important sensations for robot structures since they convey useful information about the interaction of the robot body with the external environment. In other words, force and tactile sensors can be regarded as a core device for robots to realize intelligent perception and human-robot interaction (HCI). Currently, different methods and techniques have been applied in realising force and tactile sensors, based on strain gauges [122, 102], cross-beams [171, 77, 48], Stewart platforms [181], optics [16], for force sensors. Sensors based on the principles of resistance [172], capacitance [138, 40], piezoelectricity [87], organic field-effect transistors (OFETs) [33], optics [83] and magnetics [60] have been employed to measure tactile information. Most of these sensors can only sense one modality, that is, they can either measure force or pressure, a fact that makes them single-functional. This thesis argues that the creation of multi-modal sensors will resolve the shortcomings of the current single modality sensors. The proposed dual-modality sensor is capable of unifying these two sensing modalities in one structure.

Of the different force and tactile sensing technologies, optical-based sensors that use cameras have attracted increasing interest, as this type of sensor can provide a high spatial resolution and, most importantly, it is able to sense multiple modalities (such as contact force and contact surface geometry) based on a single captured image [139, 93] - which is a significant advantage comparing with other tactile sensing techniques. In the past, the camera-based sensors were hindered by the large size of cameras, but nowadays, this disadvantage has been gradually overcome with the development of small-sized cameras. Vision-based optical tactile sensors usually use soft and deformable materials [20, 69] as the sensing medium. The deformation of the material can be directly monitored through the camera or by observing changes to certain patterns on the sensing medium (as an indirect way) to acquire tactile information. Elastomeric materials offer compliance, which gives the tactile sensor the ability to adapt to the curved or irregular surfaces

during manipulation of objects [120]. For instance, a compliant tactile sensor [43] mounted on a fingertip or an end-effector of a robot is useful for grasping different types of objects. However, there are also challenges for developing such a multi-modality sensor. As these multi-modalities can be correlated, we need to figure out a method to separate each modality from the others to avoid unwanted interference. This thesis proposes a new optical vision-based force and tactile sensing method to achieve dual-modality information acquirement and effective ways to separate one modality from the other.

1.2 Aim and Objectives

Aim: This thesis aims to develop a novel methodology for combining multi-axis force measurements and tactile information perception within one optical vision-based sensor so that the sensing device can achieve dual-modality perception, that is contact force measurement in x -, y -, and z - directions, and the perception of the surface geometry of the touched object. The proposed concept is named as F-TOUCH (Force and Tactile Optically Unified Coherent Haptics) sensor.

Objectives: To this aim the thesis will:

1. Investigate and propose an optical vision-based sensing scheme that can achieve concurrent multi-axis force/torque measurement and tactile information perception within one sensor.
2. To miniaturise the proposed sensor so that the resultant structure is compatible with standard robot end effectors.
3. To, concurrently and in real-time, measure six-axes Force/Torque (F/T) information and perceive contact surface geometry.
4. To conduct experimental studies (involving hardware design and software development) to verify the proposed methodology.

1.3 Contributions

The main contributions of this thesis are as follows:

1. Dual-modal sensor for force and tactile sensing in one sensor structure completed
2. The miniaturisation of dual-modality force/tactile sensor for integration with robot arm end effector realised
3. Concurrent and real-time force and tactile sensing using a single camera sensor achieved
4. Extension from normal force measurement to three degrees of freedom forces measurement, to six degrees of freedom forces/torques measurement
5. Experimental study conducted to validate the approach




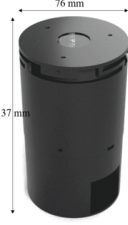



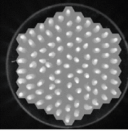
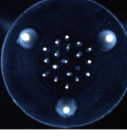
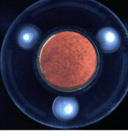
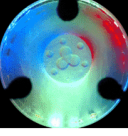
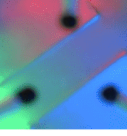
F-TOUCH (Force and Tactile Optically Unified Coherent Haptics) Sensor						
Sensor Prototype						
						
Description	Section 4.2	Section 4.3	Section 4.4	Section 4.4	Section 4.5	Section 4.5
Result	Not shown (This sensor is abandoned)	Section 5.2	Section 5.3	Section 5.3	Not shown (this sensor is further replaced with F-TOUCH_V3.2)	Section 5.4

Figure 1.1: Overview of the proposed force and tactile sensors.

Notably, four generations, six sensor prototypes are developed in this thesis following the proposed optical scheme for dual-modal (force and tactile information) sensing, seen in Fig. 1.1.

They are

1. **ICFTS:** Initial Camera-based Force/Tactile Sensor design using single vision sensor and cone-shaped elastomer;
2. **CTS:** Camera-based Tactile sensor design using cone-shaped elastomer and a cantilever structure;
3. **CFTS:** Camera-based Force/Tactile Sensor that applies multi-cone elastomer structures to measure force and tactile sensing modalities with single camera. Two versions (namely CFTS1 and CFTS2) are presented, where CFTS1 measures pressure and force, and CFTS2 measures texture and force.
4. **F-TOUCH:** Force and Tactile Optically Unified Coherent Haptics sensor on spring-loaded structure for enhanced single-camera-based force and tactile sensing. Two versions (namely F-TOUCH0 and F-TOUCH) are presented, where F-TOUCH is the miniaturised version of F-TOUCH0.

ICFTS is the earliest prototype that tried to sense both force and tactile (texture detection) information within one capture. CTS is then introduced to verify the concept of tactile sensing (pressure detection) using an elastomer (with reflective pins) and a cantilever structure. Then CFTS is introduced (CFTS1 and CFTS2) to implement force measurement functionality upon CTS. Moreover, CFTS1 can detect force and pressure while CFTS2 can detect force and texture. However, one issue of CFTS is that the sensing areas of force and tactile sensing are separate. Therefore, F-TOUCH is introduced (F-TOUCH0 and F-TOUCH) with a vertical hardware layout of an elastomer (on the top) integrated with a spring-mechanism structure (at the bottom), ensuring the whole sensing surface can detect both force and tactile (texture detection) information. Besides, F-TOUCH is the miniaturised version of F-TOUCH0. These three sensors are summarised below:

1. CTS (Camera-based Tactile Sensor)

We present an optical-based tactile sensor that can sense the tactile information in the form of pressure distribution. Our proposed sensor uses a piece of elastomer with reflective conical pins underneath as the touch medium. The elastomer consists of 91 pins arranged in a honeycomb pattern, and each pin can be regarded as a tactile sensing element. Each tactile element transfers the applied pressure value into a circular image pattern which can be captured by a camera. The applied pressure over the sensing array can be computed by processing the area of each sensing element. The sensor surface is reconstructed to visualise the pressure distribution. The experimental results have proven the viability of the sensing concept; the prototype sensor can effectively detect single-point touch as well as multi-points touch.

2. CFTS1 (Camera-based Force/Tactile Sensor)

We present a novel design for an optical-based force and tactile sensing device that senses both force and tactile information within one elastomer. In addition, the tactile information in this sensor is measured in the form of pressure distribution from the surface of objects (same concept as an optical-based tactile sensor). The proposed sensor has a soft and compliant design employing an opaque elastomer. The optical sensing method is used to measure both force and tactile information simultaneously based on the deformation of the reflective elastomer structure and a force-sensitive structure. The experimental evaluation shows that the prototype is capable of sensing normal forces up to 70 N with an error of 6.6% as well as measuring pressure distribution.

3. F-TOUCH (Force and Tactile Optically Unified Coherent Haptics) Sensor

We present a novel sensor architecture that uses one camera to obtain both force and tactile information based on the deformation of a reflective elastomer and a spring mechanism structure. Based on this sensing principle, we miniaturise the sensor into a size (using small camera, silicone elastomer, LEDs and 3D printed parts) that is compatible with the standard robotic gripper, and this is the up-to-date version of our proposed sensor. The ex-

perimental evaluation shows that the prototype is capable of measuring force/torque quantities and capturing the geometry of the contact object surface at the same time. Moreover, we also extend the force measurement capability from one-axis normal force to three-axis forces (F_x, F_y, F_z) , then to six-axis forces and torques $(F_x, F_y, F_z, T_x, T_y, T_z)$. We also develop a unique force calibration method for the proposed sensor. F-TOUCH sensor is inspired by the GelSight tactile sensor. Due to the effectiveness of extracting force-related information from the tactile image (texture), F-TOUCH sensor shows a better multi-axis force measurement capability than the GelSight tactile sensor.

1.4 Thesis Outline

The thesis is organized as follows:

Chapter 1 gives an overview of the project and summarises the motivation, aim and objectives, contributions and gives a thesis outline.

Chapter 2 describes the importance of robotic force and tactile systems, and proceeds to the literature review of currently existed force and tactile sensing technologies, namely strain gauges, three DOF cross-beam force sensor, six DOF cross-beam force sensor, Stewart platform force sensor, optical force sensor, capacitive tactile sensor, electromagnetic tactile sensor, piezoresistive tactile sensor, piezoelectric tactile sensor, piezoelectric sensors, organic field-effect transistors (Organic Field-Effect Transistors (OFETs)) tactile sensors and optical tactile sensors. The chapter concludes with a discussion on dual-modality force and tactile sensor design method, as well as the metric of the proposed sensing method in this thesis.

Chapter 3 describes the overall methodology of the proposed dual-modality force and tactile sensor. The discussion of the theoretical model of the force and tactile sensing is followed by the introduction and analysis of the optical-based dual-modal force and tactile sensing methodology. The sensor architecture uses a single camera and a combination of an elastomer layer and an

elastic structure. Finally, the ways for sensor miniaturisation are analysed.

Chapter 4 introduces the implementation of different proposed sensor prototypes. Several versions of sensor prototypes are presented, from the initial design - ICFTS, to the CTS for pressure visualisation, then to the CFTS series, and finally to the newest design - F-TOUCH series.

Chapter 5 shows the calibration process and the experimental results of three proposed sensor prototypes (CTS, CFTS1 and F-TOUCH) that are described in Chapter 4. Analysis and a comparison between F-TOUCH and the optical-based tactile sensor GelSight (developed at the MCube Lab of Massachusetts Institute of Technology) is presented.

Chapter 6 contains the conclusion and discussion of the thesis, as well as future work directions.

Chapter 2

Background

2.1 Introduction

This chapter provides an overview of the research conducted in the area of force sensing and tactile sensors, especially those that are integrated with the robotics end effector. The importance of force and tactile sensing for robotics is highlighted. With the rapid developments within the robotics field over the past decades, a variety of sensors using different sensing technologies have been produced commercially or are being developed in labs. However, the majority of the research is focused on the development of either force or tactile sensors. A force sensor is used to measure the multi-axis force and torque (3-DoF, 6-DoF); these sensors are considered single-point sensors. Force sensors have the advantage of achieving high-precision force/torque measurements and a wide measuring range, but they cannot measure the force distribution across a surface. A tactile sensor is used to provide tactile information from the surface of an object. Tactile sensors have the advantage of measuring pressure distribution and other forms of tactile information (for example, geometry information). However, they cannot accurately measure multi-axis force and torque values, and often the measuring range is relatively small compared with a force sensor. In this chapter, we will analyse force sensor technologies and tactile sensor

technologies, and propose a new sensor architecture that combines the capabilities of both a force sensor and a tactile sensor within one sensor housing. The sensor architecture is inspired by both the optical-based force sensor (for example the optoforce sensor) and the camera-based tactile sensor (for example the TacTip sensor and the GelSight sensor).

As shown in Fig. 2.1, this chapter firstly introduces the preliminary knowledge of human and robotic force and tactile system in Sec. 2.2. An overview of the currently-used multi-axis force sensing technologies is presented in Sec. 2.3, including strain sensing technology in Sec. 2.3.1, three degree-of-freedom cross-beam sensing technology in Sec. 2.3.2, six degree-of-freedom cross-beam sensing technology in Sec. 2.3.3, Stewart platform sensing technology in Sec. 2.3.4, and optical-based sensing technology in Sec. 2.3.5. An overview of the existing tactile sensing technologies is presented in Sec. 2.4, including resistance-based sensing technology in Sec. 2.4.1, capacitance-based sensing technology in Sec. 2.4.2, piezoelectricity-based sensing technology in Sec. 2.4.3, organic field-effect transistors (OFETs) sensing technology in Sec. 2.4.4, magnetic-based sensing technology in Sec. 2.4.5, and optical-based sensing technology in Sec. 3.2.2. Finally, a summary is presented in Sec. 2.5.

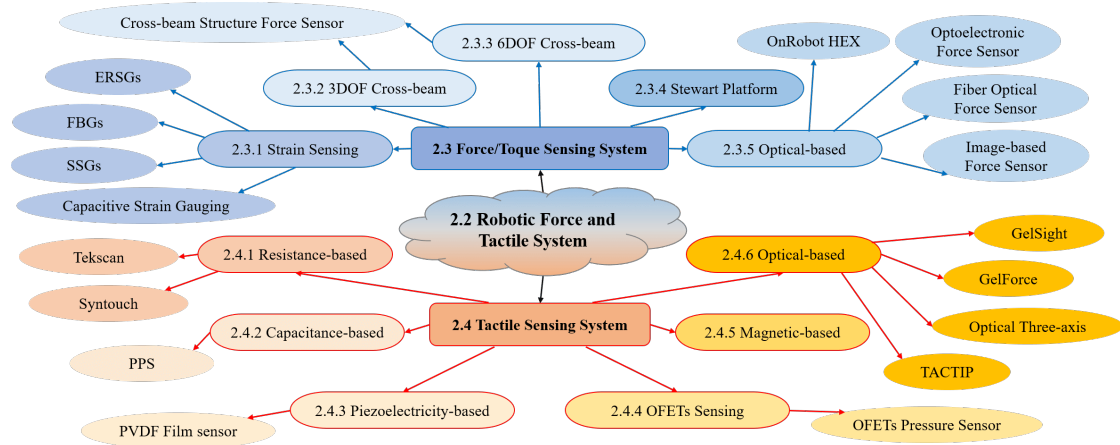


Figure 2.1: Overview of force and tactile sensing systems used in robotics.

2.2 Background of Robotic Force and Tactile Systems

In this thesis, we are particularly focusing on the development of a sensor that can be installed on a robotic system. As is defined by the International Standard Organization (ISO) 8373, a robot is “an automatically controlled, re-programmable, multipurpose manipulator programmable in three or more axes, which may be either fixed in place or mobile for use in industrial automation applications.” Today, robots operate in the rigid, fixed assembly line of the traditional factory as well in more complex environments such as hospitals, offices and hotels, where they are expected to interact with humans and deal with variable conditions rather than repeatedly conduct pre-defined tasks. The new application fields require the robot to be “smart” which means the robot shall be endowed with sufficient levels of intelligence to react to the real-world environment autonomously. In their drive to create robots able to efficiently interact with the environment, many roboticists have taken inspiration from biology to design robots that incorporate behaviours from animals [161] [163] [88] [133] or humans [27] [158] [39] [56].

Among biologically-inspired robots, the development of the end-effector, also known as a robot hand, is a typical example of a robotic device with one or multiple fingers imitating human-hand behaviour. Fig. 2.2 demonstrates several of the recent hand-like end-effectors; some of them are already commercialised while some are still under lab development. It is commonly accepted that the hand is the most dexterous part of the entire human body, and we are always amazed by the subtlety of movements and the high degree of rotations that a human hand can achieve. It is known that our hands are composed of tendons, joints, muscles, small bones, nerves, and blood vessels. When we pick up things or use tools, these parts will cooperate with each other to help us complete the work. As a result, the hand plays one of the most important roles when humans are interacting with the physical world. The research by Bicci [24] shows that the human hand is mainly dealing with three particular tasks, namely manipulating objects, restraining objects, and exploring the surroundings. Taking the object manipulation task as an example, we observe that human in-hand object manipulation [79] contains a series of actions, and each action completes a sub-task of the overall manipulation task. In addition

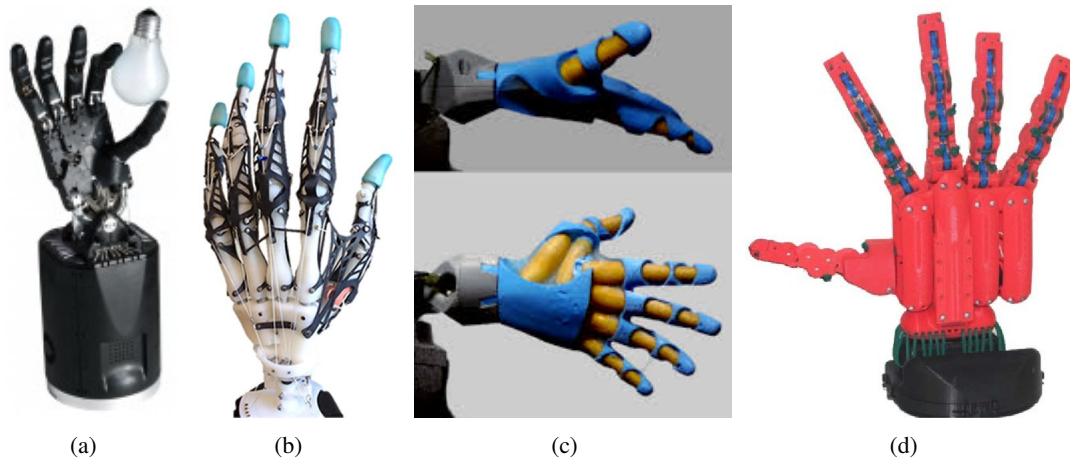


Figure 2.2: Examples of biologically-inspired robot, (a) Shadow Dexterous Hand [10]; (b) a Highly Biomimetic Anthropomorphic Robotic Hand [173]; (c) a Soft Biomimetic Prosthetic Hand [52]; (d) a skeleton of the Pisa/IIT SoftHand advanced anthropomorphic hand prototype [29].

to personal constraints, the choice of actions when performing a given manipulation task is guided by three sets of parameters: those parameters related to the object itself (for example the size, shape, weight and the surface texture); those related to the manipulation (for example the movement pattern), and lastly those pertaining to performance demands (for example accuracy and speed). Compared with the studies [47] [32] [24] upon human hand postures and movement for grasping objects, current robot in-hand manipulation has not yet achieved the same level as a human hand. One possible reason for this is the high complexity and diversity of the tasks. Another vital factor is the limitations of the sensing technologies in terms of relatively low sensitivity and spatial resolution. The sensing technologies here refer to the robotic force and tactile sensing technologies, which are especially important for acquiring information about the real-world environment during the interaction.

The human tactile system is extremely comprehensive as it consists of an extraordinarily high number of epidermis mechanoreceptors to detect the mechanical stimuli on the skin (shown in Fig. 2.3). Different kinds of mechanoreceptors are aligned at different depths in the human

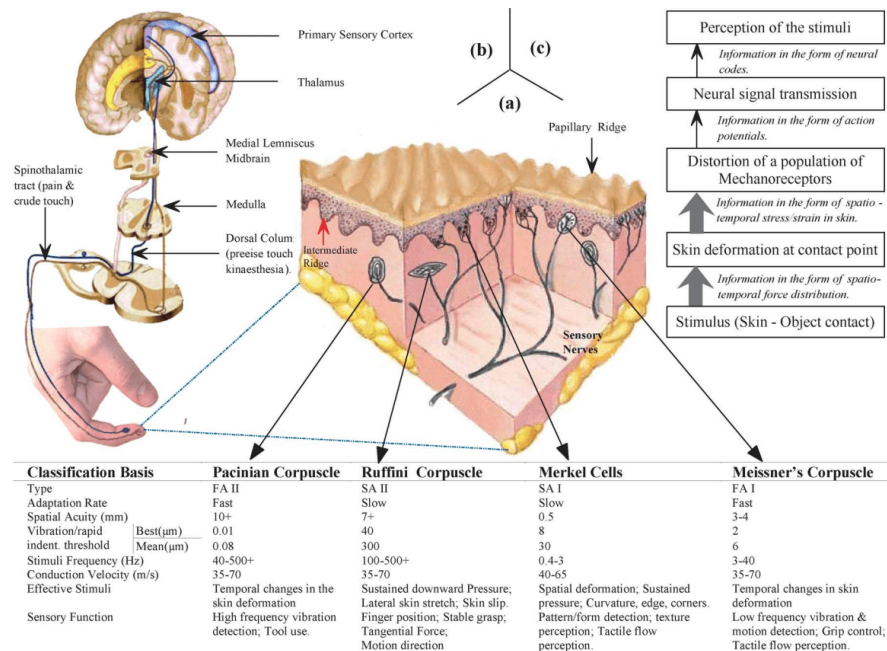


Figure 2.3: Section view of glabrous skin showing spatial location and classification of four mechanoreceptors [35]. It is noted that Ruffini corpuscle (with low spatial resolution) is for force estimation and is located beneath the Merkel cells (with high spatial resolution) which is for pressure and texture perception.

skin, namely as Merkel cells, Pacinian corpuscle, Meissner's corpuscle and Ruffini corpuscle [35]; these cells are responsive to different types of stimuli.

1. the Merkel cells are responsive to high-resolution skin deformation and low frequency forces;
2. the Pacinian corpuscle is responsive to low-spatial-resolution but high frequency vibration;
3. the Meissner's corpuscle is responsive to high-spatial-resolution but low frequency vibration;
4. the Ruffini corpuscle is responsive to low-resolution all-directions static forces based on skin stretched near joints.

All these mechanoreceptors work together when performing tactile sensing tasks. Apart from mechanical perception, other perception systems are also getting involved at the same

time, such as temperature perception and pain perception. The combination of these different perception systems make up the human tactile sensing system, and all of these receptors with multi-modalities work together during the physical contact with the external environment, thus, providing us an overall perception of the physical touch.

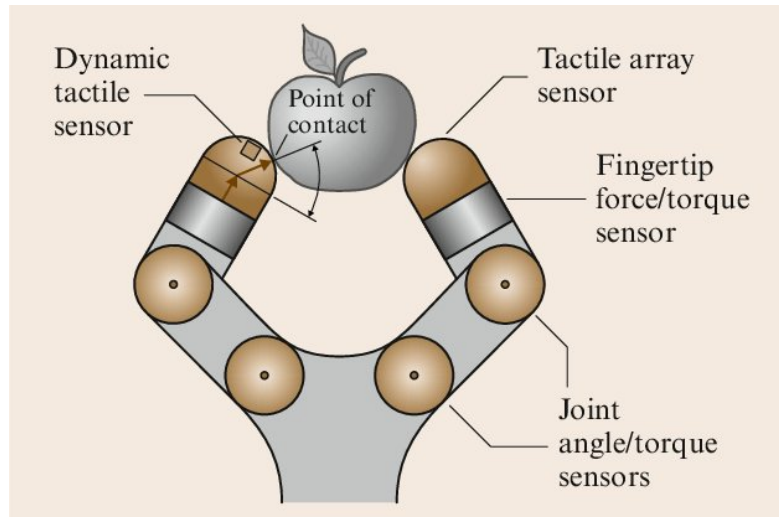


Figure 2.4: A theoretical model of an artificial force and tactile system that includes different kinds of sensors on a robot end-effector [62].

In robotics, force and tactile sensing imitates the human tactile system which is defined as the continuous sensing of variable contact forces [119]. One of the most famous theoretical models that have been developed is proposed by Howe [62], where different sensors are applied, and they all work as an integrated robotic force and tactile sensing system. As can be seen in Fig. 2.4, the system includes tactile array sensors at the end of the robotic finger to sense the pressure distribution of the contact surface, whilst multi-axis force/torque sensors are inserted behind the tactile array sensors to measure the overall forces and torques exerted by the fingertip contact. Additionally, dynamic tactile sensors are mounted on the robot's fingertip to sense the vibration, and lastly, joint angle sensors are placed at the joints to measure the precise angle of each joint: these sensors are further used for calculating the position, velocities, and accelerations of all the elements of the robot hand. However, compared with the human tactile system,

the current robotic tactile system cannot match the capabilities of the human sensing system. The majority of today's tactile sensing research is focusing on the development of individual, separately operating sensors. Another shortcoming of robotic tactile sensing systems is their inability to intelligently interpret the information given by the sensors. In many cases, the existing algorithms used to extract useful information from the data provided by the sensors are not developed enough to deal with the enormity of data [177]. Current multi-axis force/torque sensors and tactile sensors will be discussed in detail in the following sections.

2.3 Review of Multi-Axis Force Sensors

As described in [62], multi-axis force sensors are developed to measure forces and torques that occur in more than one direction within the robotic tactile sensing system. Due to their ability of performing multi-dimensional measurements of force and torque quantities, force sensors are generally installed on joints of robotic system structures. This feature makes force sensors very popular in a broad range of robotic research. Presently, force/torque sensors have been well-developed and also commercialised. Fig. 2.4 shows a layout [3] where an optical force/torque

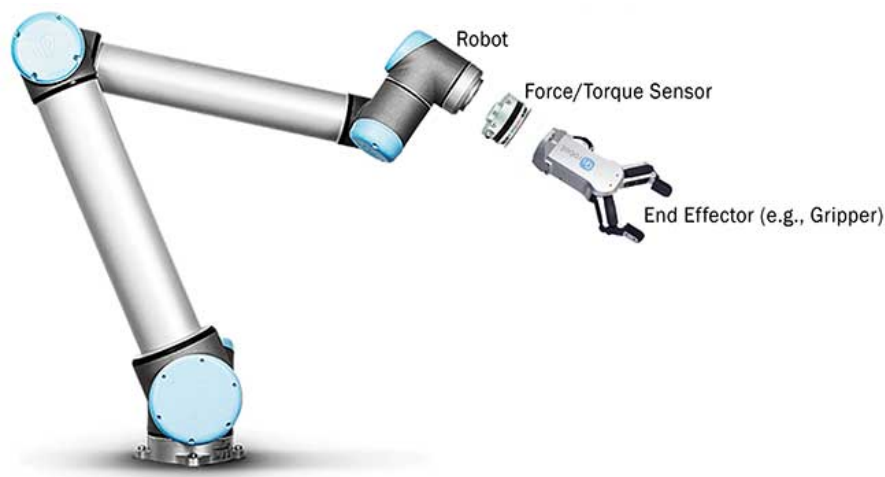


Figure 2.5: Force/Torque sensors expand robotic capabilities [3]. A force/torque sensor [4] is mounted between the robot arm [12] and the end effector (gripper) [9].

sensor HEX 6-axis Force/Torque sensor (formerly known as OptoForce sensor) [4] is installed between a UR5 robot arm [12] and the end of an arm tool, the RG2 Gripper [9]. Beyond optical sensing technology, extensive methods of developing multi-axis sensors have been proposed over the past few decades. The key points of a desired force sensor design require an elastic structure and a suitable sensing technology to measure its deformation, and then transfer it into the force/torque values. We will give examples of force sensors that use different sensing technologies and structures.

2.3.1 Strain Sensing Technology

Strain sensing has been one of the most popular methods used in a wide range of applications [22, 151, 145]. The majority of the force sensors use strain-sensitive elements installed on an elastic structure to measure multi-directional forces and torques; In general, strain sensing technology can be categorized into four main types, namely semiconductor strain gauges (SSGs), capacitive strain gauging, Fibre Bragg Gratings (FBGs) and electrical resistance strain gauges (ERSGs).

Semiconductor strain gauges (SSGs) is a sensing technology [122] that uses a semiconducting material. It usually uses silicon which has the piezoresistive effect (the electrical resistivity depends on its mechanical strain). To give a more detailed explanation, the gauge factor (GF) of a semiconductor strain gauges (SSGs) conductor with a longitudinal strain ε can be defined as:

$$GF = 1 + 2\nu + \left(\frac{1}{\varepsilon} \frac{\Delta\rho}{\rho}\right), \quad (2.1)$$

where ν is the Poisson's ratio of the SSGs material and ρ is the SSGs material resistivity which undergoes a variation of $\Delta\rho$. SSGs sensing technology has the advantage of high sensitivity; however, because of their small size, they are mostly used in micro-electro-mechanical systems (MEMS) force sensors.

Capacitive strain gauging is a sensing technology based on the capacitor's capacitance char-

acteristics which can be presented as:

$$C_p = \frac{\epsilon_0 \epsilon_r A}{d}, \quad (2.2)$$

where C_p stands for the capacitance, A is the cross-sectional area of two parallel plates of the capacitor, d is the distance between the two plates, and it is noted that $d \ll A$. ϵ_0 is the permittivity of free space and ϵ_r is the permittivity of the dielectric material filling the gap between the two plates. Capacitive strain gauging has the advantages of high sensitivity, however, similar to semiconductor strain gauges (SSGs) sensors, capacitive strain gauges can be developed via micro-machining techniques, and thus they are applied to small-scale force measurement. Moreover, because of its unique characteristics, capacitive sensing can also be applied within flexible sensors, and currently, it is widely used in tactile sensors, which will be described in detail in Sec. 2.4.2.

Fibre Bragg Gratings (FBGs) is a very popular force sensing technology [59] and it is a type of distributed Bragg reflector constructed in a short segment of optical fibre that reflects particular wavelengths of light and transmits all others. The working principle of FBGs is based on periodical modulation of the refractive index along with the core of a single-mode optical fibre. FBGs strain sensing technology has the advantages of immunity to electromagnetic (EM) interference, high-sensitivity, and waterproofness; however, the use of FBGs is always affected by the temperature compensation and FBGs itself is costly.

The working principle of electrical resistance strain gauges (ERSGs) is based on the fact that the change of the geometry of an electrical conductor leads to a change of its electrical resistance. Wheatstone bridge circuits are always involved in amplifying the small changes of the resistances within ERSRs; besides, the use of the Wheatstone bridge circuits also helps with the temperature compensation by introducing thermal-induced resistance variations on each arm of the bridge. However, ERSRs are affected by EM interference, and their sensitivity is relatively low.

To summarise, strain sensing technology is a very popular method for measuring force information, and it has been used in many commercial force sensors. Currently, strain gauges [6] (shown in Fig. 2.6(a)) and load cells [5] (shown in Fig. 2.6(b)) have dominated the strain measurement and weighing industry. The ATI multi-axis force/torque sensors family [2] (shown in Fig. 2.6(c)) that uses silicon strain gauges sensing technology is regarded as one of the most accurate force sensors within the entire industrial field because of its high sensitivity and repeatability.



Figure 2.6: Examples of commercialized force sensors, (a) a Strain gauge from [6]; (b) a miniature Tension and Compression Stud-Mount load Cell from [5]; (c) ATI force-torque sensors family from [2].

2.3.2 Three DOF Cross-beam Sensing Technology

Cross-beam design is one of the most widely used structures for multi-axis force sensors. A typical three Degrees of Freedom (DOF) cross-beam design is made up of an outer frame connected to the central platform with the use of multiple elastic beams. Fig. 2.7 shows a design that consists of four elastic beams in a planar cross-shape layout.

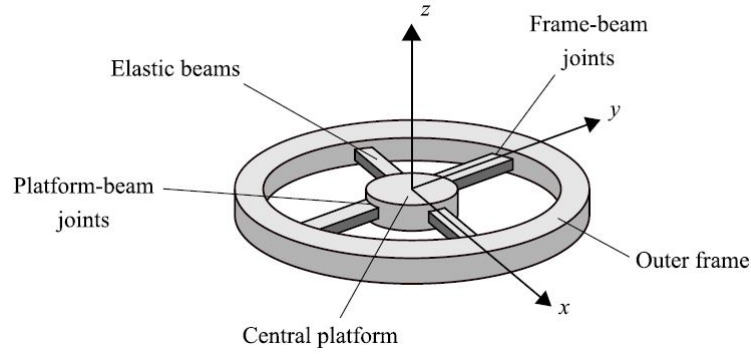


Figure 2.7: A typical design of a cross-beam structure force sensor which consists of the outer frame, central platform, and four elastic beams.

In general, according to different load combinations, the three DOF force sensors can be categorized into three types: sensors for measuring F_x , F_y , F_z (known as 3DOF-A); sensors for measuring F_x , F_y , T_z (known as 3DOF-B); and sensors for measuring F_z , T_x , T_y (known as 3DOF-C). As shown in Fig. 2.7, different force and torques can be measured depending on different deformation scenarios within the cross-beam structure. As for measuring the force F_x and F_y , the exertion of in-plane F_x and F_y will cause axial deformation in the elastic beams that are parallel to the exertion direction, together with the lateral bending in the elastic beams that are perpendicular to the exertion direction. As for measuring the force F_z , the exertion of F_z will cause out-of-plane bending in four elastic beams. As for measuring the torque T_x and T_y , the exertion of T_x and T_y will cause out-of-plane torsion in the elastic beams that are parallel to the exerting lateral moment, together with the out-of-plane bending in the elastic beams that are perpendicular to the exerting lateral moment. As for measuring the torque T_z , the exertion of

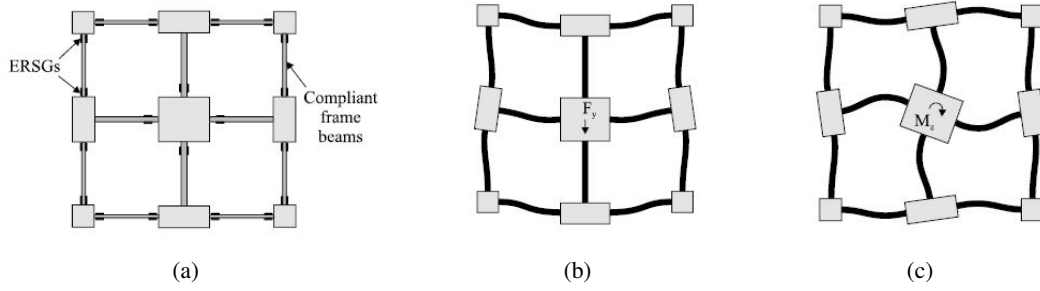


Figure 2.8: A 3 DOF-B sensor design [77]. The proposed force sensor uses 12 compliant elastic beams to connect the outer frame and central platform: (a) the overall layout of the sensor, (b) the deformation scenario when a lateral force F_y is exerted, (c) the deformation scenario when a torque T_z is exerted.

T_z will cause lateral bending in four elastic beams. Specifically, in the design of a cross-shape layout with four elastic beams, the collinearity between the elastic beams and the x - and y -exerting directions helps to decouple the sensor output, as well as maximizing the strain in each beam. Moreover, this design also achieves an identical response for mutually orthogonal lateral forces and torques.

The deformation of each elastic beam can be measured using different technologies, such as piezoresistive method [51], captive method [21], Fibre Bragg Gratings (FBGs) method [171], and electrical resistance strain gauges (ERSGs) method [156]. Fig. 2.8 gives an example of a 3DOF-B sensor using ERSGs method, based on the model proposed in [77]. The sensor consists of 12 compliant elastic beams within both outer frame and central platform, and the end of each beam is equipped with a ERSGs. Using the compliant beams in both the central frame and the outer frame allows the decoupling of the sensor output since different load conditions will exert different deformation to each beam.

2.3.3 Six DOF Cross-beam Sensing Technology

Six degrees of freedom (DOF) cross-beam sensing technology can be categorized into three types according to different structures: rigid jointed cross-beams structure, flexible jointed cross-

beams structure, and dual-layer cross-beams structure.

The rigid jointed cross-beams structure is the most direct way of extending the typical three DOF cross-beam sensors into six DOF cross-beam force sensors. This type of sensor usually adds strain-sensing elements on all sides of the elastic beams to measure both lateral and vertical deformation. For example, Chao and Yin [31] show a six-component force sensor, which is an extension of the mechanical design in Fig. 2.7, for measuring the loading of human feet in locomotion. Another example is a six DOF cross-beam sensor design proposed by Palli et al. [117]. The proposed sensor (shown in Fig. 2.9(a)) is using optoelectronic sensing technology for detecting the deflection of the cross-beam. As shown in Fig. 2.9(b), the sensor consists of

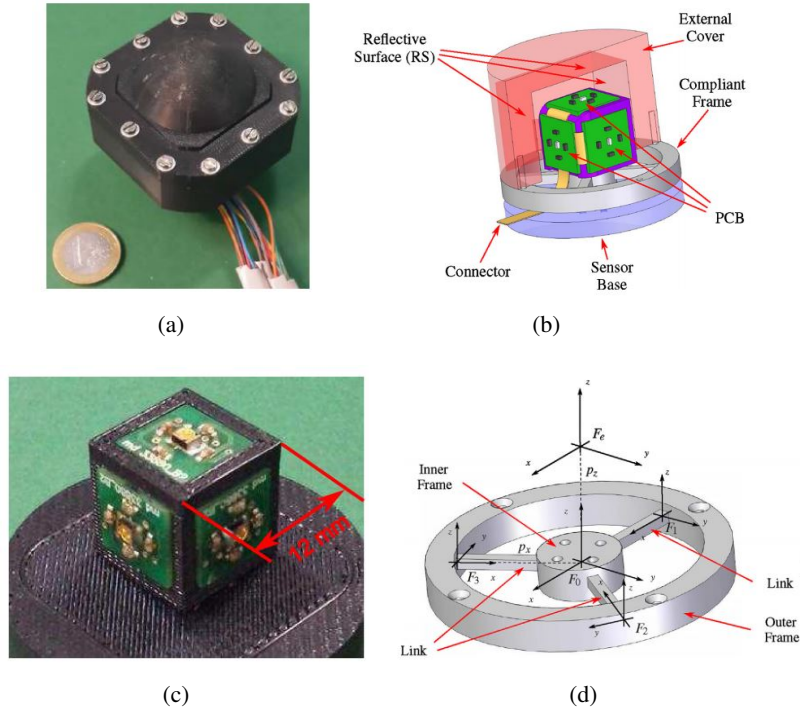


Figure 2.9: A cross-beam 6-axis force/torque sensor that uses optoelectronics proposed in [117]. (a) the sensor prototype, (b) the conceptual design of the sensor, (c) the view of the cube with the three printed circuit board (PCB)s, each PCB consists of a light emitting diode (LED) and four photo detectors (PDs), (d) the 3D drawing and related reference systems of the compliant frame that is shown in the conceptual design of the sensor.

a cube with three PCBs (shown in Fig. 2.9(c)) mounted on a compliant frame structure (shown in Fig. 2.9(d)). A cover with an internal reflective surface (RS) is placed above the sensor base. The PCB ($10\text{ mm} \times 10\text{ mm}$ in size) mounted on the cube is made of an LED placed in its center and four photo detectors (PDs) that are symmetrically located around the central LED at a 3 mm radius. When loads are applied to the sensor cover, the deformation of the cross-beam within the compliant frame structure is indirectly measured by the light intensity changes received by the various of PDs emitted from the LED through relative movement of the corresponding reflective surface on each side of the cube. To summarise, the rigid jointed cross-beams structure is a very common method to achieve six-axis force and torque measurements, and has been widely adopted in multi-axis force sensor development.

The flexible jointed cross-beam structure uses flexible outer frame beam joints to help decouple the sensor outputs. These flexible frame beam joints are similar to the universal joints. Three DOF compliance is provided within the joints [55]. A variation of flexible jointed cross-beams structures has been proposed in the past few decades, one of the earliest models in force detection being the one put forward is by Scheinman [137]. The proposed flexible jointed cross-beam structure has thin flexures at the four outer frame beam joints. The semiconductor strain gauges (SSGs) method is used to measure the deformation of the four beams. This model is then further explored with the purpose of improving sensitivity and isotropy by means of applying different sensing technologies (for example electrical resistance strain gauges (ERSGs) in [157] and piezoresistive strain sensing in [37]) and different mechanical designs at the outer frame beam joints (for example a ball-bearing design in [30] and a radial spherical bearing design in [141]). Another typical example of the flexible jointed cross-beam structure model is the one using parallel-plate beams in the outer frame, which is proposed by Kim [75]. He further improves the design in [78] where 24 ERSGs are used to measure both the lateral and vertical displacement of the compliant parallel-plate-beam. Further explorations are conducted with more complex mechanical designs in [103] and [54]. Extending from this, Sun et al. [148] proposes another high-sensitivity force sensor with the use of highly-compliant plates in the outer frame. The

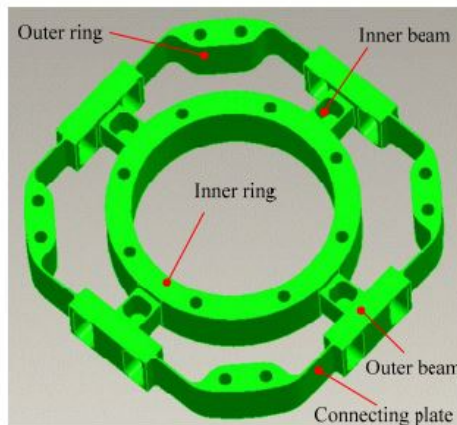


Figure 2.10: The flexible jointed cross-beams structure proposed in [148]. The six DOF force/torque sensor is comprised of four cross beams (Inner beam) with vertical blind hole on its top side and four laterally-compliant plates with lateral through holes in the outer frame beam joints (Outer beam). The inner beams form a 3DOF-*B* structure, and the outer beams form a 3DOF-*C* structure.

sensor design is shown in Fig. 2.10, where the structure consists of four cross-beams connecting the outer frame and the central platform. Each cross-beam has a vertical blind hole (blind hole (BH)) on its top surface acting as a 3DOF-*B* structure, and the outer frame beam joints have two horizontal through-holes (through hole (TH)s) at each joint acting as a 3DOF-*C* structure. The ERSGs method is applied for sensing the deformation of the elastic body. To summarize, the advantage of a flexible jointed cross-beams structure is that it enables the sensor body to be fabricated in one piece, which can avoid the unwanted mechanical friction and clearances that can occur when assembling a sensor from separate components.

The dual-layer cross-beam structure comprises a vertical assembly of two cross-beam force sensor structures, each one of whom is responsible for measuring a specific three degrees of freedom (DOF) force/torque components (therefore six DOF components for the entire structure). It is noted that the two cross-beam structures can be two rigid jointed cross-beam structures, or two flexible jointed cross-beam structures, or one rigid jointed cross-beam structure and one flexible jointed cross-beam structure. One example is a six-component force/moment sensor proposed by

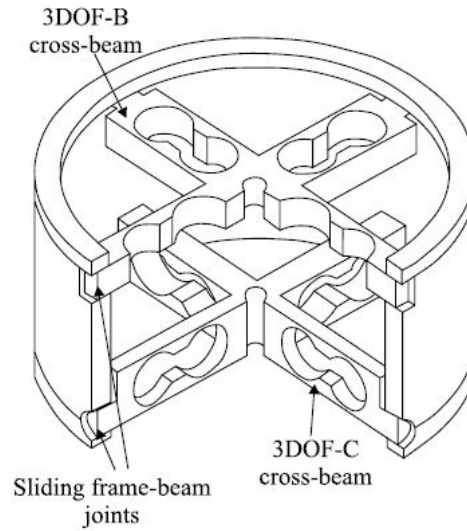


Figure 2.11: The dual-layer cross-beam sensor proposed in [168]. The sensor can measure six-axis force/torque components, and it is comprised of a 3DOF-*B* cross-beam structure and a 3DOF-*C* cross-beam structure in a vertical layout. The outer frames of both cross-beam structures are connected with the use of sliding frame-beam joints.

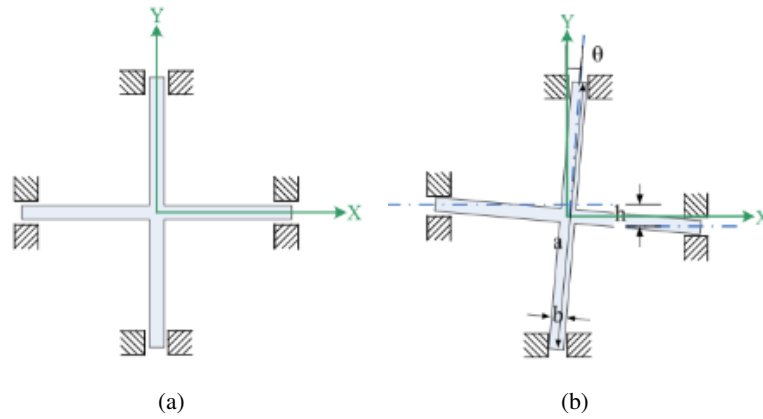


Figure 2.12: Contact modes between the elastic body and the groove. (a) Contact without angle; (b) contact with an angle.

Kim et al. [76]. The proposed sensor combines the 3DOF-*B* sensor structure (shown in Fig. 2.8) with a 3DOF-*C* sensor structure in a vertical layout. The outer frames of the two cross-beam structures are connected and electrical resistance strain gauges (ERSGs) sensing technologies

are applied for measuring the deformations of the cross-beams. Another example is a six-axis force/torque sensor proposed by Wu and Cai [168]. As shown in Fig. 2.11, the sensor consists of a 3DOF-*B* cross-beam structure and a 3DOF-*C* cross-beam structure in a vertical layout. The end of each cross-beam is inserted into grooves of an outer-cylindrical shell, and each of the cross-beam contains an ‘eight-shape-like’ hole structure which enables double bending (lateral and vertical) for each beam. The outer frames of both cross-beam structures are connected with the use of sliding frame-beam joints to decouple the measurement results; however, it is noted that the choice of the sliding clearances needs accurate calculation as the size of the clearance between the elastic body and the groove can bring additional coupling error during contact and the error increases with the increase of the angle (see Fig. 2.12).

2.3.4 Stewart Platform Sensing Technology

The Stewart platform (shown in Fig. 2.13) is a six DOF mechanism that is composed of a rigid upper platform connected to a fixed bottom base via six legs, proposed by Stewart [146]. This design has also been used in force sensor applications, where the leg structures are replaced with elastic elements, of which the axial deformation caused by the load can be measured using different sensing technologies. In general, this type of force sensor has six DOF force/torque sensing capability and high loading capacity. However, the sensor always has a rigid structure.

One of the early force sensors proposed by Romiti and Sorli uses a six DOF Stewart platform [131], where six single-axis force sensors are used as the leg structure with low-friction ball joints. More studies of this prototype are conducted in [49] and [142], and it is found that the sensor shows a nonlinear behaviour and a high degree of hysteresis due to the use of the ball joints. Hysteresis is defined as the maximum difference in sensor output at a pressure when that pressure is first approached with pressure increasing and then approached with pressure decreasing during a full span pressure cycle [11]. The hysteresis correlates to the sensor accuracy and is determined by the hardware (material properties for instance). Another prototype is proposed by Dai and Kerr [36], where six pre-tensioned flexible wire legs are used, and the force in each

wire is measured with the use of electrical resistance strain gauges (ERSGs). Later on, several sensor prototypes [72, 46, 181, 128, 23, 134] with different mechanical designs and sensing technologies are proposed. The lateral sensor prototypes have a monolithic structure and flexural

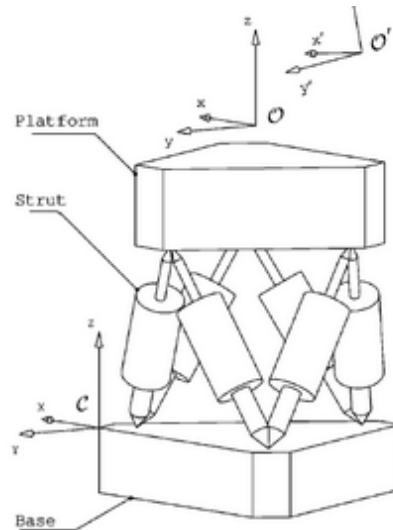


Figure 2.13: Schematic design of a Stewart platform structure, the design is comprised of the upper platform, fixed bottom base, and six leg structures.

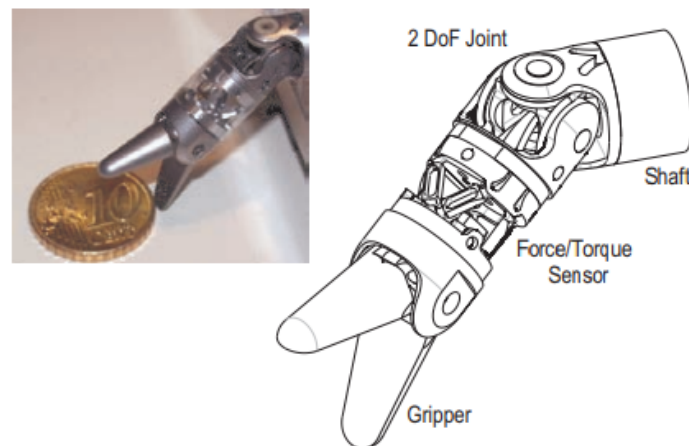


Figure 2.14: Illustration of a distal end of the instrument for minimally invasive surgery. The end contains a distal force-torque sensor, joint, and gripper mechanics.

joints mechanism to replace the traditional spherical joints. [140] gives an example of a small-scale force sensor for minimally invasive robotic surgery (MIRS). The proposed force sensor is installed within the surgical instrument end and is located between the gripper and joint (as shown in Fig. 2.14). The sensor is used for measuring manipulation forces at the instrument tip and is miniaturised with an outer diameter of 10 mm. It uses electrical resistance strain gauges (ERSGs) method together with flexural joints within the six DOF Stewart platform. In summary, the force sensors based on the Stewart platform have the advantage of being highly adaptable with regards to stiffness and scalability. However, they suffer from mechanical hysteresis.

2.3.5 Optical-based Sensing Technology

The optical sensing method has attracted interest from many researchers keen to develop force sensors in the past few years. There are currently different types of optical-based force sensors, including sensors using optoelectronics, optical fibres, and cameras. Examples of each method will be presented.

One type of optical-based force sensor make use of optoelectronics which can be integrated into specific mechanical structures. It is noted that unlike the other sensing methods like strain

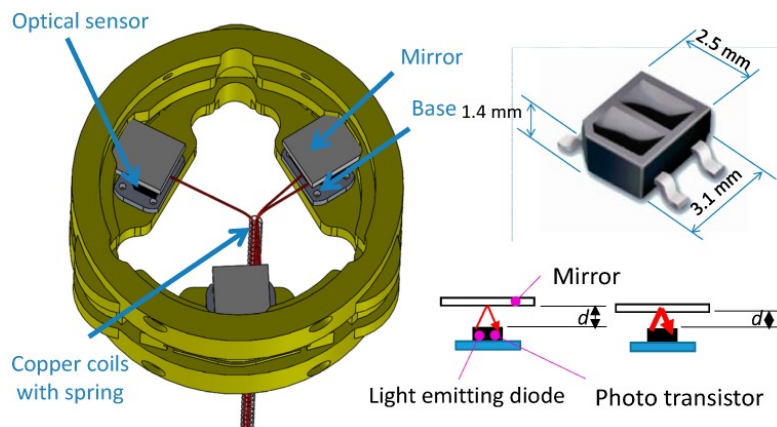


Figure 2.15: An optoelectronic force sensor design proposed in [107]. The sensor can measure three-axis force/torque components, and it is comprised of a bespoke mechanical structure equipped with mirrors and three pairs of light-emitting diodes and photo-transistors.

gauges, piezoresistive and capacitive methods, optoelectronic components are not physically connected to both ends of the mechanical beam; instead, reflective surfaces are used to reflect the emitted light back to the optoelectronic receiver. Thus, the deformation within the mechanical structure can be indirectly measured. Since this type of sensor does not require mechanical contact with the structure, a lower level of noise is exhibited when compared with the methods mentioned above. One example is described in the above subsection in Fig. 2.9, another example is a sensor proposed in [107]. As shown in Fig. 2.15, the sensor has an outer-cylindrical shell, and three mirrors, while three pairs of light-emitting diodes and photo-transistors are integrated within a bespoke mechanical structure. The proposed sensor can measure 3DOF-C components with a low-level noise via detecting the changes of the received light intensity reflected by the mirror. Another popular sensor is the OptoForce 3-axes force sensor [7]. As shown in Fig. 2.16. OptoForce is a dome-shaped sensor that can be mounted on the robot fingertip. There is a reflective layer inside the outer sensing surface which is made of silicone. When an contact occurs, the photodiodes (placed at the bottom) measures the amount of reflected light which is originally emitted by the LED (also placed at the bottom). Then, by comparing the measured values

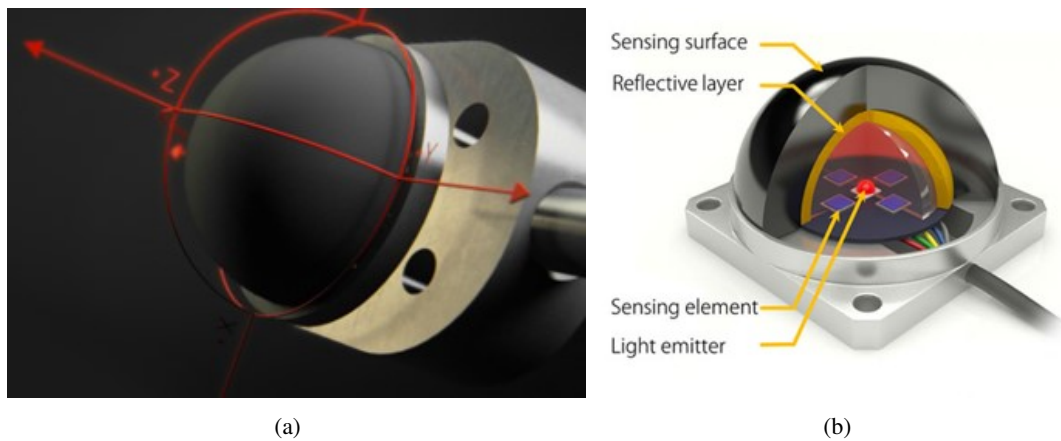


Figure 2.16: OptoForce 3-axes force sensor in [81]. (a) the fingertip sensor prototype, (b) the sensing principle of the OptoForce sensor, where the photodiodes at the bottom measure the amount of reflected light emitted by the LED. The force can be reconstructed based on the measured light intensities.

on the photodiodes, the exerted 3-axes forces can be precisely reconstructed. The measurement range of the sensor is from 10 N to a few thousand newtons due to different silicone materials that are used. To summarise, the advantages of optoelectronic sensor are its high degree of miniaturization, low cost, and high sensitivity.

Another type of optical-based force sensor makes use of optical fibres [57], which allow it to be light weight and small in size. Moreover, optical fibres are immune to electromagnetic interference, water, and corrosion. Currently, four main fibre optic sensing approaches are used based on the modulation of the wavelength, the phase, the polarization, and the intensity of the light signals. For the modulation of the wavelength sensing approach, Fibre Bragg Gratings (FBGs) [105], which has been described in the above subsection, is the most widely used sensing technology with high sensitivity. However, it is fairly costly. For the modulation of the phase sensing approach, the commonly used methods are based on Mach-Zehnder and Fabry-Perot principles [174] where an interferometer is used to compare the phase of a light signal with a signal from a reference fibre; in this way, the applied forces can be estimated. This approach has a high sensitivity, but the entire sensor system is fairly complex and hard to manufacture. For the modulation of the polarization sensing approach, linear, elliptical, and circular polarization approaches are being used, where the changes in the fibre polarization state caused by the stress or strain can be detected [135]. This approach is of high sensitivity but is more expensive compared to other approaches. For the modulation of the intensity sensing approach, the commonly used methods are based on detecting the magnitude change of the fibre light intensity relying on the reflection, transmission, or the bending of the fibre caused by the external force. This approach has the advantages of high accuracy, insensitivity to temperature, and inexpensiveness compared to other approaches.

Due to the versatility of the intensity modulation approach, many force sensors based on this principle have been developed. A hybrid fibre optical force/proximity sensor [81] is shown in Fig. 2.17, This robot-finger-integrated perception sensor is composed of five pairs of optical fibres that detect light intensity at each sensing elements (three force sensing elements and two

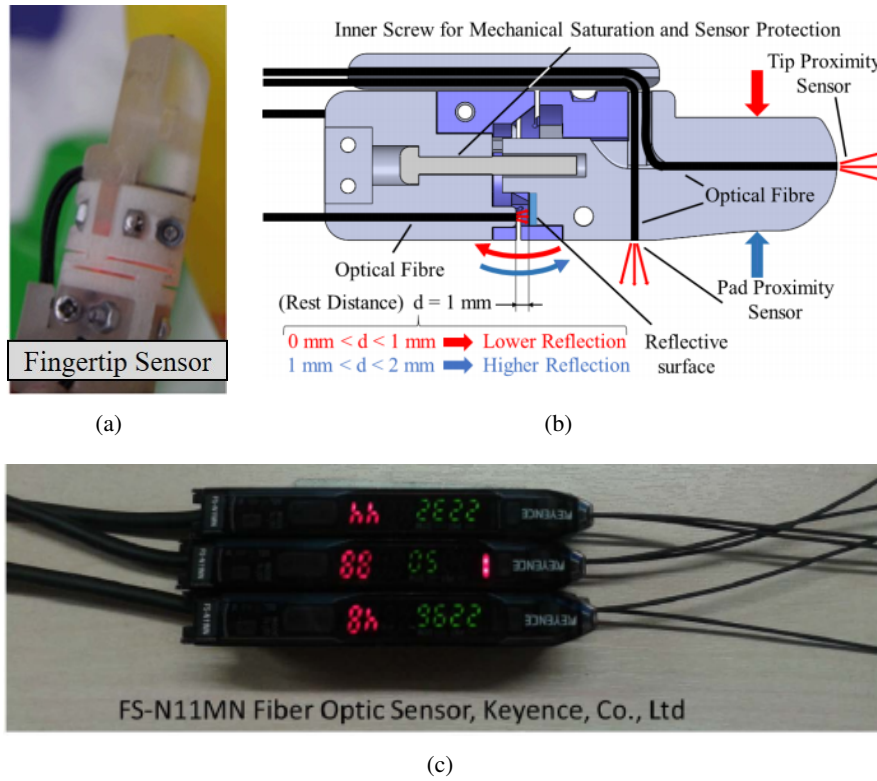


Figure 2.17: Hybrid fibre optical force/proximity sensor in [81]. (a) the fingertip sensor prototype, (b) the sensing principle of the integrated fingertip sensor, where the red and blue arrows show sensor behaviour for deflections in different directions, (c) the FS-N11MN fibre optic sensor from Keyence.

proximity sensing elements), where each sensing element consists of a transmitting fibre and a receiving fibre. For the three-axes force measurement, a cantilever mechanical structure with reflective surfaces on each cantilever beam is equipped with three pairs of optical fibres, and the surfaces are painted with a thin layer of reflective metallic paint. The deflection of the mechanical structure caused by the external force leads to the displacement of each reflective surface with respect to the tips of the corresponding pair of optical fibres. The light intensity is modulated as a function of the applied forces with the use of the FS-N11MN fibre optic sensor from Keyence (shown in Fig. 2.17(c)). A similar sensing principle is also applied in another three-axis force sensor for flexible manipulators [111].

Apart from using the Keyence sensor for fibre light intensity modulation, another common method is using a camera and estimating forces using image processing techniques. A magnetic resonance (MR) compatible tactile force sensor [170] is shown in Fig. 2.18, where pairs of optical fibres and miniature mirrors are installed within a flexure structure. Applied forces lead to a displacement of the mirror in respect to the tips of the corresponding pair of optical fibres, the transmitting fibres are connected to a light source, and the receiving fibres are connected to a camera at its proximal end. The camera reads the light intensity of the receiving fibres, and the applied force is estimated as a function of the number of activated pixels in the camera

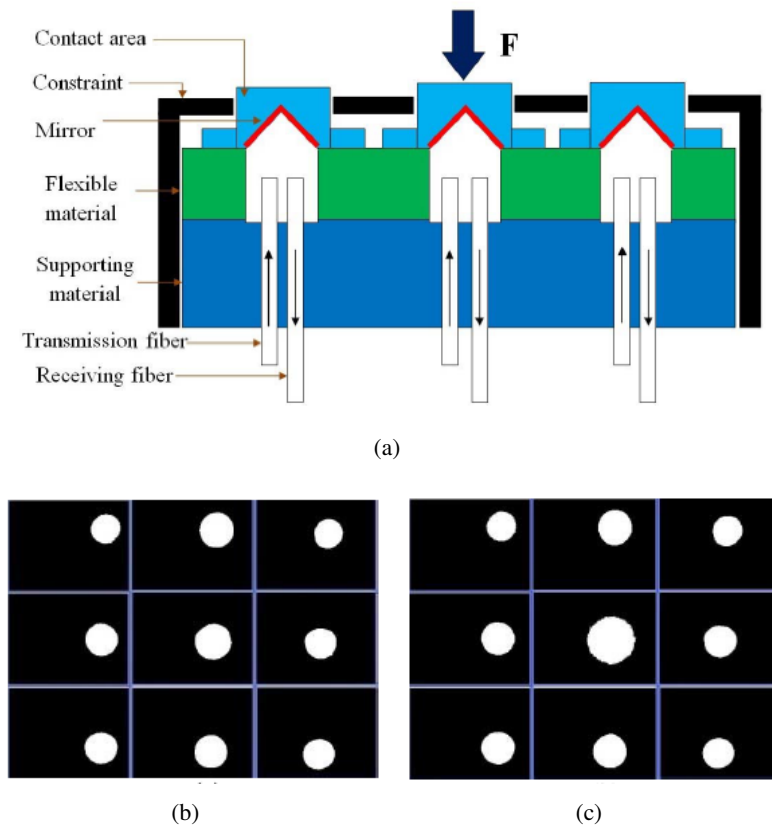


Figure 2.18: A magnetic resonance-compatible tactile force sensor design proposed in [170]. (a) The sensor uses fibre optics with mirrors and a vision sensor (camera) to measure the normal force; (b) the received image under the unload status; (c) the received image when a normal force is applied on the central sensing element of the sensor.

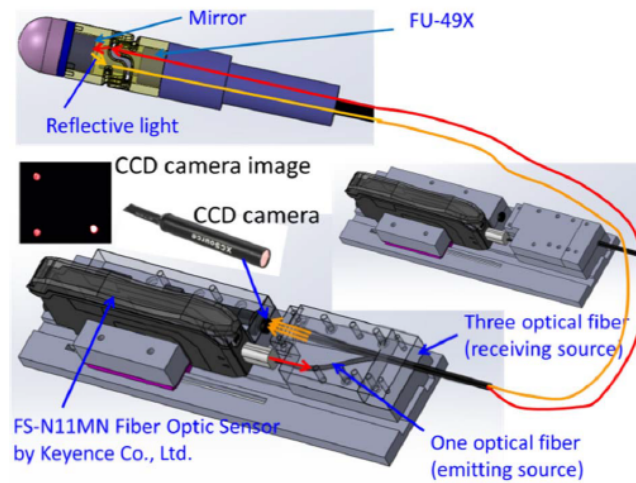
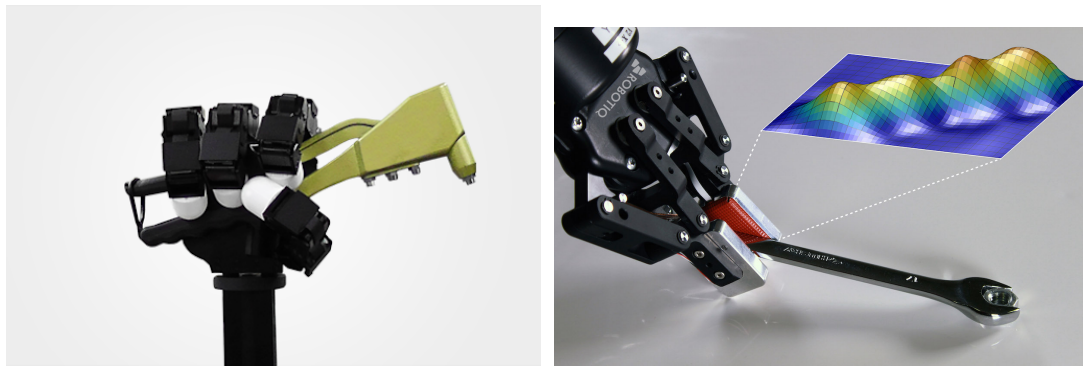


Figure 2.19: Image-based optical miniaturised force sensor [109] for cardiac catheterization. The sensor can measure three-axis force components, and it is comprised of a 3DOF-A cantilever structure (equipped with a mirror and a pair of optical fibres) and a camera.

images. Another image-based optical force sensor [109] for cardiac catheterization is shown in Fig. 2.19. This type of sensor has the advantage of being small in size, robust and low cost. This miniaturised force sensor uses a 3DOF-A cantilever structure (equipped with small-sized multi-cores optical fibres and a mirror) and a CCD camera for three-axis forces measurement. The deflection of the mechanic structure leads to a displacement between the mirror and the tips of the optical fibres; the camera reads the receiving fibre light intensity. By processing the received images, the applied force can be estimated as a function of the light intensity.

2.4 Review of Tactile Sensors

The sense of touch plays a very important role for both humans and robots during grasping and manipulation tasks (see Fig. 2.20). Tactile sensors which have been widely investigated over the past few decades, are regarded as the future of robotic grasping [44]. Robots need tactile feedback if they are to be able to determine the amount of force they have to exert on an object whilst manipulating it. As shown in Fig. 2.4, tactile sensors are usually mounted at



(a) In-hand Manipulation [1]

(b) Robotic Grasping [44];

Figure 2.20: Examples of the robotic tactile system using different robots.

the robot fingertip to acquire tactile information that includes mechanical stimulus detection of contact, slip, pressure and temperature. Therefore, an ideal tactile sensor (if is as powerful as a human's tactile system) can give a robot hand the capability to grasp an object regardless of the texture, shape, or location of the object. However, current tactile sensing technology is still underdeveloped and hence not yet as comprehensive as the human's tactile system. One main issue is that the tactile signals are naturally complex. Simply adding multiple individual tactile sensors cannot effectively help the enhancement of the robot hand's manipulation and grasping capabilities. The goal is to combine and transform the multiple raw and low-level sensing data into high-dimensional information. In other words, the integration of the tactile information still needs more software-side algorithm to improve. Nowadays, many tactile sensors for robots are biologically inspired; in their drive to improve tactile feedback, researchers look to structures and processes encountered in nature. Sensing technologies that have been used in tactile sensors include resistance-based, capacitance-based, piezoelectricity-based, organic field-effect transistors (OFETs), magnetic-based and optical-based. Each sensing technology will be described in the following subsections.

2.4.1 Resistance-based Sensing Technology

Resistance-based tactile sensing technology is based on Ohm's Law which can be presented as:

$$V = IR \quad (2.3)$$

where V is the measured voltage, I is the measured current, and R is the electrical resistance. In general, a resistance-based tactile sensor [162] transfers the applied loading pressure as a function of the measured electrical resistance between a conductive polymer and at least two electrodes on multiple sensor cells, as shown in Fig. 2.21. Therefore, it needs to be constructed of conductive, pressure-sensitive materials, such as foam, rubber and ink. All of these materials are set up as a mesh layout for tactile sensing.

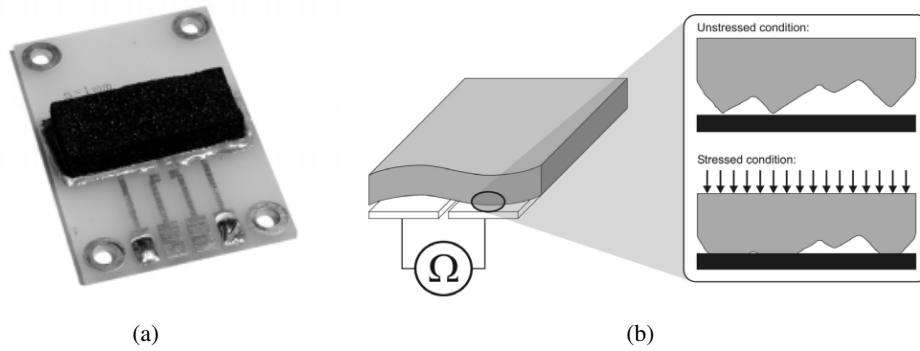


Figure 2.21: A typical resistive tactile sensor in [162]. (a) The electrode board with glued sensor material; (b) the working principle of a resistive tactile sensor cell, where the compression leads to incrementing the contact area, resulting in a decreased electrical resistance between the sensor material and the electrode.

Apart from the in-lab resistance-based tactile sensors [19, 14] that use carbon nanotube (CNT) and polydimethylsiloxane (PDMS) composite, resistance-based tactile sensors have already been commercialised. For example, Tekscan, Inc commercialised the sensor [118] for pressure mapping. As shown in Fig. 2.22, the sensor is made up of two parallel $25\mu m$ thick

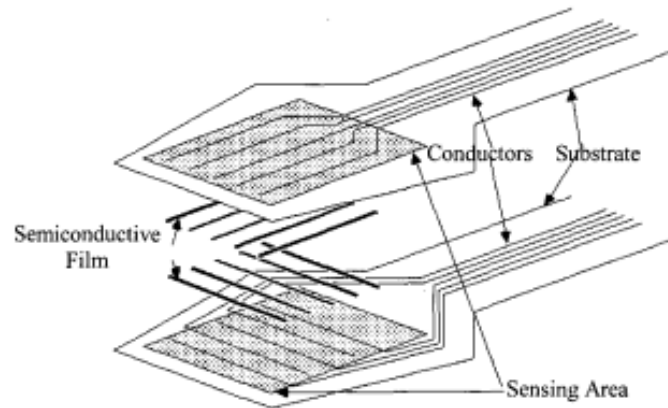


Figure 2.22: The structure of the Tekscan resistance-based sensor [118].

polyester sheets, which are attached to each other with adhesive in the non-sensing area. Ag-filled polymer conductive traces that are covered by thermoplastic semiconductive ink of resistivity ρ , are screen-printed on the sheets to form a grid in the sensing area. Each cross-section of the grid forms an individual contact force sensor at a spatial resolution of 0.5mm . Therefore, the exerted loads lead to a change of conductance in each sensor cell.

Another commercial tactile sensor is the Syntouch's BioTac tactile sensor (shown in Fig. 2.23(c)). This finger-shaped sensor array prototype was proposed by Wettels et al. [164] with the purpose of mimicking the full cutaneous sensing capabilities of the human finger [165] in terms of contact force, microvibrations and thermal fluxes. The force sensing element within this tactile sensor is resistance-based, as shown in Fig. 2.23(a), the sensor has an elastic skin filled with a conductive fluid over a rigid bone-like core (with multiple impedance electrodes attached). The working principle can be described as follows: The exerted force deforms the elastic skin and the underlying fluid, which leads to changes in the thickness between the skin and the electrodes; this thickness change is equivalent to the thickness change of the fluid path. Since the electrical resistance of each electrode is related to the fluid path, the change of fluid path results in the change of the resistance of electrodes arranged on a distributed pattern. Then artificial neural

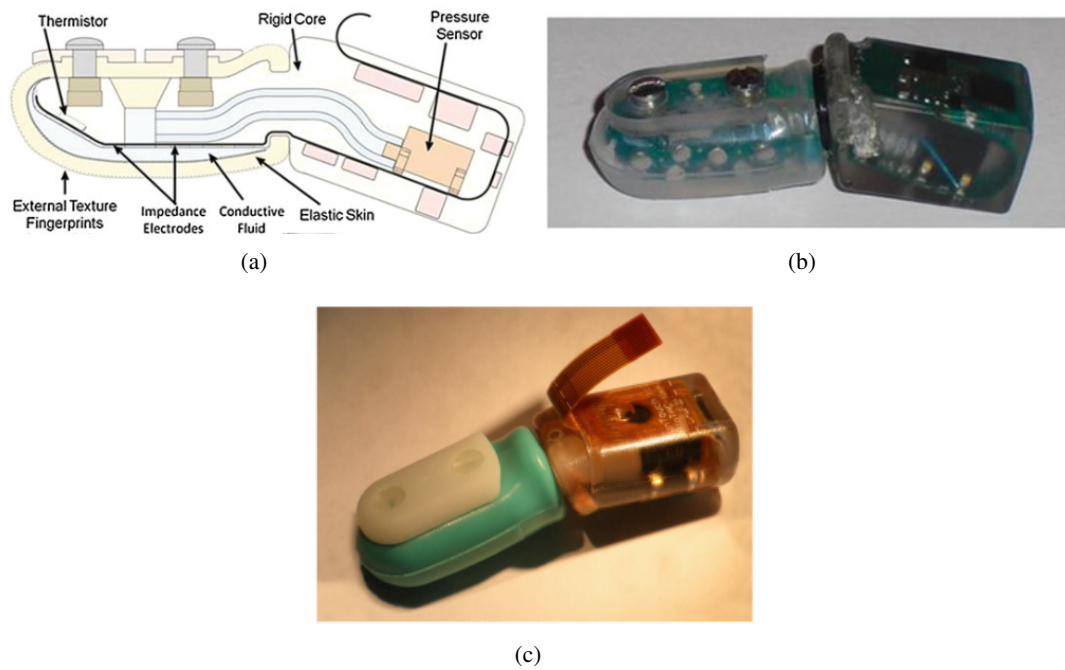


Figure 2.23: The Syntouch's BioTac tactile sensor design. (a) The cross-sectional drawing of BioTac showing various components used for each sensing modality. (b) The angular view of the sensor [164] with skin and nail installed. The device is filled with $200\mu L$ of conductive fluid. (c) Photography of an assembled BioTac in [50].

networks (ANN) and Gaussian mixture model regression (GMMR) are applied to extract three-dimensional force vectors from numbers of electrode sensing channels so that the sensor can obtain the information of the point of contact, magnitude, and the direction of the force. However, the frequency response and spatial resolution of the sensor are limited by the viscoelastic properties of the fluid path scheme within the elastic skin.

To summarise, resistance-based tactile sensing technology is relatively well-developed and has been commercialised. This type of sensor requires the involvement of conductive materials and electronic components which allows for its miniaturisation. However, the sensor suffers from hysteresis and is sensitive to temperature changes.

2.4.2 Capacitance-based Sensing Technology

Capacitance-based tactile sensing technology is based on the capacitor's characteristics which are presented in equation 2.2. This technology is regarded as one of the most sensitive technologies for detecting small deflections of sensor structures, and it has been widely explored nowadays [40, 159, 58]. It is worth mentioning that the capacitance-based sensor is not affected by temperature changes [97].

One typical example is the capacitive sensor [90] developed by Lee et al. This tactile sensor is designed to be capable of measuring both normal force and shear force. The sensor system has a measurement range of $0 - 10 \text{ mN}$ with sensitivities between $2.5\%/mN$ and $3\%/mN$ in both normal and tangential directions. The tactile sensor is composed of 64 tactile cells arranged in

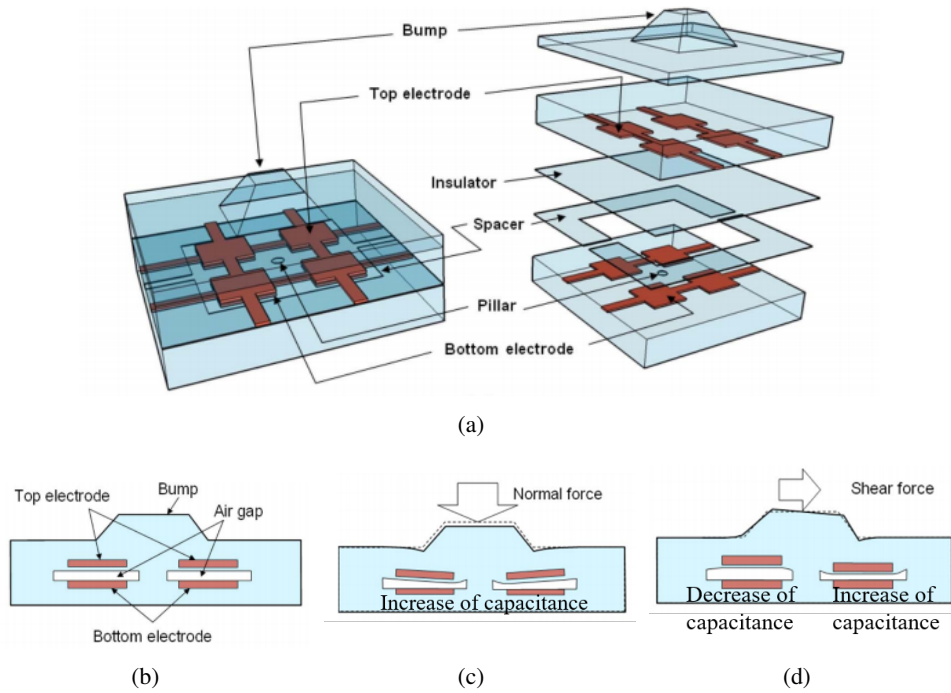


Figure 2.24: Conceptual diagram of a tactile cell of the capacitive sensor [90] that can measure both normal force and shear force. (a) the schematic view of the cell (b) the cross-sectional view of the cell without loads (c) the cell's response to the normal force (d) the cell's response to shear force

an 8×8 array with the overall size of $22 \times 22 \text{ mm}$. Each tactile cell is of $2 \times 2 \text{ mm}$ in size. Four electrodes are placed inside of each cell, as shown in Fig. 2.24(a), configured on both the top polydimethylsiloxane (PDMS) layer and the bottom PDMS layer. A PDMS spacer layer with air gaps, an insulator layer, and a pillar is embedded between two PDMS layers of the capacitor plates. Thus, as shown in Fig. 2.24(b), the capacitance of the tactile cell will alter when an external force is applied on the top bump leading to a deformation of the middle air gaps. When a normal force is applied, as shown in Fig. 2.24(c), the air gaps between all electrodes decrease which results in an increase in all four measured-capacitance (see 2.2, a decrease of distance d results to an increase of capacitance C). When a shear force is applied, as shown in Fig. 2.24(c), the heights of air gaps behave differently on each pair of electrodes, and there are two increased measured-capacitance (two air gaps are compressed) and two decreased measured-capacitance (two air gaps are expanded). However, the issue of cross-talk between the different cells in the sensor is not addressed.

The capacitance-based tactile sensor has been commercialized and a typical example is the sensor from pressure profile systems (PPS) [8], as shown in Fig. 2.25. The sensor contains 20 – 24 tactile sensing cells (each cell size is between $25 - 100 \text{ mm}$). The pressure measurement range of the sensor is between $0 - 20 \text{ psi}$, the sensitivity is 0.1 psi , and the sampling frequency

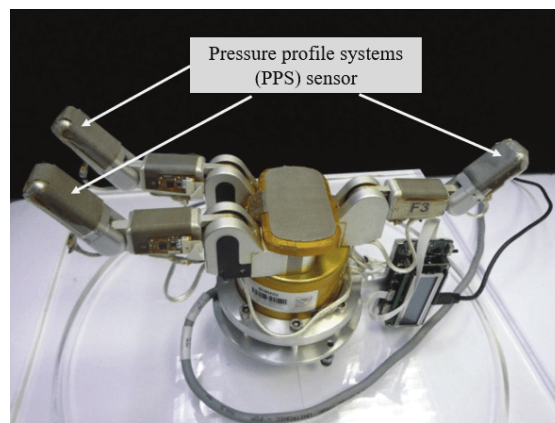


Figure 2.25: A Barrett Hand is equipped with PPS sensors on each of its fingertip [127].

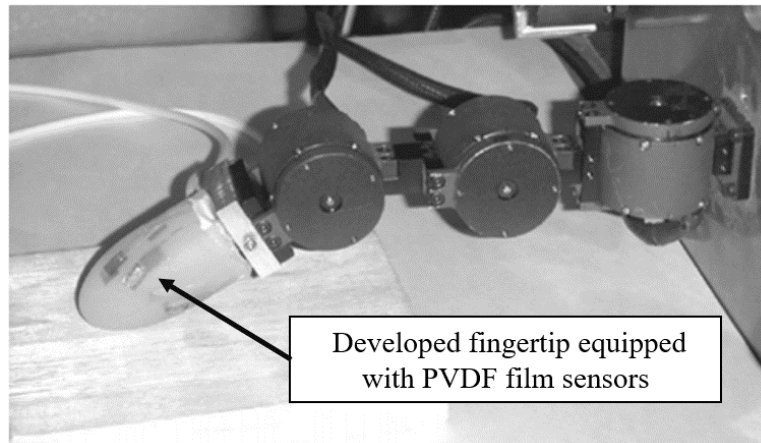
is 35 Hz.

To summarise, capacitance-based tactile sensing technology is one of the most commonly used methods at the moment, and it has also been put into commercial use (a typical example is the touch screen in current electrical devices). The advantages of this type of sensor include high sensitivity and small size.

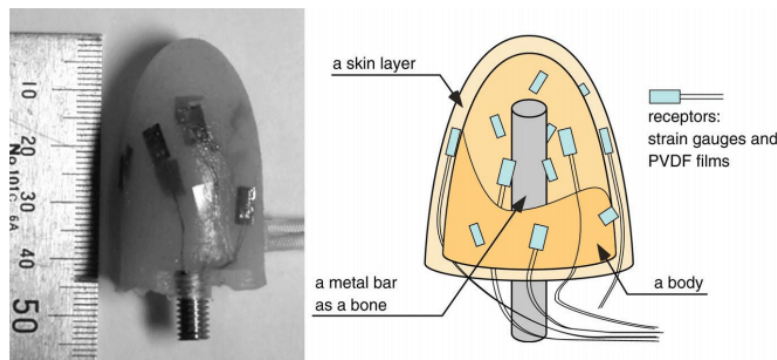
2.4.3 Piezoelectricity-based Sensing Technology

Piezoelectricity-based tactile sensors convert an external force or stress into an electric voltage; the so-called conversion is also known as the piezoelectric effect [144]. It is noted that the sensing cells within the sensor body do not need an electrical power supply due to the use of piezoelectric materials, which makes the sensor fairly applicable in situations where small-scaled sensors are needed. Piezoelectric materials include ceramics, crystals, and polymers. Among all these piezoelectric materials, polymer polyvinylidene fluoride (polymer polyvinylidene fluoride (PVDF)) films is the most commonly used one in tactile sensor designs due to its high piezoelectric coefficients, low weight, mechanical flexibility, chemical inertness, and dimensional stability [87].

A typical example of the piezoelectricity-based tactile sensor is the polymer polyvinylidene fluoride (PVDF) film sensor proposed by Hosoda et al. [61]. As shown in Fig. 2.26, a biomimetic artificial fingertip is made by combining strain gauges and PVDF film sensors into a silicone-made skin layer, together with a metal bar which acts as the phalanxes. The mixture of strain gauges and PVDF film sensors can be regarded as the tactile receptors of the biomimetic fingertip to detect the external mechanical stimuli. When mounted at the tip of a robot finger (shown in Fig. 2.26(a)), the sensor is able to discriminate between different materials via pushing and rubbing the corresponding objects. Hosoda et al. have further explored the design and have expanded the sensor system to include a tactile skin for flat areas [149], allowing it to be applied within the palm area of a robot hand. However, the use of various electrical components as tactile receptors creates an excess of wiring making this type of sensor complex to be manufactured.



(a)



(b)

Figure 2.26: Developed fingertip equipped with PVDF film sensors [61]. (a) An anthropomorphic fingertip is attached at the tip of a robot finger. (b) A developed fingertip (left) and its cross-sectional sketch drawing (right): The fingertip is made up of a metal bar, a body, and a skin layer inspired by the structure of the human finger. The body and the skin layer are made of different kinds of silicone rubber. Polymer polyvinylidene fluoride (PVDF) films and strain gauges are embedded randomly inside as tactile receptors.

Also, the fabrication of artificial skin for the entire hand can be difficult.

To summarise, piezoelectricity-based tactile sensing technology is widely used at present [73]. The advantages of this type of sensor include high sensitivity, reliability, and excellent frequency responses. However, it can only measure dynamic forces due to the fact that its voltage output drops over time [126].

2.4.4 Organic Field-effect Transistors (OFETs) Sensing Technology

Organic Field-effect Transistors (OFETs) can be directly used in tactile sensor design as they can detect the pressure information; a number of sensors have been built based on this sensing design. For example, Darlinski et al. [38] directly place pentacene OFETs on a rigid surface as the pressure sensing elements in their sensor. Manunza et al. also use pentacene OFETs in their flexible sensors [101] [100] and the transistors show the capability for both pressure sensing and switching. OFETs are fabricated on a $1.6\ \mu\text{m}$ thick Mylar foil and the foil acts both as the carrier substrate and the gate dielectric for mechanical support. The sensors show a linear current response with the applied pressure. Further, they present 3×3 tactile sensor arrays [33] based on the same technology, as shown in Fig. 2.27(a). The sensor consists of 9 pentacene OFETs, as shown in Fig. 2.27(b), and each of the sensing elements can be switched on individually. The sensor has an overall spatial resolution of $7\ \text{mm}$.

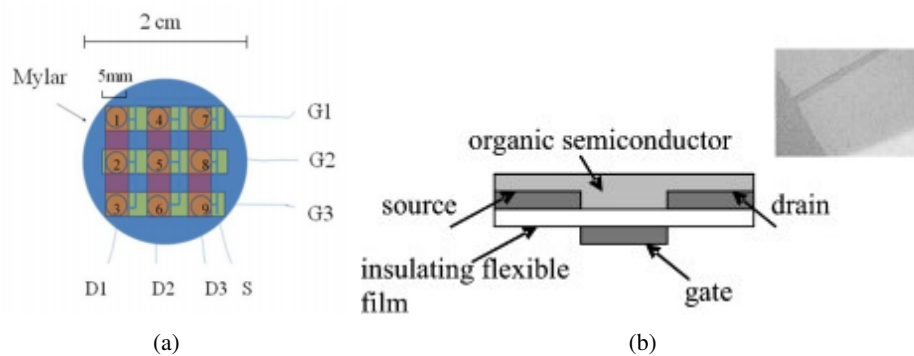


Figure 2.27: Arrays of pressure sensors based on OFETs [33]. (a) The schematic design of the employed array configuration. (b) The cross-section view of substrate-free OFETs for each sensing element.

Mannsfeld et al. present another array of pressure sensor [99] (shown in Fig. 2.28), with the use of OFETs. In this sensor, an elastomer made of polydimethylsiloxane (PDMS) is used as the dielectric layer and the OFETs can be used as a pressure sensor based on the mechanical deformation of the elastomer. Besides, the output current of the OFETs is directly related to

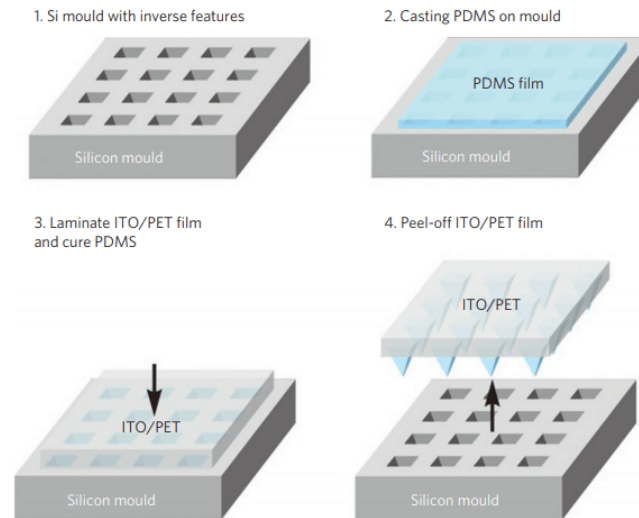


Figure 2.28: Fabrication of the arrays of pressure sensor [99] with microstructured rubber dielectric layers.

their capacitance. The sensor has very high sensitivity and a reduced relaxation time due to the microstructuring process of the PDMS layer. Specifically, the sensor has a sensitivity of $1 \mu A/kPa$ under $2 kPa$ pressures and $0.3 \mu A/kPa$ for pressures between $2 - 18 kPa$.

To summarise, the OFETs sensing technology has the advantages of simplified fabrication with the use of OFETs as the direct pressure sensing element, as well as high sensitivity. However, the application of OFETs for tactile sensing always requires a reference electrode [153].

2.4.5 Magnetic-based Sensing Technology

Magnetic-based tactile sensing technology is based on magneto-elastic materials (for example, permanent magnets, or permanent magnetic nanocomposite material), whose magnetic field values can be altered via the displacement of the material's location or the deformation of the material's structure when an external force is exerted. In order to measure the change of the magnetic field, some tactile sensors use magnetic Hall effect sensor [106] as the receptor to measure the magnitude of the magnetic field, while others use giant magneto-resistance (GMR) (its resistance gets changed when external magnetic field alters) sensors [17] as the receptors in-

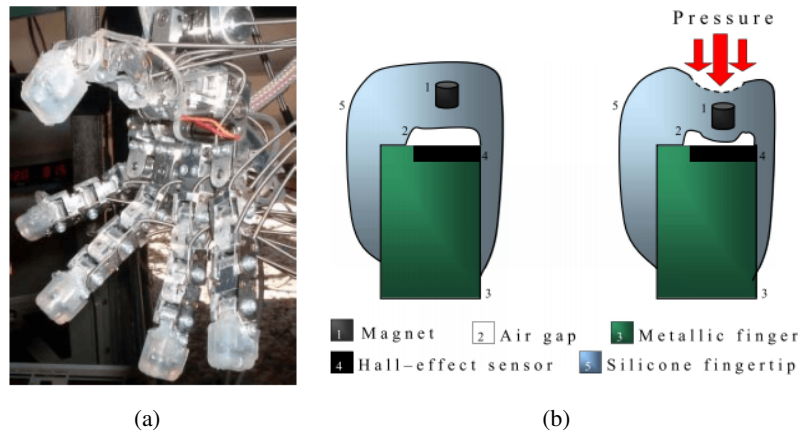


Figure 2.29: Highly sensitive soft magnetic-based tactile sensors [66]. (a) An anthropomorphic robotic hand equipped with 17 tactile sensing elements. (b) The structure of the sensor and the sensing principle. Note the presence of an air gap between the silicone shell and the Hall effect sensor increases the sensitivity of the sensor system.

stead. All in all, the exerted force can be calculated by detecting the receptor's electrical signals (can be voltage, current or resistances).

A typical example is a soft magnetic-based tactile sensor proposed by Jamone et al. [66], as shown in Fig. 2.29. The sensor is small enough to be mounted on an anthropomorphic robotic hand in the form of a phalangeal sensor and fingertip sensor model. As shown in Fig. 2.29(b), the sensor is made of a silicone body with a small permanent magnet placed inside. A hall-effect sensor is placed underneath the silicone body to measure the magnetic field generated by the immersed magnet. It is noted that there is also an air gap between the silicone body and the hall-effect sensor, and this gap helps increase the sensitivity of the system. When an external force is applied on the surface of the silicone body, it leads to a displacement of the immersed magnet moving towards the hall-effect sensor, while the intensity of the magnetic field around the sensor increases, resulting in an increasing output voltage signal. When the force is released, the situation is just the opposite. Specifically, the minimum sensed force is 0.01 N for the phalangeal sensor model and 0.05 N for the fingertip sensor model.

To summarise, magnetic-based tactile sensing technology has the advantages of mechani-

cal flexibility, robustness, and low hysteresis. However, the requirement for the electrical and magnetic components leads to issues of complexity concerning the wiring.

2.4.6 Optical-based Sensing Technology

Optical-based tactile sensing technology has become an attractive topic in the past few years as the rapid development of advanced optical systems enable the utilization of tactile sensors in small volumes. Current optical-based tactile sensors include optical components such as optoelectronics [85, 26], optical fibres [104, 53] and camera [96, 63]. There has been a surge of interest in vision-based sensing technology with the use of cameras [45, 70, 155, 64, 170, 80] due to increasingly developed computer vision techniques. This type of tactile sensor uses high spatial resolution, small-sized camera to detect the tactile information via image processing. Typical examples of vision-based tactile sensors are presented below.

The TacTip sensor [160] is a biologically inspired sensing device with a dome structure. There are currently six different versions of this sensor: open-TacTip (original), Tac-Tip (improved), TacTip-GR2, TacTip-M2 (flat), TacTip-M2 (round), and TacCylinder, as shown in Fig. 2.30(d). Fig. 2.30(a) shows a schematic representation of the original sensor, while the structure is slightly different in the succeeding generations. However, the entire TacTip family shares a similar working principle. There is a silicone outer skin with inward-facing nodule pins, and the inside of the sensor is filled with a clear, compliant gelatinous polymer placed on a lens. To provide a better understanding, a schematic of a 3D printed mould of a 20-mm-diameter fingertip TacTip device [166] is shown in Fig. 2.30(b). The sensor uses LEDs as the light source, and a camera is placed at the bottom to capture the images of the skin deformation via a clear lens. The image is initially captured in a colour format (see Fig. 2.30(c)), which is subsequently converted into grayscale. Then, the grayscale image is subjected to thresholding to create the pixel distribution map, in which the movement of each pin (white pixel) compared with its untouched status can be observed and evaluated. The distance of pixel movements can be translated into the intensity of the applied force.

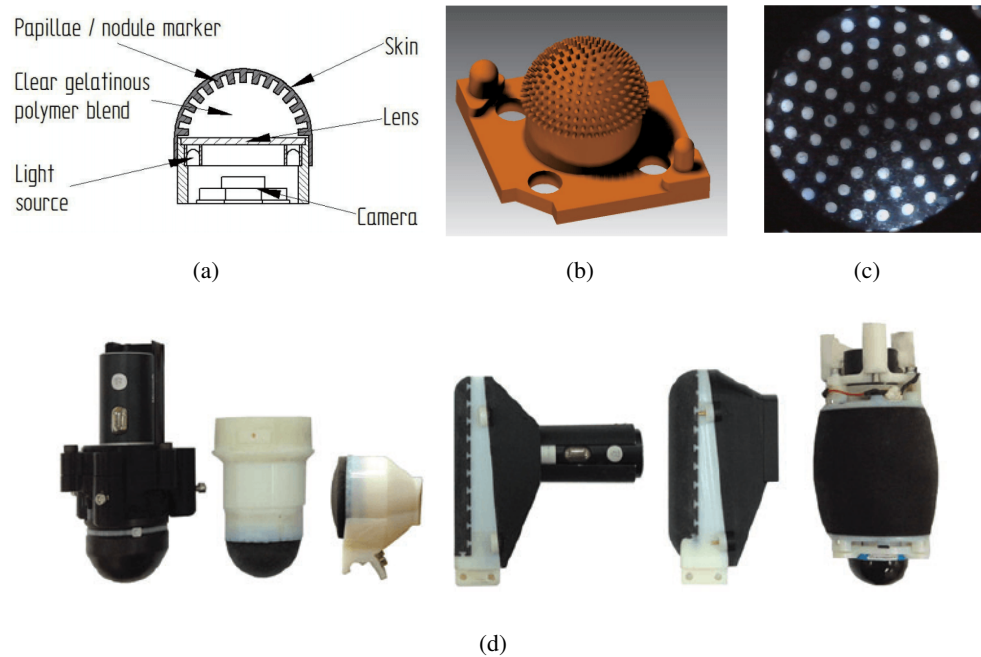


Figure 2.30: The TacTip family soft optical tactile sensors [160]. (a) The schematic design of the original TacTip sensor. (b) A 3D printed mould assembly of the 20mm-diameter fingertip TacTip device [166]. (c) The raw image capture without object contact by the fingertip TacTip device. (d) TacTip family sensors. From left to right are open-TacTip (original), Tac-Tip (improved), TacTip-GR2, TacTip-M2 (flat), TacTip-M2 (round), and TacCylinder.

The optical three-axis tactile sensor [114, 113] is a dome-like robotic finger that is capable of sensing normal and shear forces. Fig. 2.31(a) presents a schematic representation of the proposed sensor [115]. The sensor is 27 mm in diameter and 42.6 mm in height. It consists of 41 sensing elements made of silicone rubber attached to a hemisphere-shape acrylic dome with the features of a flange structure to attach all sensing elements. Each sensing element consists of a columnar feeler (height: 3 mm) and eight conical feelers (height: 0.3 mm). The sensor uses optical fibres as the light source, and a CCD camera is placed at the bottom acquiring images of the feelers on the dome being deformed by the interaction with objects. An integrated sensor prototype [112] is shown in Fig. 2.31(b). The image captured by the camera is divided into 41 regions, as shown in Fig. 2.31(c), and several steps are required for the image processing. These

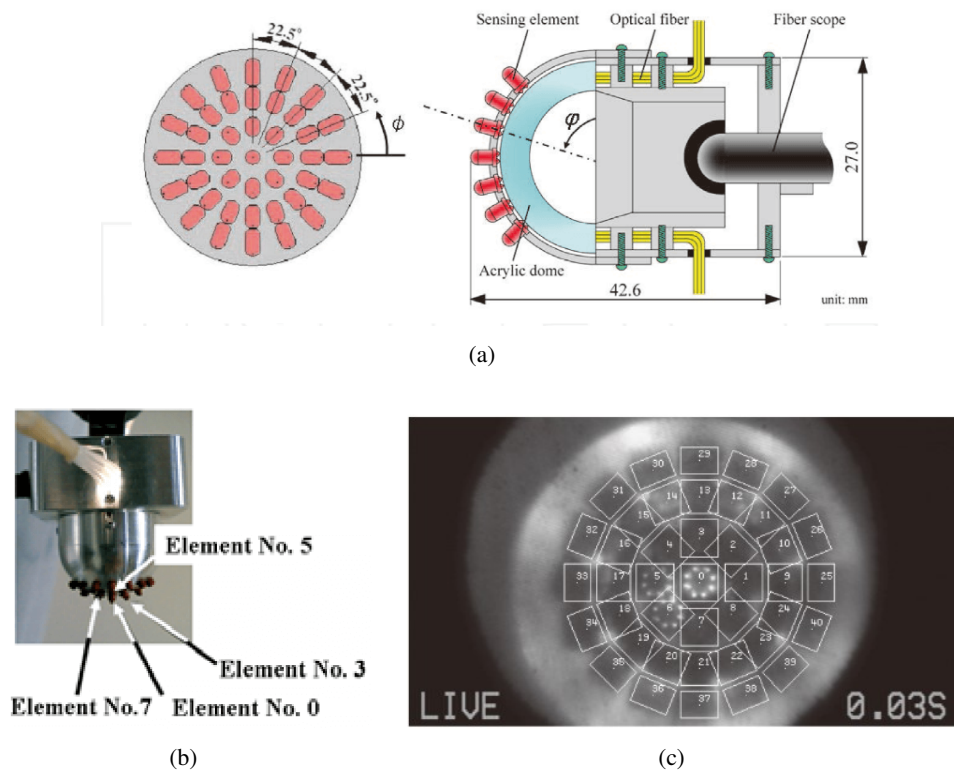


Figure 2.31: Optical three-axis tactile sensor [112]. (a) The schematic design of the fingertip three-axis tactile sensor. (b) The sensor prototype. (c) The raw image with the address of sensing elements captured by the sensor.

steps include a division procedure, digital filtering, and integrated grayscale value, and centroid displacement calculations. Both the pixel grayscale value and the centroid displacement of each sensing element can be translated into the intensity of the applied force.

Another vision-based tactile sensor proposed by Kamiyama et al. [71] has been developed with twin layers of markers inserted into a rubber covering. As shown in Fig. 2.32(a) and Fig. 2.32(b), it is a large, flat sensor; a camera is applied to capture the position of each blue and red marker in the x, y plane, where the blue and red markers are located under different depth. The researchers used a simplified mechanical model to calculate the normal and shear forces during point contact. Later on, they scaled the sensor size down to a robot fingertip (as shown in Fig. 2.32(c)) and named the device ‘GelForce sensor’ [136].

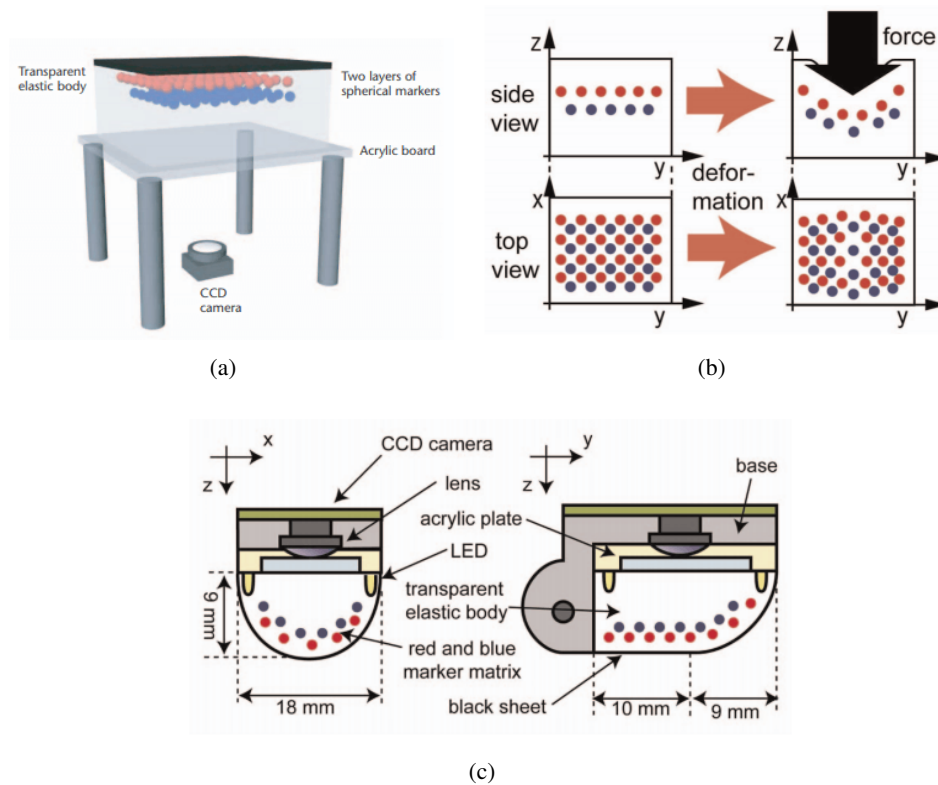


Figure 2.32: GelForce tactile sensor [71, 136]. (a) The schematic design of the initial sensor. (b) Representing depth information through colour. (c) The schematic design of the finger-shaped GelForce sensor.

Johnson et al. introduced a novel device [68] that can be used as a 2.5D scanner to reconstruct the contact surface shape and texture, as shown in Fig. 2.33. On the basis of this early version of the so-called elastomeric sensor [69], Li et al. [92] introduced a fingertip GelSight tactile sensor, as shown in Fig. 2.34. As described in [176], the GelSight tactile sensor uses a deformable elastomer piece as the medium of contact, and an embedded camera is placed at the foot of the sensor to capture the deformation of the elastomer surface. The initial elastomeric sensor prototype [68] was developed without any markers on the elastomer. A later version of the GelSight sensor [178] features small black markers painted along with the entire deformable elastomer, and the motion of the markers provides information about both normal and shear



Figure 2.33: Illustration of the GelSight [68] operating concept. A cookie is pressed against the skin of an elastomer, and the shape can be measured via the photometric stereo and rendered at a novel viewpoint.

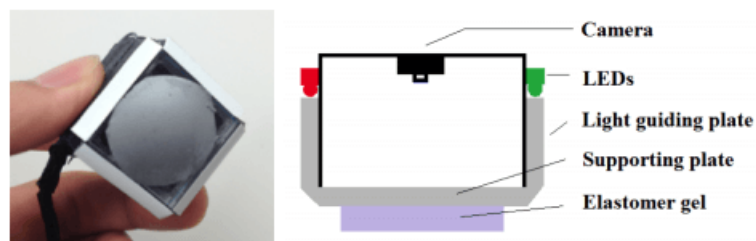


Figure 2.34: GelSight sensor (without marker) [92] prototype and its schematic design.

forces, as shown in Fig. 2.35. The GelSight sensor can easily capture the detailed shape and texture of the contact object, which makes it useful for material recognition and hardness estimation [180]. Later on, another improved version of the GelSight sensor (shown in Fig. 2.36) was developed by Dong et al. [42], with the use of a Lambertian membrane and a new illumination system. The high-resolution three-dimensional geometry of the contact surface can be reconstructed from the camera images by using photometric stereo techniques with relatively high accuracy. It is noted that in the GelSight sensor [179], the force measurement is correlated to its tactile image (geometry) due to the presence of numerous markers merging with the tactile information in the image.

In general, optical vision-based tactile sensors use soft and deformable materials as the sensing medium. The deformation of a material can be monitored by camera via which tactile information can be acquired. The compliance of elastomeric materials give the tactile sensor the

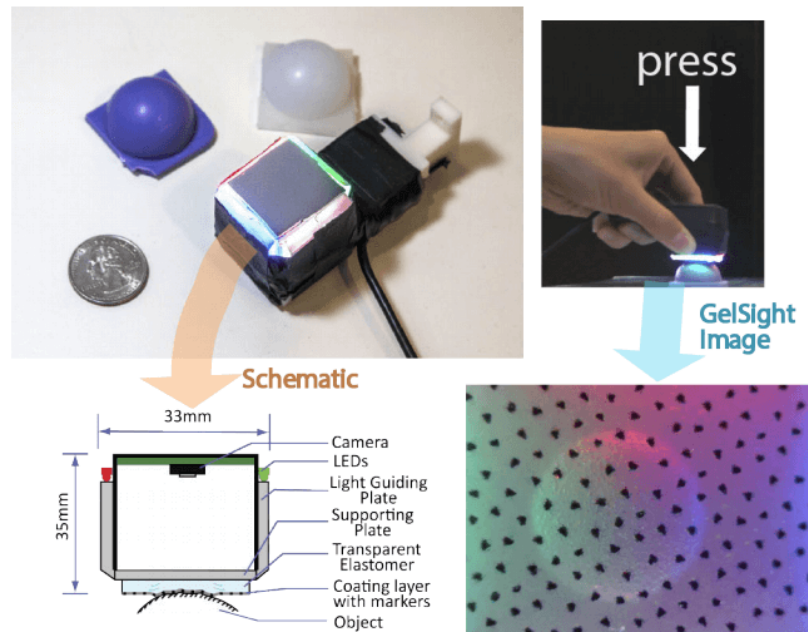


Figure 2.35: GelSight sensor (with marker) [180] prototype, together with its schematic design and captured view.

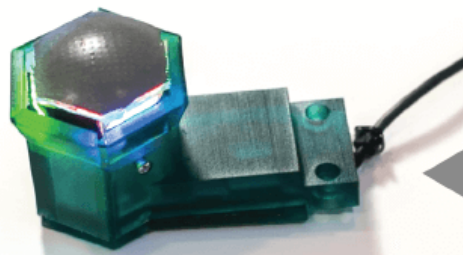


Figure 2.36: Improved GelSight sensor [42] prototype.

ability to adapt to curved or irregular surfaces during the manipulation of objects. For instance, a compliant tactile sensor mounted on a fingertip or an end-effector of a robot is useful for grasping different types of objects. To conclude, the vision-based tactile sensor has high spatial resolution and the capability for multiple tactile information acquisition. However, this type of technology requires complex computation to achieve the needed image processing, and the

viscosity of the soft material can cause hysteresis which affect the sensor accuracy.

2.5 Summary

This chapter has presented an overview of different sensing technologies that have been applied in force and tactile sensing in robotics. Concerning force sensing, different sensing technologies (semiconductor strain gauges (SSGs), capacitive strain gauging, Fibre Bragg Gratings (FBG), and electrical resistance strain gauges (ERSGs)) are typically integrated with mechanical structures (such as cross-beam structure, Stewart platform, and cantilever structure). The strain gauge is one of the most well-developed and commercialised technologies to date. However, there exists a trade-off between the sensitivity and the stiffness of the sensor structure. The optical-based force sensing approach which consists of optoelectronic components, optical fibres and cameras is also widely applied. With the rapid advancements in camera miniaturisation, size is not a very big issue for this type of sensor any more. The resistance-based tactile sensor is widely used and has been commercialised at present. However, it still suffers from hysteresis. The capacitance-based tactile sensor is also commonly-used nowadays, and the majority of touch screens are based on this technology. It has high sensitivity and can be miniaturised; however, a sudden electrostatic discharge may occur and produce noise requiring complex electronic filtering system to be implemented. A piezoelectricity-based tactile sensor can be miniaturised as well, but it can only measure dynamic forces, a fact that limits its application. The tactile sensor that uses organic field-effect transistors (OFETs) is relatively simple to fabricate; however, it always requires a reference electrode. A magnetic-based tactile sensor has low hysteresis, but it usually suffers from complex wiring issue. The optical-based tactile sensor, particularly the camera-based version, has become popular in the last few years, because of the increasingly developed computer vision technology and camera miniaturisation. However, the main issue of this type of sensor is the computational complexity of tactile information processing.

From the above review, we can see that the majority of the research is focused on the development of either a multi-axis force sensor or a tactile sensor. The robotic force and tactile

sensing system proposed in this thesis aims to put forward a concept of an integrated camera-based sensor capable of concurrent force and tactile sensing. Compared to other force and tactile sensing techniques, the advantages of a camera-based sensor include

1. high spatial resolution (the sensing elements are theoretically the pixels within the images);
2. customised-shape of the sensing medium (flat-shaped, dome-shaped or other different shaped elastomer);
3. simultaneous force and tactile sensing within one image (an image can contain multiple information), meanwhile, deep learning and other vision-based techniques can be directly applied as vision and learning has developed a lot recently;
4. miniaturised sensor can be achieved with the development of small cameras.

Therefore, we have chosen to explore the optical vision-based sensing technology, as it uses a camera that can provide a high spatial resolution and, most importantly, is capable of sensing dual modalities (force information and tactile information in our case) by processing a single image. The methodology of concurrent force and tactile sensing within an integrated device is introduced in the following chapter.

Chapter 3

Dual-Modality Sensor Methodology

3.1 Introduction

This chapter describes the concept of combination of force and tactile sensing within a single sensor. This chapter starts with the discussion of the theoretical model of a robotic force and tactile sensing system proposed in [34]. It proceeds with an analysis of both the force sensor structure and the tactile sensor structure. This is followed by an introduction to the methodology of the proposed optical dual-modality sensor structure that uses a single camera and a combination of an elastomer layer and an elastic structure. Finally, we discuss ways of miniaturising the sensor.

3.2 Dual-Modality Sensor Methodology

3.2.1 Robotic Force and Tactile Sensing System

One of the well-known theoretical models of a robotic force and tactile sensing system where different sensors of different functionalities are utilized and work together as an integrated system to perform force and tactile sensing is shown in Fig. 3.1(a). Force sensors are mounted between a robot fingertip's end and joint for force sensing, where the force information includes the multi-axis force/torque components measured along the x -, y -, and z - directions. Tactile sensors are mounted on the robot fingertip end for tactile sensing. Tactile information includes the mechanical stimulus detection of contact, slip, and pressure. This robotic force and tactile sensing system can be powerful when dealing with three types of activities: manipulation, exploration, and response, as shown in Fig. 3.1(b). For manipulation task, it has been studied within the fields of sensory integration therapy, physical therapy, developmental psychology, and medicine [125, 123, 41, 147, 124]. A typical manipulation task is grasping an object which is a fine motor skill that develops naturally in both humans and animals. The key points of accomplishing a manipulation task depend on both the object-related parameters (for example, size, shape, weight, and texture of the object) and the manipulation related parameters (for example,

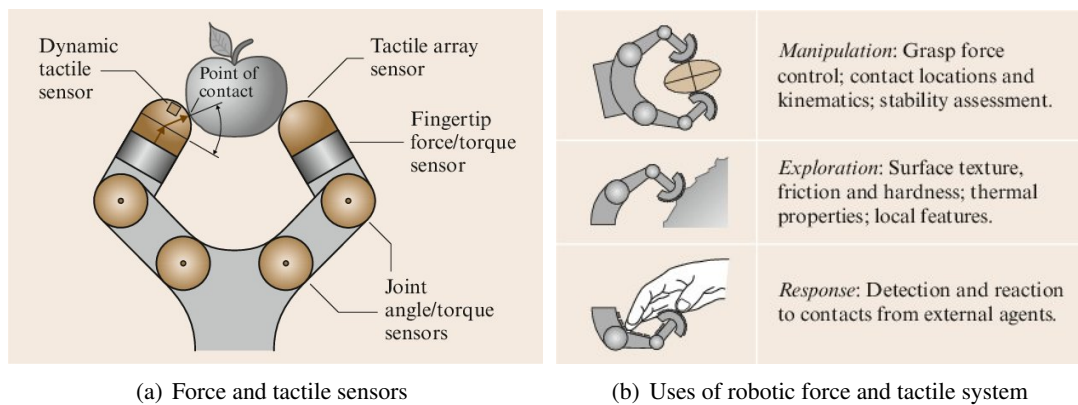


Figure 3.1: Introducing force and tactile sensing system and its uses in robotics [34].

speed, accuracy, and movement patterns) [175]. Force and tactile sensing is very important for tasks where an appropriate grasp force control, contact location and kinematics analysis, and stability assessment are required. With respect to exploration, a majority of the research is focused on exploring the contact materials and surface properties (for example, surface texture, friction and hardness, thermal properties, and local features). Some materials might not be easily distinguished by sight, as they share a similar appearance while force and tactile sensing can do the job perfectly via touch. A reasonable force and tactile sensing system gives a gentle response, while an inaccurate system can cause an impact on the operation process and damage the contact object surface.

3.2.2 Dual-Modality Sensing Principle

Force and tactile sensing has generated much research interest over past decades, for it admits of information gathering through direct physical contact between a sensing device and the contacted objects. The application of force and tactile sensing with respect to a robot's end effector is vital to achieving next-level grasping and manipulation performance. However, there is currently no other sensor out there that is capable of measuring these two modalities in one housing.

Force sensors have seen extensive development over the past seven decades [150], and their capacity for multi-dimensional force/torque measurement has made them very attractive across a broad swathe of robotic research. Various means of developing multi-axis force sensors have been proposed, including strain sensing technology [94, 25], cross-beam structure [171], Stewart platform [95], and optics [16]. Salient criteria to arrive at a desired force sensor design include considerations of accuracy, robustness, and reliability. Strain gauges were among the earliest and most commonly used technologies, and they have dominated the strain measurement and weighing industry. The ATI multi-axis force/torque sensor [2] uses silicon strain-gauge sensing technology to attain high sensitivity and repeatability and is one of the best-known force sensors currently on the market. Optical-based force sensors have also developed rapidly in recent years; a typical example is the OnRobot HEX force/torque sensor (formerly known as the

OptoForce sensor) [4]. Other than commercial sensors, many in-lab optical-based force sensors [117, 15, 109] have been proposed which make use of optoelectrical components, optical fibres or cameras.

Tactile sensors have drawn interest for yet another reason: they are regarded as the future of robotic grasping [44]. As tactile information has become a key sensing modality, various technologies have been investigated to develop sensors [160, 96, 130] of this type. However, there is still room for development of the current tactile sensing devices due to the inherent complexity of understanding the sense of human touch and its replication in hardware. Many tactile sensors for robots are biologically inspired [65, 93], where the aim is to imitate the human ability to obtain tactile feedback. Among the different methods that have been applied towards realizing tactile sensors are ones that rely on resistance [19], capacitance [40], piezoelectricity [73], organic field-effect transistors (OFETs) [169], optics [83], and magnetics [60]. Most of the tactile sensors used on robots are designed for fitting onto fingertip-shaped appendages or gripper end-effectors [92, 43], while others are designed to be mounted on the body of a robot [98]. The latter has a larger sensing area and are mostly used for contact and collision detection during robot motion.

There are major challenges [175] in developing a desired artificial force and tactile sensor. Firstly, the sensor needs to be small in order to be of a size compatible with standard robots. Secondly, it should at all times, provide real-time force and tactile feedback with good signal quality. Thirdly, the sensor should be reproducible, so as to enable other researchers to duplicate it. Fourthly, it ought to be able to measure normal force as well as shear force and torque. Finally, the sensor should be able to handle multi-point touch, not only single-point, with an evenly distributed contact area where each local tactile element ideally has the same characteristics.

In amongst the myriad different sensing technologies, spanning both force and tactile sensors, optical sensors using cameras have a lot to recommend them. This type of sensor can provide a high spatial resolution and, crucially, can sense multiple modalities (such as contact force, contact surface geometry, and hardness) from analyzing a single captured image



(a) Robot end effectors equipped with force sensors and tactile sensors



(b) Robot end effectors equipped with proposed force and tactile sensor

Figure 3.2: Introducing the proposed force and tactile sensor within a robot system.

[139, 20, 69, 120, 93, 132]. Vision-based tactile sensors usually use soft and deformable materials as the sensing medium. Deformation of the material can be directly monitored through a camera or by observing changes to certain patterns on the sensing medium to acquire tactile information indirectly. Elastomeric materials offer compliance, which gives the tactile sensor the ability to adapt to curved or irregular surfaces during manipulation of objects. For instance, a compliant tactile sensor mounted on a fingertip or end-effector of a robot can assist with grasping different types of objects. Hence, a number of optical tactile sensors leverage deformation and compliance.

A major contribution of this thesis is to create a single integrated sensor that matches the high performance of stand-alone force and tactile sensors combined. As shown in Fig. 3.2, a tactile sensor is usually mounted on an end-effector end, while a small-volume force sensor is usually applied between the joint and the tactile sensor. We aimed to provide a force and tactile sensor that can be directly mounted at the robot end-effector end so that our sensor can achieve the same performances of both force and tactile sensors. According to the review in Sec. 2.3 and Sec. 2.4, we chose an optical method with the use of a camera as the transducer to sense both the modalities of force and tactile information within a combination of an elastic structure and an elastomer layer. The overall sensor structure is shown in Fig. 3.3, where a camera is fixed at the foot of the sensor; an elastomer layer is applied upon a supporting plate at the top of the sensor to perceive tactile information, and an elastic structure is applied between the elastomer layer and the camera to measure the force information. The tactile information (in the form of pressure or geometry) is detected by directly observing the deformation of the illuminated elastomer layer from the camera. Multi-axis forces and torques are measured by indirectly detecting the deformation of the force-sensitive elastic structure (via observing visible markers within the elastomer layer or visible markers attached to the elastic structure) with use of the same camera. Thus, a single sensor can simultaneously perform what is essentially multi-dimensional force/torque sensing and tactile sensing within the same housing.

The human tactile system has four mechanoreceptors, namely Pacinian corpuscle, Ruffini

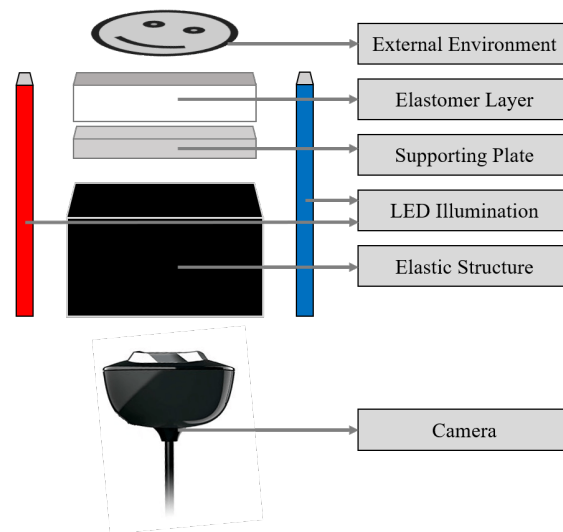


Figure 3.3: Sensing principle of the proposed dual-modality sensor design.

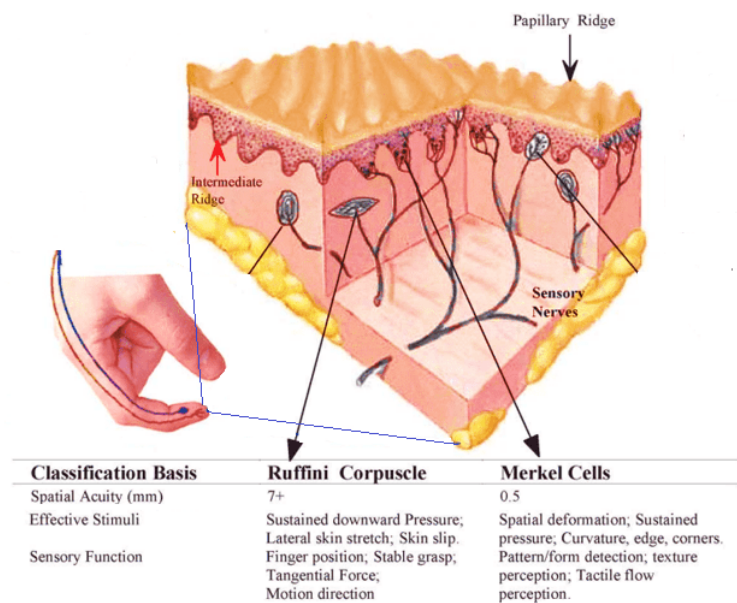


Figure 3.4: Section view of the human skin showing various mechanoreceptors [35]. Ruffini corpuscle (with low spatial resolution) is for force estimation (here corresponds to the elastic structure in our sensor structure) and is located beneath the Merkel cells (with high spatial resolution) which is for pressure and texture perception (here corresponds to the elastomer layer in our sensor structure). Sensory nerves correspond to the camera in our sensor structure.

corpuscle, Merkel cells, and Meissner's corpuscle. As shown in Fig. 3.4, these cells are located at different depths in the skin and are sensitive to different types of stimuli. In particular, Merkel cells are aligned with the intermediate ridge with a high spatial resolution (spatial acuity: 0.5 mm), are used for pressure and texture perception. Ruffini corpuscle is located beneath the intermediate ridge with a relatively sparse spatial resolution (spatial acuity: 7+ mm), and is responsible for force estimation. In our work, as can be seen in Fig. 3.3, the two core components within the proposed sensor structure are the elastomer layer (corresponding to the Merkel cells) and the elastic structure (corresponding to the Ruffini corpuscle). The combination of the elastomer layer and the elastic structure is regarded as the touch medium of the proposed sensor. When in contact with the external environment, both the deformation of the elastic structure (indirectly presented by the status change of a small number of markers) and the distortion of the elastomer layer (captured in the high-resolution tactile image) are recorded by the camera. Computer vision methods, which are competent at processing high-resolution image data, are then applied to analyse the acquired data for simultaneous force and tactile sensing. Note that compared with other vision-based tactile sensors, we used a separate force-sensitive elastic structure (this was also the principal internal structure inside a force sensor) to indirectly detect multi-axis force and torque quantities within the tactile image. Moreover, a supporting plate and LED arrays were included within the sensor structure. The elastomer layer is a relatively soft component, while the elastic structure is made of a more robust material, so in order to achieve a typical force sensor behaviour, a supporting plate (acrylic sheet) was mounted between the elastomer layer and the elastic structure to provide an overall deformation to the entire force structure. To create strictly controlled light conditions and prevent external light from interfering with the capture, we blocked the external light via the sensor shell, the elastomer coating layer, and used an internal illumination system (LED arrays). Note that the LED light colour, direction and position can influence the sensor performance.

To prove the validity of the sensing methodology, some typical force and tactile sensor prototypes are proposed, as shown in Fig. 3.5. All of them follow the same sensor architecture

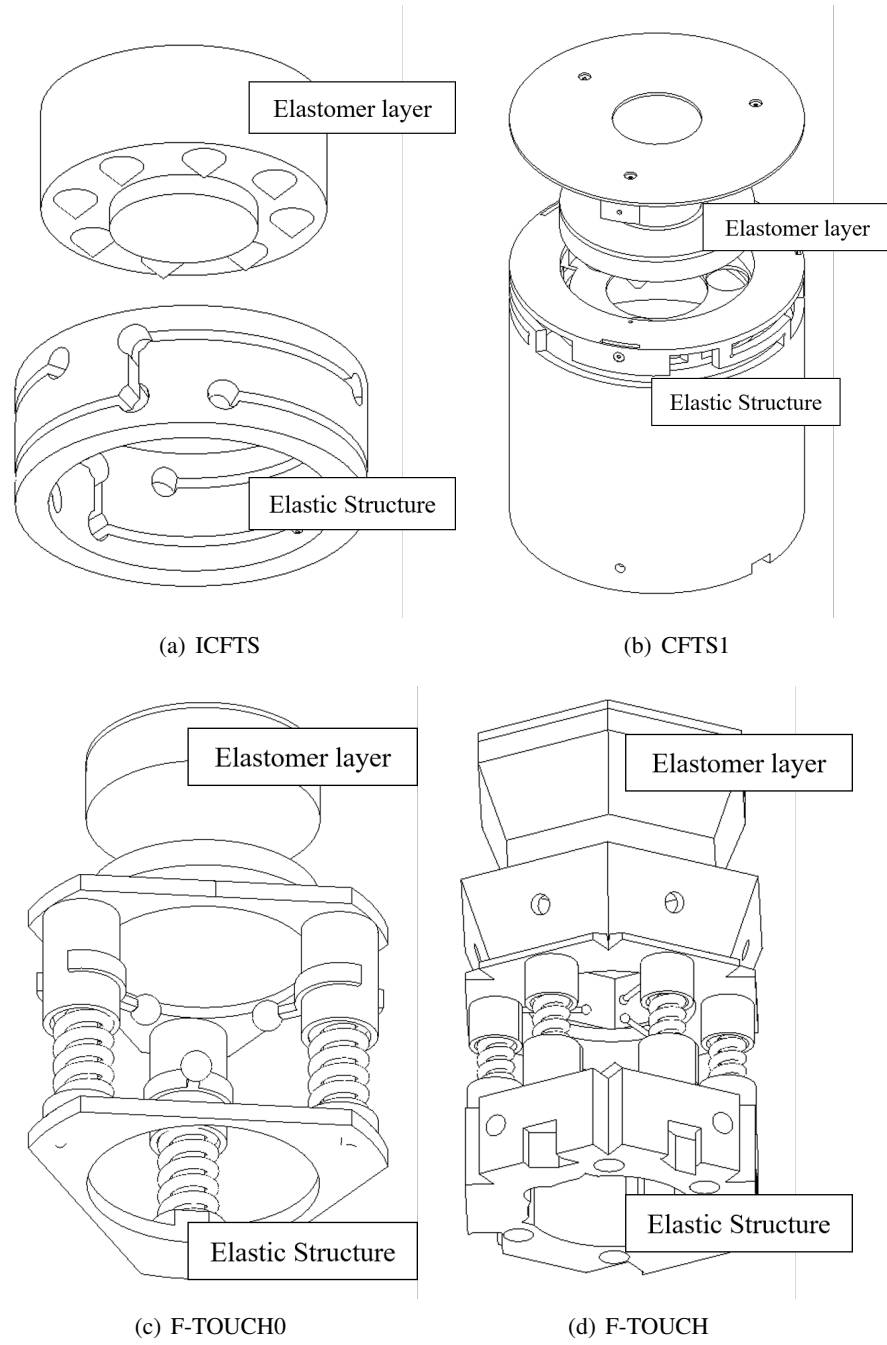


Figure 3.5: Typical sensor structures that consist of a combination of an elastomer layer and an elastic structure within the proposed F-TOUCH sensor prototypes.

with both an elastomer layer and an elastic structure above a camera. However, different elastomer, in terms of its shape, size, and material, and different elastic structures (for instance, a cantilever structure or a spring-mechanism structure) were used in each prototype. Fig. 3.5(a) shows the sensor structure of the ICFTS (Initial Camera-based Force/Tactile Sensor) which includes a compound elastomer layer whose the central area is a transparent silicone component, and its surroundings are covered in translucent silicone components with eight reflective conical force sensing elements. The elastic structure in this prototype is based on a mechanical cantilever beam structure. A detailed description and its working principle can be seen in Sec. 4.2. Fig. 3.5(b) shows a sensor structure of the CFTS1 (Camera-based Force/Tactile Sensor) whose compound elastomer layer has a central area consisting of numerous thin reflective conical tactile sensing elements, while the surrounding areas have three thick reflective conical force sensing elements. The elastic structure in this prototype is based on another more complex mechanical cantilever beam structure. A detailed description and its working principle can be seen in Sec. 4.4 and Fig. 3.7. Fig. 3.5(c) shows a sensor structure of the F-TOUCH0 with a coated elastomer layer (a piece of transparent silicone base coated with a thin reflective membrane). The elastic structure in this prototype is based on a mechanical spring-mechanism structure that uses three compression springs and three force markers attached within the force-sensitive structure. A detailed description and its working principle can be seen in Sec. 4.5. Fig. 3.5(d) shows a sensor structure of the F-TOUCH which has the same coated elastomer layer (a piece of transparent silicone base coated with a thin reflective membrane but in a considerably smaller size); the elastic structure in this prototype is based on a more complex mechanical spring-mechanism structure that uses six compression springs together with twenty-four small magnets and three tiny force markers attached within the force-sensitive structure. Each of the sensor prototypes and its performance will be introduced and discussed in the following chapters. A detailed description and its working principle can be seen in Sec. 4.5 and Fig. 3.8.

3.3 Concurrent Real-time Dual-Modality Sensing Using A Single Camera

After analysing both the force sensors and the tactile sensors, we found that a possible way to link these two modalities together was by using optical-based techniques, in particular, cameras.

Taking inspiration from the human tactile system (shown in Fig. 3.4), we propose a sensor structure whose sensor components correspond to human receptors tactile system (shown in Fig. 3.3). The elastomer layer corresponds to the Merkel cells for texture and pressure perception; the supporting plate corresponds to the intermediate ridge for supporting; the elastic structure corresponds to the Ruffini corpuscle for force perception, and the camera corresponds to the sensory nerves for transmitting signals.

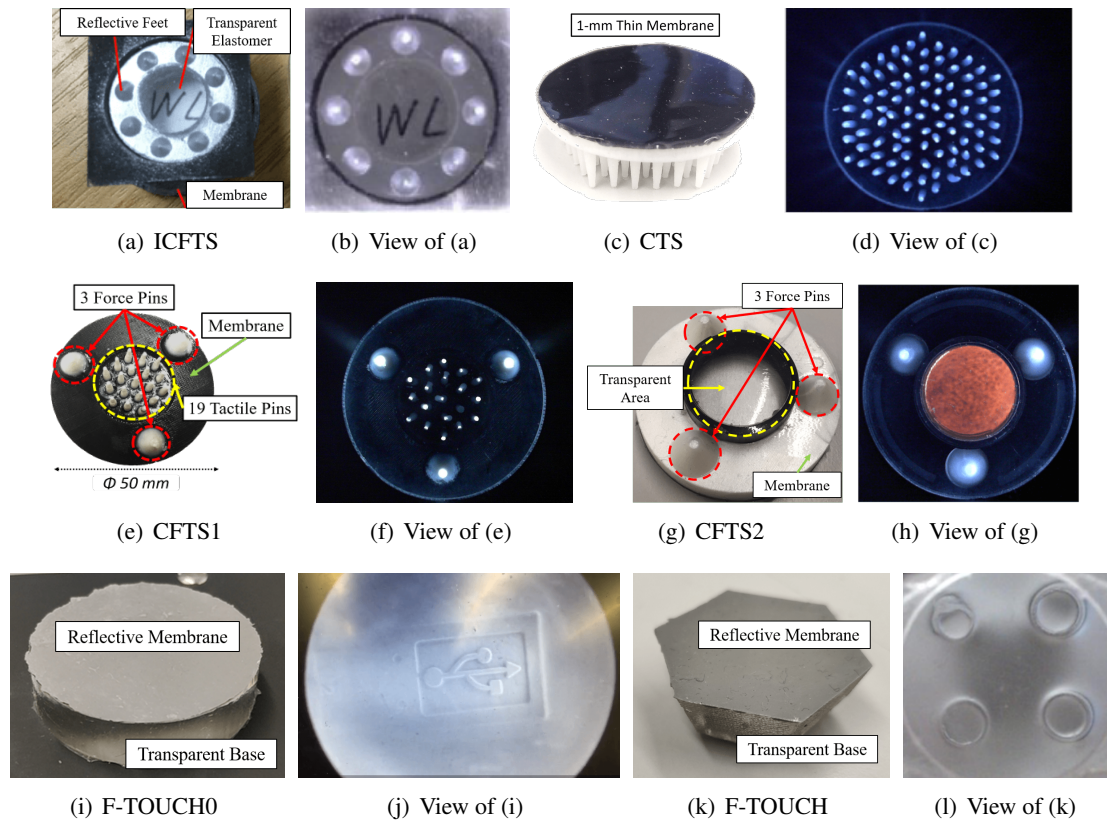


Figure 3.6: Typical elastomer layers manufactured in ICFTS, CTS, CFTS1, CFTS2, F-TOUCH0 and F-TOUCH for pressure detection in (d), (f) and geometry perception in (b), (g), (j) and (l), respectively.

In the proposed sensor architecture, an elastomer layer is placed at the top to acquire tactile information, more specifically, to detect pressure or geometry. The elastomer layer contains two main parts: an elastomer base and a coating layer. The elastomer base is always a soft silicone base, and the coating layer is usually an opaque layer of silicone mixture to block the external environment light. When choosing the elastomer base materials, several aspects have to be considered: hardness, transparency (for geometry observation), and complexity for fabrication. For pressure detection, the elastomer layer has to be stretchable to sustain the applied pressure, while its hardness needs to be adjusted to meet a specific measurement range. The common elastomer materials that we used for pressure detection are Ecoflex and Psycho Paint (both are platinum silicone from the Smooth-on company). For geometry observation, the elastomer base has to be transparent and stretchable to yield to different contact shapes. Also, the hardness of the elastomer can be manually adjusted by adding softener. We used Solaris (platinum silicone) from the Smooth-on company for making the transparent elastomer base. Note that all these silicone materials are easy to manufacture as we only need to mix Part A and Part B of the silicone, and pour the mixture into a mould, then wait for the silicone to cure. For the coating layer, we usually mix the silicone materials with a colourant (for example, a black colourant to block the external light) and then directly pour the mixture on top of the cured elastomer base, making the resultant silicone compound layer opaque. In particular, we add metallic powder when producing coating layer for the transparent silicone base as the powder can provide a matte surface effect which is better for geometry observation (the specular surface can easily generate light spots which interfere with the observation). Several elastomer layers made of silicone rubber are presented in Fig. 3.6: two of them have reflective conical feet for pressure detection that are elastomers of CTS and CFTS1, while the other is transparent for geometry observation that is the elastomer of F-TOUCH0. More details including manufacturing process and material, will be shown in Chap. 4.

Another important component in the proposed sensing architecture is the elastic structure that is placed beneath the elastomer layer. This mechanical structure is also deformable (with

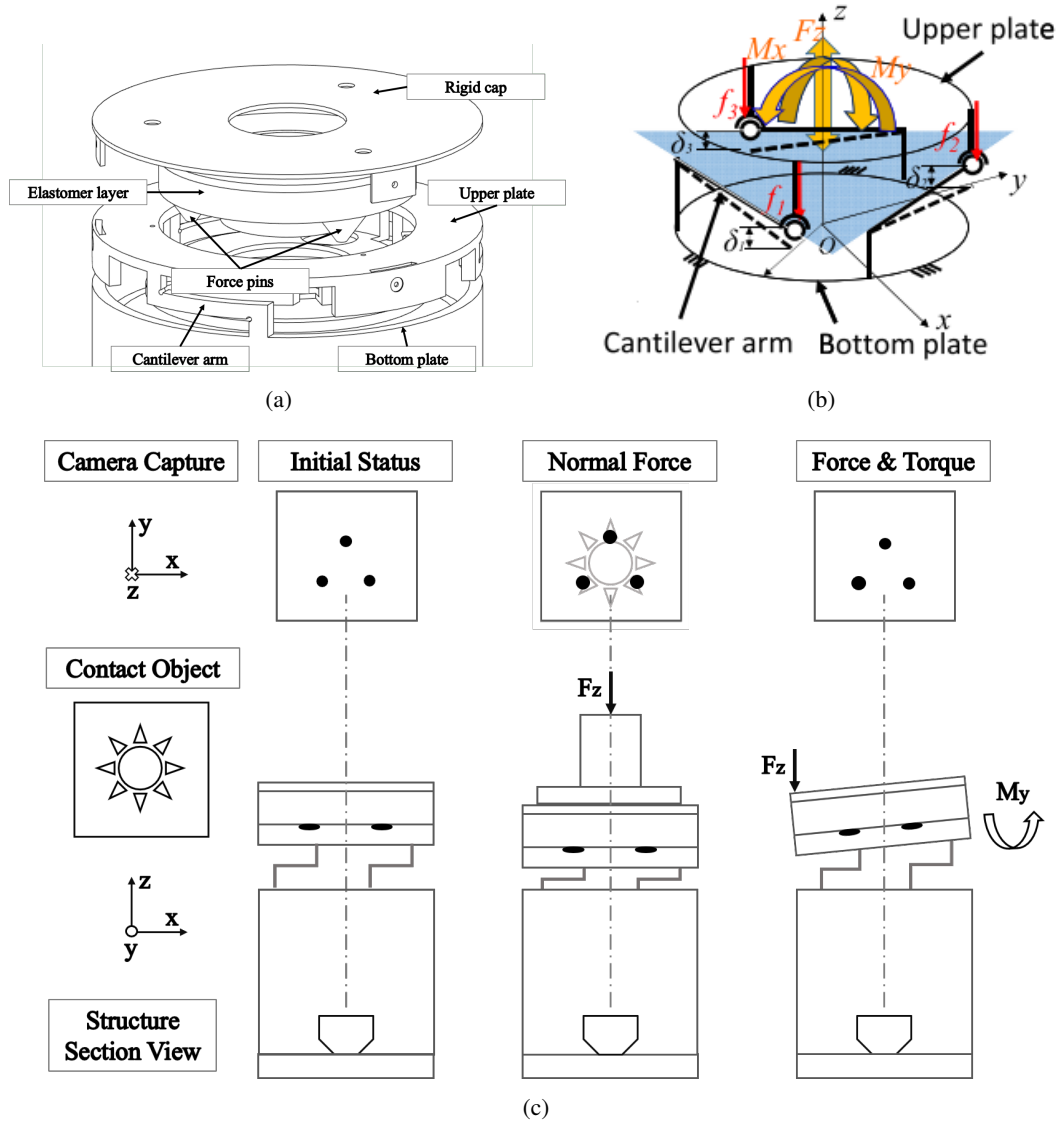


Figure 3.7: Cantilever structure used within the proposed sensor CFTS1. (a) Exploded view of the proposed sensor structure. (b) Measurable force and moment components on the sensor structure. (c) Sensing principle of the prototype that uses cantilever structure and the elastomer layer. The top row shows the camera capture when different forces and torques are exerted upon the sensor. The force and torque quantities can be estimated by analysing the status changes of the three force pins shown in the camera capture. Meanwhile, high-resolution tactile images can be observed from the same capture.

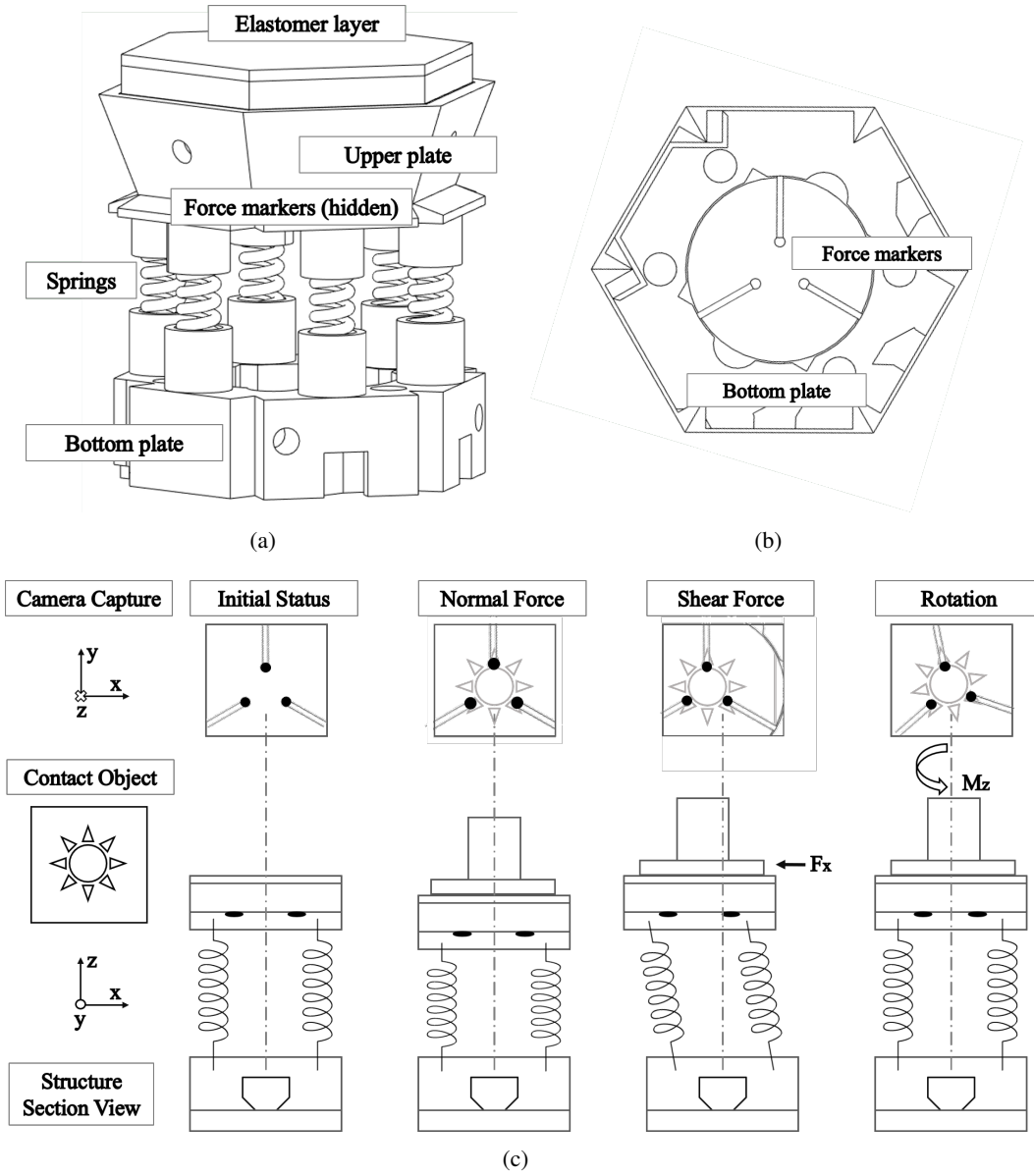


Figure 3.8: Spring mechanism structure used within the proposed sensor F-TOUCH. (a) Schematic view of the proposed sensor structure. (b) Bottom view of the proposed sensor structure. (c) Sensing principle of the prototype that uses spring mechanism structure and the elastomer layer. The top row shows the camera capture when different forces and torques are exerted upon the sensor. The force and torque quantities can be estimated by analysing the status changes of the three force pins shown in the camera capture. Meanwhile, high-resolution tactile images can be observed from the same capture.

linearity characteristics) and is used for force measurement. Two successful structures that are used in the developed sensor prototypes are the cantilever structure in CFTS1 (see Fig. 3.7) and the spring structure in F-TOUCH (see Fig. 3.8). Cantilever structure is a typical mechanical design used for three-axis force sensor [111]. The structure has three cantilever arms that are symmetrically located at 120° at the same radial distance, as shown in Fig. 3.7(b). Note that an elastomer layer (with force pins) is inserted inside of the cantilever structure (see Fig. 3.7(a)). When external forces are applied to the upper plate, the three associated cantilever arms will be deflected. The cantilever arm deflections (δ_1 , δ_2 , and δ_3) between the upper plate and the bottom plate can be indirectly represented in terms of the status change of the three force pins (shown in Fig. 3.7(c)) within the camera capture. More details will be provided in the sensor prototype section in Chap. 4. Regarding the spring structure, it can be used in multi-axis force sensor design [116]. As can be seen in Fig. 3.8(a), the sensor consists of three parts: a bottom plate, an upper plate and six springs that connect both plates. With such configuration, the upper plate can move in all directions (six degrees of freedom) with respect to the bottom plate. Furthermore, three force markers were inserted to the underside of the upper plate (therefore, the markers always keep the same pace with the upper plate movement, see Fig. 3.8(b)). Based on the force sensor analysis in the previous chapter, the movement (translation and rotation) and the area changes of the three force markers should have a linear relationship with the applied forces and torques due to this spring mechanism design. Then, we use a commercial multi-axis force/torque sensor to calibrate the proposed sensor (using regression methods), and given a known linear fit, the proposed sensor can estimate multi-axis force and torque values. Note that since the force markers are inserted at the bottom side of the upper plate, the camera can therefore capture both the force markers and the elastomer layer surface during the interaction, as shown in Fig. 3.8(c). Moreover, the tactile image (capture of elastomer surface) has relatively high spatial resolution compared to the three force markers within the elastic structure, which is consistent with the human tactile system architecture shown in Fig. 3.4.

As described above, we have placed a single camera at the bottom of the structure to capture

the deformations of both the elastomer layer and the elastic structure (indirectly represented by the status changes of the force markers) for tactile (pressure or geometry) and force sensing. For tactile perception, we apply an artificial neural network (ANN) for texture classification, and for force measurement, we apply linear regression method for multi-axis forces and torques estimation. Since only three black markers represent the force information, and the elastomer surface is illuminated by RGB colour, it is feasible to extract the force markers from the tactile image with simple thresholding. This scheme ensures the resource efficiency for dual-modality sensing since only one capture is required for obtaining two modalities information. Also, all processing is in real-time (with a frame rate of 15 fps). Several developed sensor prototypes will be presented in the next chapter to provide a more detailed explanation of each sensing principle.

3.4 Miniaturisation of Dual-Modality Sensor

Following the basic methodology of real-time dual-modality sensing using a single camera, we also considered reducing the sensor size to fit the standard robot end effector. The sensor miniaturisation can be considered from the following aspects:

1. **Elastomer layer:** the miniaturisation of the elastomer layer is feasible by using a small 3D-printed mould (around 20 mm in width and 12 mm in height). Then, we can easily obtain a small elastomer layer with the same manufacturing procedures described above.
2. **Supporting plate:** thin acrylic sheet (1 mm thickness) can be cut in small shape as the new supporting plate.
3. **Elastic structure:** taking the spring structure as an example, we can use small springs (of 15 mm length, 4 mm in diameter, and of 0.5 mm wire diameter), and small 3D-printed upper plate and bottom plate.
4. **LED illumination:** surface mounted diode (SMD) LED can be applied on a thin printed circuit board (PCB) of 1.5 mm in height.
5. **Camera:** small webcam (Logitech C310) can be used to replace the original Microsoft

lifecam studio.

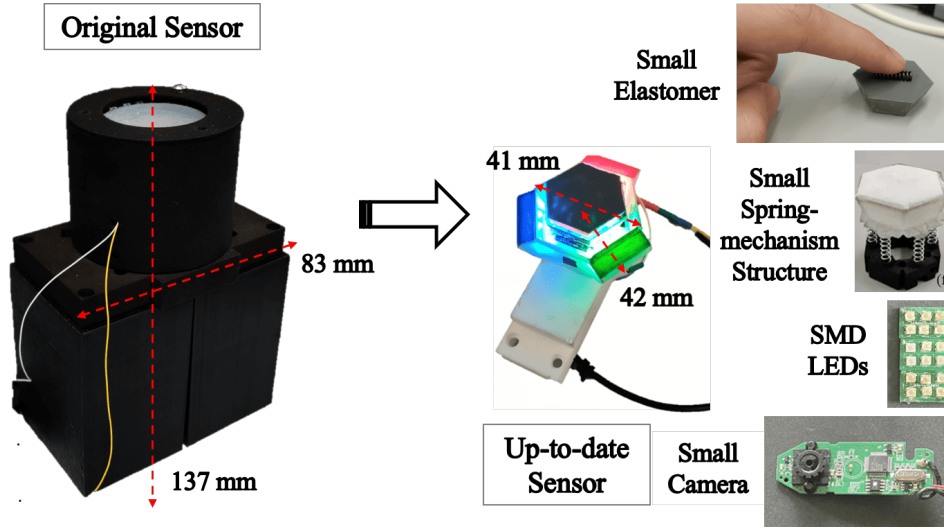


Figure 3.9: Comparison between the original sensor F-TOUCH0 (left, in large-scale) and the revised sensor F-TOUCH (right, in small-scale).

Following these aspects, we built a miniaturised sensor F-TOUCH (42 mm in height, and 41 mm in width) from the old-version sensor F-TOUCH0 (137 mm in height, 83 mm in width), as shown in Fig. 3.9. The revised sensor can be mounted on a commercial gripper and the connection is via two USB cables (one is for the webcam and the other is for the LED power supply). A detailed description of the sensor can be seen in Sec. 4.5.1.

3.5 Summary

Our principal contribution in this thesis is to match the high fidelity of stand-alone force and tactile sensors with the use of a single, integrated sensor. Since a force sensor cannot measure tactile information, and a tactile sensor cannot accurately measure force information, we require both modalities to co-exist within the same sensing unit. At the same time, premising data acquisition on a single optical transducer (i.e. monocular camera) shared across the two modalities affords us a high level of integration. Our use of a unitary shared transducer equates to a reduced

hardware footprint for the same proximate data throughput and thereby to increased resource efficiency. Economizing on hardware resources has the ancillary benefit of increased portability of the sensor, such that it can more easily and readily be mounted onto an end effector for instance. We employ an elastic structure (coupled to visible markers) beneath an elastomer layer for force sensing, whereby multi-axis force/torque components are measured through the corresponding motion and area changes of each marker. The elastomer, meanwhile, conveys tactile information (pressure or geometry).

Chapter 4

Sensor Design, Prototyping and Analysis

4.1 Introduction

This chapter describes several tactile and force sensor prototypes that are based on the sensing architecture proposed in Chapter 3. All of the proposed sensors in this chapter are following the concept of integrating both tactile sensing and force sensing capabilities within one sensor housing with the use of a combination of an elastomer layer and an elastic structure above a camera.

This chapter firstly introduces the ICFTS with finite element analysis (FEA) in Sec. 4.2. Then an optical-based tactile sensor the CTS using reflective elastomer layer and cantilever structure is introduced in Sec. 4.3. The proposed sensor can detect both single-point touch and multi-points touch. Based on this tactile sensor, a tactile and force sensor the CFTS1 following the same architecture (a reflective elastomer layer plus a cantilever structure) is introduced in Sec. 4.4, where the sensor can detect both tactile information (in the form of pressure distribution) and force information. However, an issue with this sensor prototype is that the tactile sensing area and the force sensing area of the sensor are separate from each other, which does not entirely meet our needs. Thus, another tactile and force sensor the F-TOUCH0 using a new struc-

ture is proposed in Sec. 4.5, where a coated transparent elastomer layer and a spring-mechanism structure are applied above a camera. This sensor prototype shares the same sensing area for both tactile sensing (in the form of geometry information) and force sensing. A minimized version of the sensor prototype the F-TOUCH is then introduced. The prototype is designed to fit the size with a standard robot gripper and can measure both geometry information and multi-axis force/torque information.

4.2 ICFTS — Initial Camera-based Force/Tactile Sensor

4.2.1 Introduction

Tactile perception became an important aspect of robot design as it could convey useful information about the interaction of the body with the external environment (i.e. detection of mechanical stimulation and temperature) [113]. Human beings have an extremely powerful perception system that detects various tactile stimuli. The hand is one of the most dexterous parts of the human body using the tactile feedback from the fingers, humans can interact with the environment and perform dexterous manipulations. The same principle applies for robot design; a robotic hand could perform advanced manipulations if feedback from the tactile sensor was available [167]. However, tactile sensing in robots is relatively backward compared to that of humans [82]. Tactile sensors are single-functional with fewer degrees of freedom compared to the human hand [89].

Tactile sensors have attracted much attention from researchers in the past few years. Yousef [175] gives an overall review of tactile sensing for human-like manipulation in robotics. One of crucial tasks of tactile sensors is to acquire information from the contact surface, especially when this surface is curved or irregular. Greater contact area with the surface provides a more stable grasp and recognizing the different physical properties of contact material (i.e. surface texture and hardness) makes for an efficient manipulation [83].

Among all categories of recent tactile sensors, the optical-based sensor shows admirable compliance due to its soft structure employing elastomers. Compared to the conventional elec-

tromagnetic sensing methods, such as resistive or capacitive-based sensors that largely depend on the transmission of electrical signals, the optical tactile sensor has a high-resolution camera that can capture the geometry of the contact surface, as well as being able to measure the contact force. Thus, it can recognize multi-modal information of the physical properties of the contact object.

We propose a design of an optical-based force and tactile sensor ICFTS. The proposed sensor can obtain and measure a wide-range of force information with the use of a combination of an elastomer and a force-sensitive structure. At the same time, it can obtain the tactile information by using a camera to capture the pattern of the contact surface via a transparent silicone.

4.2.2 Sensor Design

We are introducing a new miniature sensor that is comparable to the size of a human finger. The proposed force and tactile sensor consists of the following parts: an elastomer part, a force-sensitive structure, LED arrays and a CCD camera.

The touch medium of the device is the elastomer part together with the flexure (a force-sensitive structure). The elastomer part is composed of two elastomers coated with a hollow membrane on top. The flexure has a three degree of freedom with a three cantilever structure, and its rigid structure can effectively stabilize the soft elastomer part. Both the elastomer part and flexure are placed on a hard surface which is a transparent acrylic sheet. The elastomer part is illuminated with white light through the LED arrays placed inside the device. In addition, LED arrays are used to provide an optimal condition for image capture. 3D-printed covers outside of the device are used to block the external light and preventing it from disrupting the light conditions of the interior. The camera captures deformations of the entire elastomer component to measure the applied force based on the deformation of eight individual legs circularly allocated on the bottom side of the outside elastomer and the tactile information based on the pattern presented by the transparent inner elastomer. The inner area gives high-resolution sensing with a spatial resolution of 2 microns.

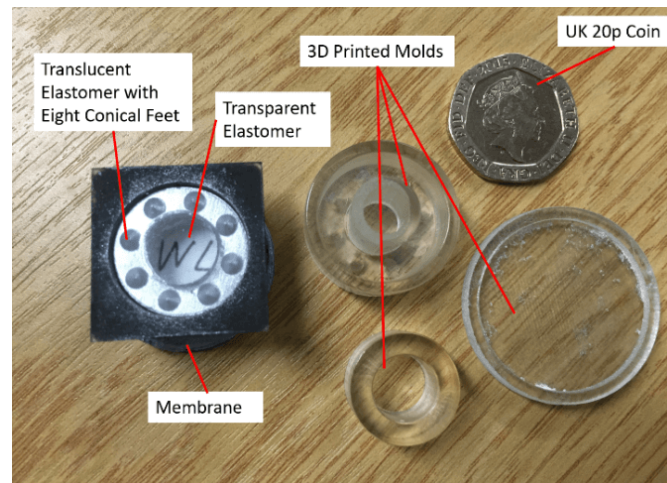


Figure 4.1: Manufactured elastomer part and the corresponding moulds.

Elastomer Part

The elastomer part consists of three parts: two elastomers and one membrane, as it is shown in Fig. 4.1. The inner elastomer comprises a long transparent cylinder that traverses both the membrane and the outside elastomer. The outside elastomer is a translucent hollow cylinder with eight miniature conical legs symmetrically attached at the bottom side of the cylinder. A hollow membrane is attached to the top of the cylinder. The three components are merged together so they can be treated as an integrated part, or named as the elastomer part. Since the elastomer part is soft and compliant, it produces good deformation when an external load is applied.

The properties of the elastomer play an important role in the tactile sensor and can largely affect the sensing range. An ideal elastomer material should be of low viscosity and good elasticity. Thickness and hardness are two important properties for the sensor design. A thick elastomer can carry out a larger degree of deformation. In our sensor, the inner transparent cylinder elastomer is made of Solaris® from Smooth-On Inc. To make the inner part, Solaris® part A and part B need to be degassed in the vacuum chamber before mixing, then both parts were mixed with a ratio of 1:1. Further on, the mixture is placed into the vacuum chamber again

for degassing since the stirring process might generate some bubbles, which are detrimental to the elastomer performance. Then we pour the silicone mixture into the 3D printed mould and leave the silicone to cure for 24 hours at room temperature. No additive liquid is needed during the mixing of part A and B since the softness of Solaris® has already met our needs. The hollow elastomer with eight conical legs is made from silicone (Ecoflex® 00-50 from Smooth-On Inc). The steps to make this translucent elastomer are similar but Ecoflex® 00-50 takes less time to cure (three hours). No additive liquid is required either. Moreover, we brush silver powder all over the surface of the hollow translucent elastomer, as well as the eight conical feet on the bottom side in order to increase the reflection of the elastomer itself, which leads to a better capture. The hollow membrane is made of dyed silicone (Eco-flex® 00-50 with Silc Pig® pigments). We need to premix the Silc Pig® in the container before dispensing and then add the colourant to Ecoflex® 00-50 part A, mix well before adding part B and wait for it to cure. Fig. 4.1 shows the transparent elastomer, translucent elastomer with eight conical legs and the membrane with some 3D printed moulds.

Force Sensitive Structure

The force-sensitive cantilever structure is used to encircle the elastomer part to stabilize and enhance the robustness of measurements. This flexure structure has three degrees of freedom.

The force-sensitive structure (flexure) consists of a hollow monolithic cylinder with three thin symmetrical horizontal cantilevers (with a thickness of 2.3 mm) in a circular arrangement. The external and internal diameters of the flexure are 25 and 20.2 mm, respectively. Each cantilever is linked to the rest of the flexure with short supports which allows the displacement to be formed either upwards or downwards between the slots (with a height of 0.78 mm of each cantilever). The tolerance of the flexure is thus 0.78 mm. Forces applying on the top of the flexure give a direct impact on the horizontal cantilevers and cause the deflection of the slots, while the bottom of the flexure remains fixed. The cantilever design ensures the minimal coupling effects between axial and lateral force components. Thus, the cantilevers bend only along the vertical axis when axial loading is applied and twist and bend along the vertical and horizontal

axes when a lateral load is applied.

The combined force-sensitive structure, together with the elastomer part, is shown in Fig. 4.2. During the contact, the deflection of the cantilever structure in the flexure results in the deformation and horizontal displacement of eight conical legs in the elastomer part. The deformation of the cantilever structure is analyzed during finite element simulations.

Based on the CAD design shown in Fig. 4.2, we use a 3D printer Stratasys Objet30 Prime to print this flexure with a polymer material (VeroClear-RGD810) that has high robustness and low hysteresis. Since the device should be isolated from the external light source, we sprayed the printed transparent flexure with black dye paint. The mechanical properties of the polymer are summarized in Tab. 4.1. One feature is that the material has a heat deflection temperature (HDT) of over 45 °C, which ensures that minimum deflection will occur in terms of the contact under human body temperature or room temperature.

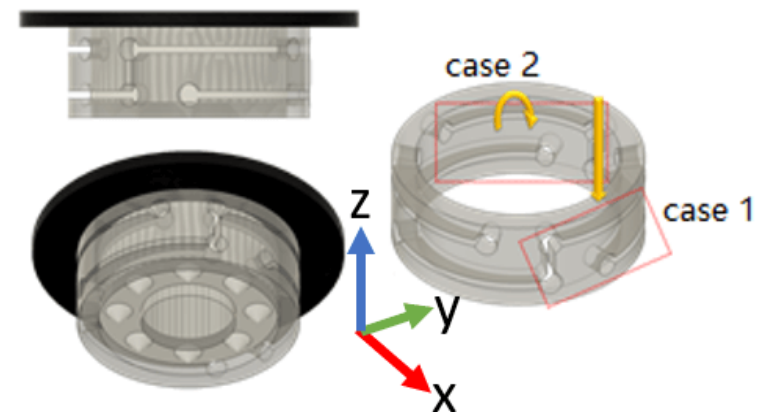


Figure 4.2: CAD design of the force-sensitive structure (two red square areas represent case 1 and case 2). In case 1, the flexure is designed to deform only along the vertical axis when axial loading is applied (show one of the three symmetrical cantilever structure). In case 2, the flexure is designed to twist and bend along the vertical and horizontal axes when a lateral loading is applied (show one of the three symmetrical cantilever structure).

Table 4.1: Force Sensitive Structure Material Properties

Property	RGD810
Tensile Strength	50 - 65 MPa
Elongation at Break	10% - 25%
Flexural Strength	75 – 110 MPa
Flexural Modulus	2,200 – 3,200 MPa
HDT, °C at 0.45MPa	45 – 50 °C
Shore Hardness (D)	83-86 D
Polymerized Density	1.18 – 1.19 g/cm ³
Poisson's Ratio	0.38

Illumination and Image Capture

A key aspect of the sensor is the way the elastomer part is illuminated. A white LED array is placed on the base of the housing for sensor illumination. The light from each of the LEDs travels through the light-guiding plates which have a 45-degree angle on one end to guide and reflect the light to the supporting plate and thus illuminate the elastomer part. The LEDs are of size 3 mm with 30-degrees viewing angle, soldered on a 3D printed electronic housing made of VeroClear-RGD810. Transparent acrylics with 1/8-inch thickness are cut as the light-guiding plates and supporting plate, using the laser cutter PLS6.150D.

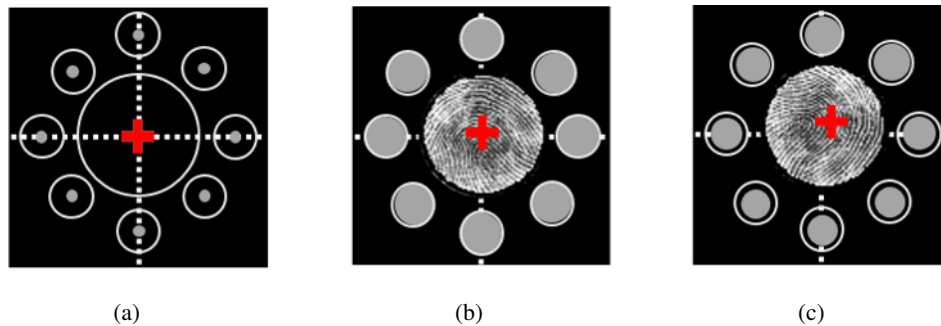


Figure 4.3: The corresponding response of the sensor when normal force and lateral moment are applied. (a) The original status of the captured elastomer part when no load is applied; (b) the captured elastomer part when a normal force is applied; (c) the captured elastomer part when both a normal force and a lateral moment are applied.

A CCD camera is placed at the bottom of the sensor to capture the deformations of both the transparent elastomer and eight feelers when contacting an external surface. The camera needs to be small, as well as having the white balance and automatic light correction. The USB webcam Logitech c270 satisfies all the requirements and has an HD 720p widescreen with noise reduction. Besides, a mobile phone camera or a small Raspberry Pie camera might perform better.

To give a better understanding of the working principle of the tactile sensor, a thumb is placed on the top of the surface. The deformations of the elastomer part can be segmented as two sections, one is in the centre area and the other one is the outer area. Initially, when there is no contact between the sensor and the thumb, the centre area shows the natural environment scene (assuming the default environment is black), see Fig. 4.3(a). Then we apply a normal force with our thumb, and the camera can capture an image shown in Fig. 4.3(b). The pattern image (the fingerprint) is shown in the central area, of which the surface geometry can be clearly recorded. The deformations of eight conical feet are recorded at the outer area, where the shape of each conical feet and horizontal displacement (it reaches the maximum normal force and there is no horizontal displacement for the normal force in this case) can be processed to evaluate the corresponding normal force. Finally, when we apply both a normal force and a lateral moment, the camera can capture an image shown in Fig. 4.3(c).

4.2.3 Sensor Prototype Evaluation

Finite element analysis (FEA) is a numerical method to investigate the performance of the target, make sure the target works within the expected range and optimize the design of the target before manufacturing [111]. In our design, we apply the Fusion360 in-built Static Stress FEA functionalities to investigate the behaviour of the force-sensitive structure, using the material VeroClear-RGD810 (the material property is in Tab. 4.1). According to [110], we aim to design a flexure structure that can measure a maximum force of up to 20 N (equals to 200 gm). The amount of deformation under vertical and lateral loading is shown in Fig. 4.4, The simulation result in Fig. 4.5 shows the sensitive force structure measures the maximum normal force of 20 N

and the maximum lateral torque (around the x-axis and y-axis) of 87.5 N/mm . The parameters of the flexure are given in the force-sensitive structure in sensor design. Besides, the sensor also provides a force overloading protection which means if the load is too heavy for the flexure to

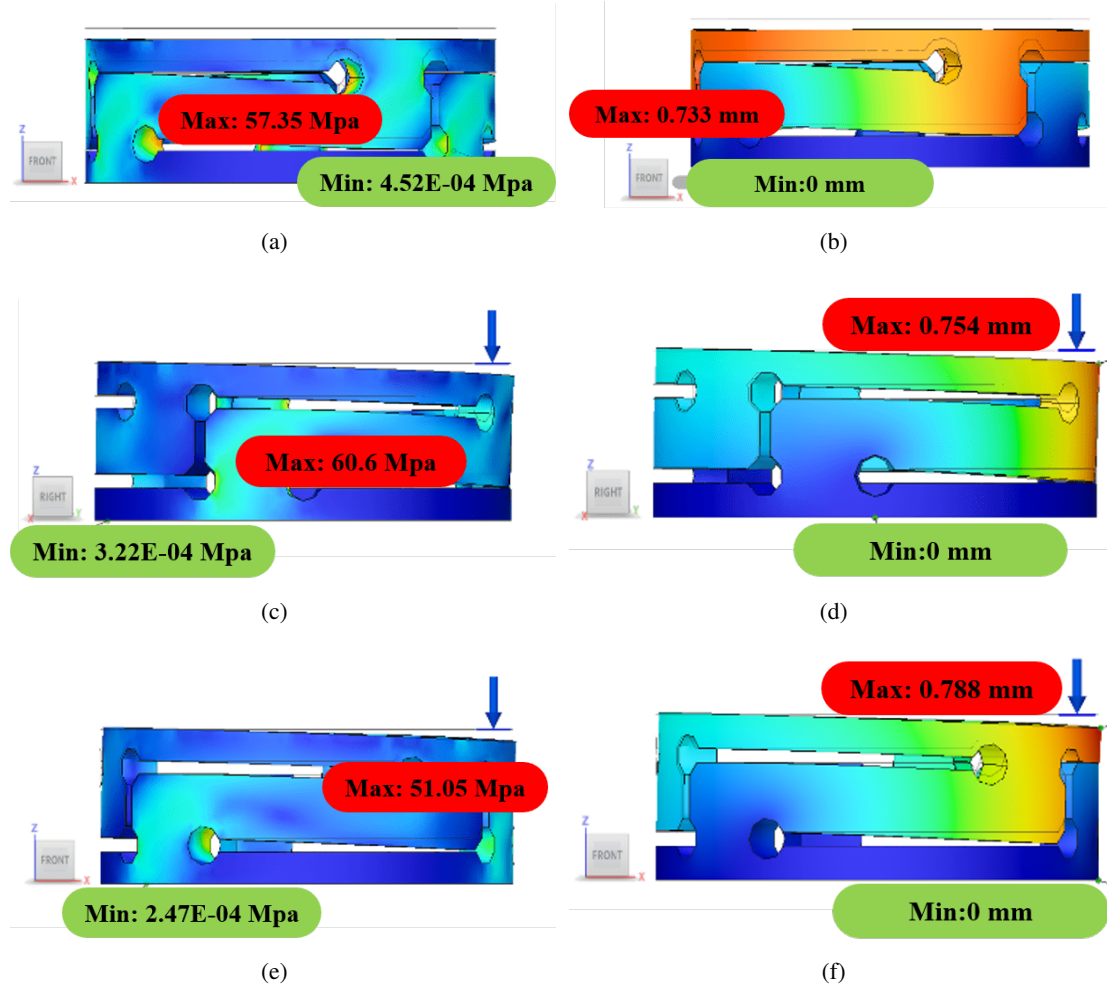


Figure 4.4: Finite element analysis (FEA) simulation performed with Fusion 360 Simulation Tool, showing the mechanical behaviour under normal force and lateral moment of the force sensitive structure. (a) Stress behaviour under normal force $F_z = -20 \text{ N}$. (b) Displacement behaviour under normal force $F_z = -20 \text{ N}$. (c) Stress behaviour under normal force $F_z = -7 \text{ N}$ and $M_x = -87.5 \text{ N/mm}$. (d) Displacement behaviour under normal force $F_z = -7 \text{ N}$ and $M_x = -87.5 \text{ N/mm}$. (e) Stress behaviour under normal force $F_z = -7 \text{ N}$ and $M_y = 87.5 \text{ N/mm}$. (f) Displacement behaviour under normal force $F_z = -7 \text{ N}$ and $M_y = 87.5 \text{ N/mm}$.

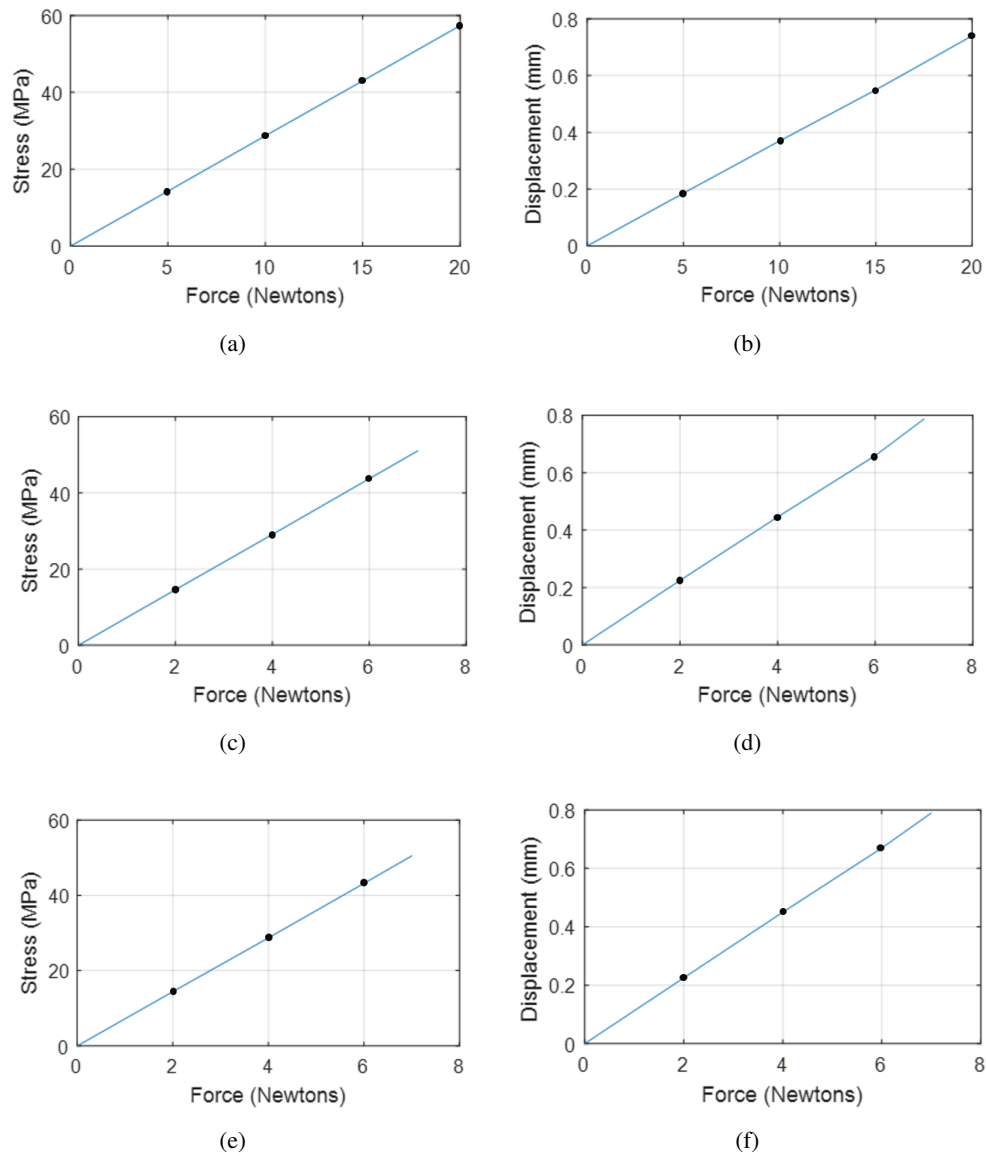


Figure 4.5: Von Mises stress and displacement of the force-sensitive structure using finite element analysis (FEA). Stress against force components in (a) normal force F_z ; (c) normal force F_z and lateral moment M_x ; (d) normal force F_z and lateral moment M_y . Displacement against force components in (b) normal force F_z ; (d) normal force F_z and lateral moment M_x ; (f) normal force F_z and lateral moment M_y .

sustain, the cantilevers will bend and physically contact with the solid part of the cylinder. Thus, the flexure can sustain a maximum of around 25 N before damage occurs.

Then we apply the finite element analysis (FEA) to investigate the behaviour of the elastomer part. The parameters of the elastomer part are based on the parameters of the flexure structure to ensure the size and the extent of deformation of both are matched. The material used for FEA is Ecoflex® 00-50 and Solaris®. The material properties of Ecoflex® 00-50 are a density of $1.07e-06\text{ kg/mm}^3$, Young's modulus of 0.08 MPa , a tensile strength of 2.2 MPa . The material properties of Solaris® are a density of $0.99e-06\text{ kg/mm}^3$, Young's modulus of 0.1 MPa , a tensile strength of 1.2 MPa . These values are based on information shown by Ecoflex® Series - Smooth-On Inc. and Solaris® - Smooth-On Inc. Simulation result in Fig. 4.6 shows the elastomer part measures the maximum normal force of 1.5 N and the maximum lateral torque (around the x-axis and y-axis) of 3 N/mm . The amount of deformation of the elastomer part shows a linear relationship with vertical and lateral loading, and the strain at the contact area of each conical leg also demonstrates a linear relationship with vertical loading, as is shown in Fig. 4.7.

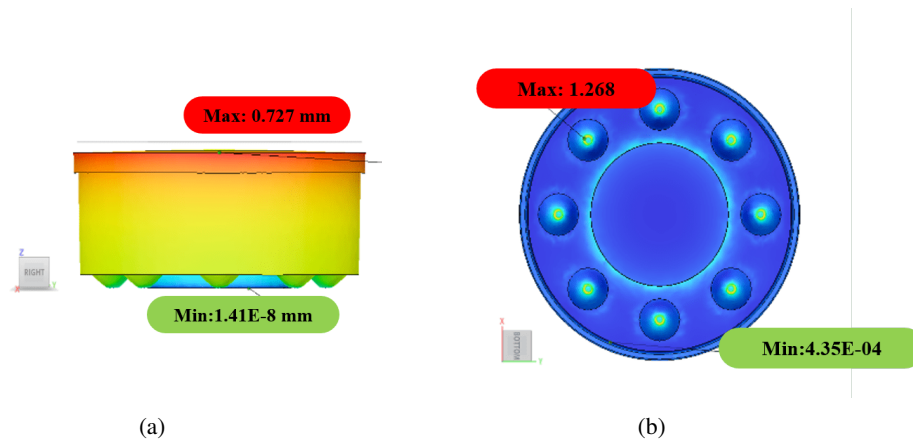


Figure 4.6: Finite element analysis (FEA) simulation performed with Fusion 360 Simulation Tool, showing the mechanical behaviour of the elastomer under normal force without lateral moment. (a) displacement behaviour under normal force $F_z = -1.5\text{ N}$. (b) bottom view of the strain behaviour of the elastomer under normal force $F_z = -1.5\text{ N}$.

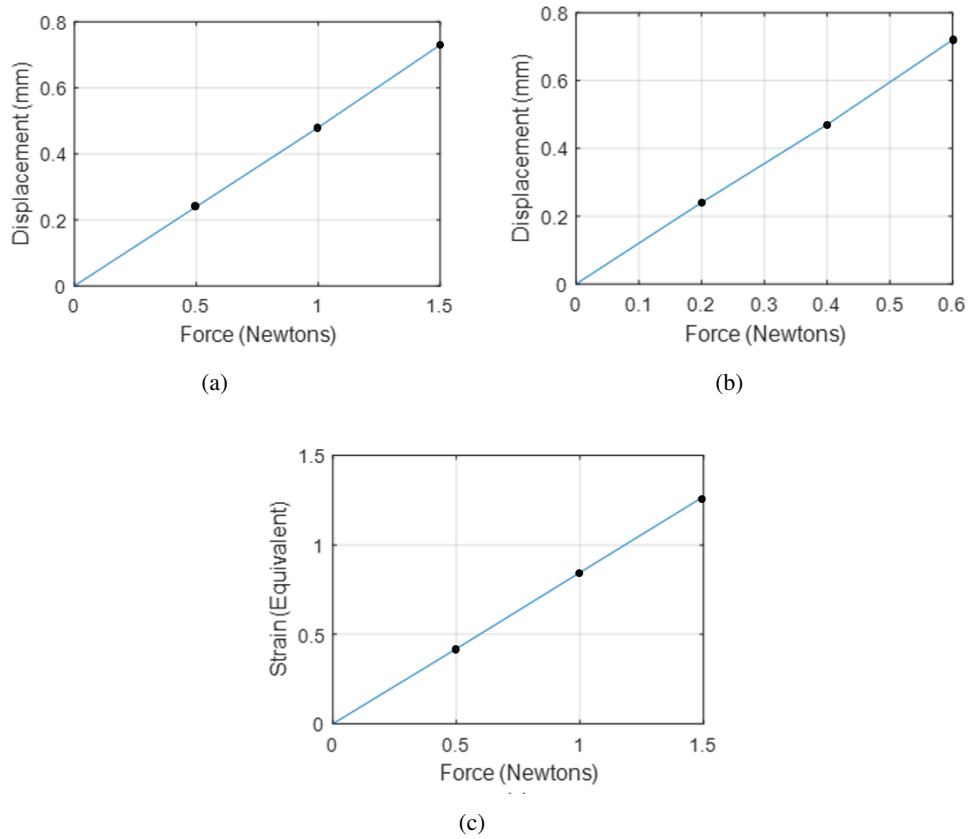


Figure 4.7: Displacement of the elastomer part and equivalent strain at the contact area of the conical leg tip using finite element analysis (FEA). Displacement against force components in (a) normal force F_z , (b) normal force F_z and lateral moment M_y . Stress against force in (c) normal force F_z .

Finally, we apply the finite element analysis (FEA) to investigate the behaviour of the combination of both force-sensitive structure and the elastomer part, based on the material used above. The simulation results in Fig. 4.8 show that the flexure can be assembled with the elastomer part and largely expand the sensor's measuring range with the maximum normal force of 22.5 N and the maximum lateral torque (along the x-axis and y-axis) of 95 N/mm . The displacements of both flexure and the elastomer part are linear against force components, and the strain at the tip of the elastomer's conical leg is also proportional to the applied force. Thus, we can establish a

map between the deformations of the conical legs and the external force.

We have created a user interface for the tactile sensor in MATLAB, as is shown in Fig. 4.9. The top left is the live video of the webcam. There are two spaces in the bottom left part, the left one is the capture of the present image, and the right one is the calibration image. In the right part of the interface, we segment the captured image into nine parts (8 images of conical legs Pin 1 to Pin 8, and the centre is for the tactile information). When no load is applied to the sensor, the camera captures an image as the calibration image. The sensor can detect three force

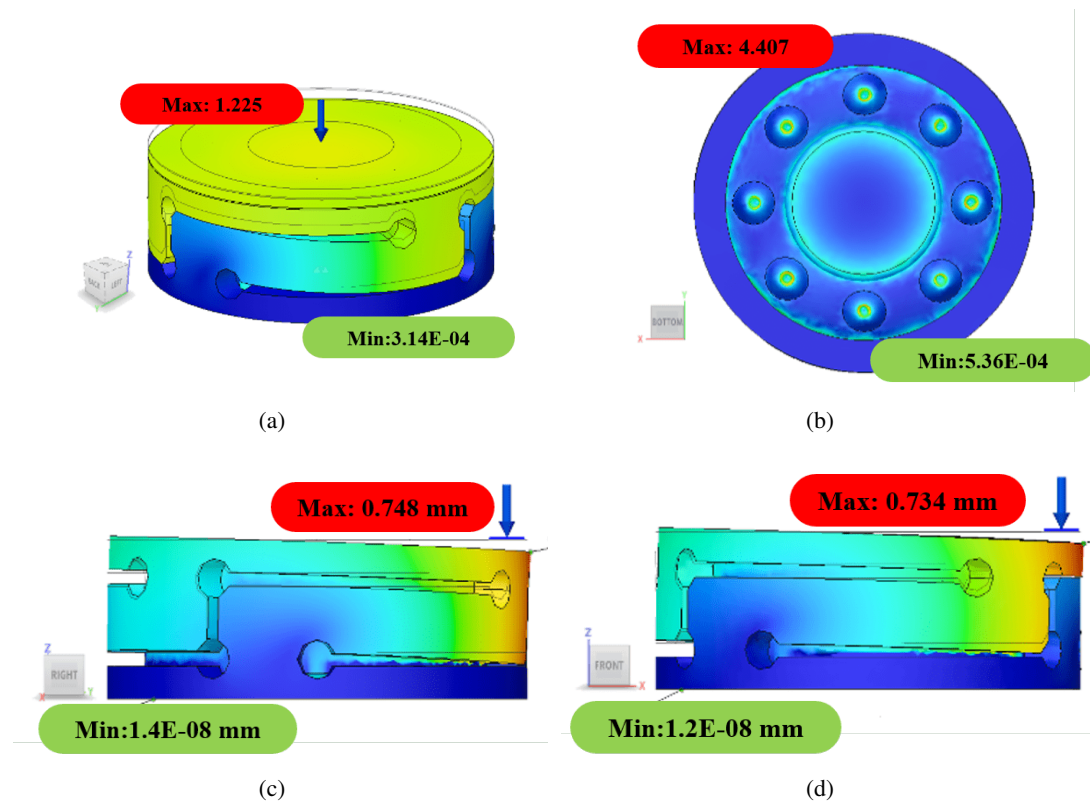


Figure 4.8: Finite element analysis (FEA) simulation performed with Fusion 360 Simulation Tool, showing the mechanical behaviour under normal force and lateral moment of the combination of the force-sensitive structure and the elastomer part. (a) Bottom view of the strain behaviour of the elastomer under normal force $F_z = -22.5 \text{ N}$. (b) Strain behaviour under normal force $F_z = -22.5 \text{ N}$. (c) Displacement behaviour under normal force $F_z = -7.6 \text{ N}$ and lateral moment $M_x = -95 \text{ N/mm}$. (d) Displacement behaviour under normal force $F_z = -7.6 \text{ N}$ and lateral moment $M_y = 95 \text{ N/mm}$.

components F_z , M_x and M_y . In normal load testing, a normal force is applied by directly adding different weights (from 10 *grams* to 100 *grams* with a step of 10 *grams* and from 100 *grams* to 1000 *grams* with a step of 100 *grams*) on the centre of the tactile sensor's membrane along the z -axis. We capture each weight's image in the sequence and save them in a database. In lateral load testing, the sensor is fixed and a string is stretched along the x -axis and y -axis, respectively. One end of the string is connected to the transparent elastomer in the centre, and the other end is connected to the loads hanging along the corresponding axis. Lateral loads with different weights (from 10 *grams* to 100 *grams*) are connected with the string, and the weights' images along x -axis and y -axis are captured in sequence, respectively.

During the test, we apply different objects on top of the sensor elastomer and the sensor's camera can capture the image as shown in Fig. 4.9, where both the force information (the status of the eight conical pins) and tactile information (the initial of a signature) can be observed

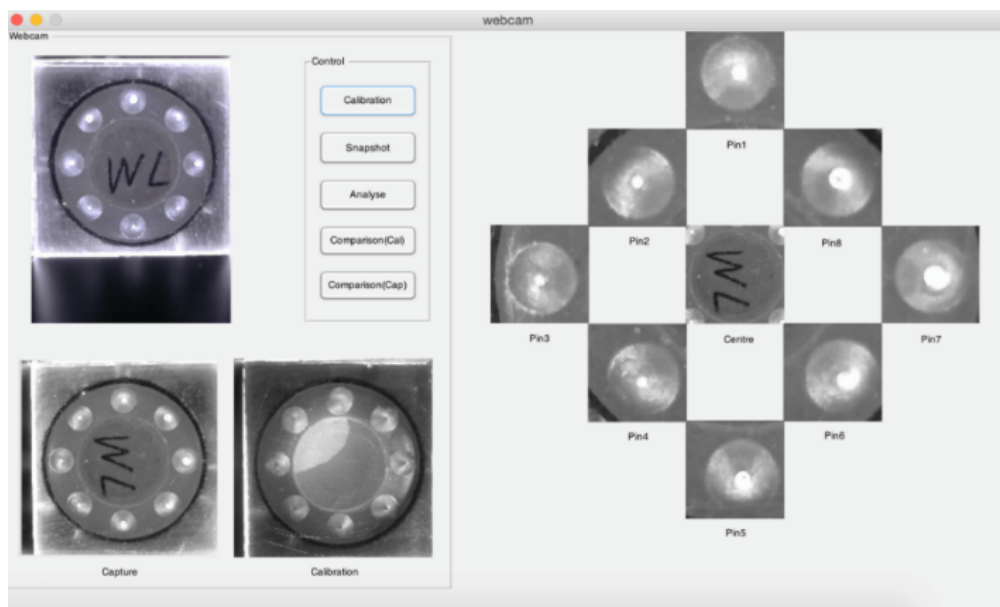


Figure 4.9: User Interface of the sensor. Top left is the live capture; the right area shows the status of the eight force pins (for force/torque measurement) and the central transparent elastomer (for geometry observation). Bottom left shows the capture when an object (with an initial of a signature on its surface) is pressed against the sensor's elastomer surface.

during the sensing in real-time.

4.2.4 Summary

In this work, we have introduced the hardware design of the ICFTS that can sense both force information and tactile information with the use of a combination of a force-sensitive structure (flexure) and an elastomer part. Finite element analysis (FEA) has been conducted to simulate the sensor's behaviour under different loading conditions. Simulation results verify that the combination of the force-sensitive structure and the elastomer part within the sensor can largely increase its force measuring range comparing with using an elastomer part only. The force information can be evaluated from the status of the eight force pins surrounded at the elastomer's bottom surface, and tactile information (geometry) can be obtained via the central transparent area. We have also proposed a method for the sensor's force calibration with the use of weights and strings. However, this is only a prototype sensor, and we have later realised the image processing of the current eight force elements can be challenging due to the low contrast between the bottom side of the pin and the background, as well as the overall hardware layout (the way of the physical combination between the flexure and the elastomer part did not perform well when measuring force and tactile information). Thus, we abandoned the work of this sensor, and we believe a more desirable design shall be proposed to give a better performance.

4.3 CTS — Camera-based Tactile Sensor

Due to the infeasibility of the ICFTS sensor described above, we aimed to find another combination of the elastic structure and the elastomer layer so that to implement our expected functionalities better. This section presents an optical-based tactile sensor CTS that can sense the tactile information in the form of pressure distribution. Our proposed sensor uses a piece of coated elastomer with thin conical pins underneath as the touch medium and a cantilever structure as the supporting medium. The elastomer consists of 91 pins arranged in a honeycomb pattern; each pin can be regarded as a tactile sensing element at 1.5 mm spacing. Each tactile element

transfers the applied pressure value into a circular image pattern which can be captured by a camera placed at the end of the sensor structure. The applied pressure over the sensing array can be computed via the processing of the area of each sensing element. MATLAB is used to process the received images that it relates the applied pressure to the activated pixels in each circular pattern of the tactile element, and further visualizing the pressure distribution on a reconstructed surface of the sensor. This work presents the development principle and fabrication process of the proposed sensor prototype. The experimental results have proven the viability of this new combination that the sensor prototype can effectively detect single-point touch and multi-points touch with a spacing of more than 2.5 mm.

4.3.1 Sensor Design

Optical tactile sensors have attracted plenty of attention from researchers in the past few years [139]. Compared with the electromagnetic sensing methods such as resistive-based or capacitive-based sensors that largely require the transmission of electrical signals, optical-based sensors simply use a high-resolution camera to capture all the information and transduce the deformation of the sensing surface with the aid of computer vision techniques. Moreover, most of the optical sensors use a physical medium which can deform according to the applied force and then indirectly infer the contact information from the deformation. This contact medium usually is a piece of elastic material or a specific deformable structure as the compliant structure refers to its ability to conform to curved or irregular surfaces of the objects during the manipulation tasks.

In this work, the proposed optical-based tactile sensor CTS (shown in Fig. 4.10(b)) which is a bio-inspired and low-cost device which uses a 3D printed shell (with elastic structure) and a compliant contact surface (so-called elastomer) as a touch medium to obtain tactile information. Fig. 4.11 demonstrates the schematic design of the sensor that is made of several components. The elastomer (1) is made of a silicone material extracted from a 3D printed mould to provide the compliant properties referred to as the touching medium of the sensor. The interior of the elastomer has a well-organized array of small reflective pins which are made of silicone mixed

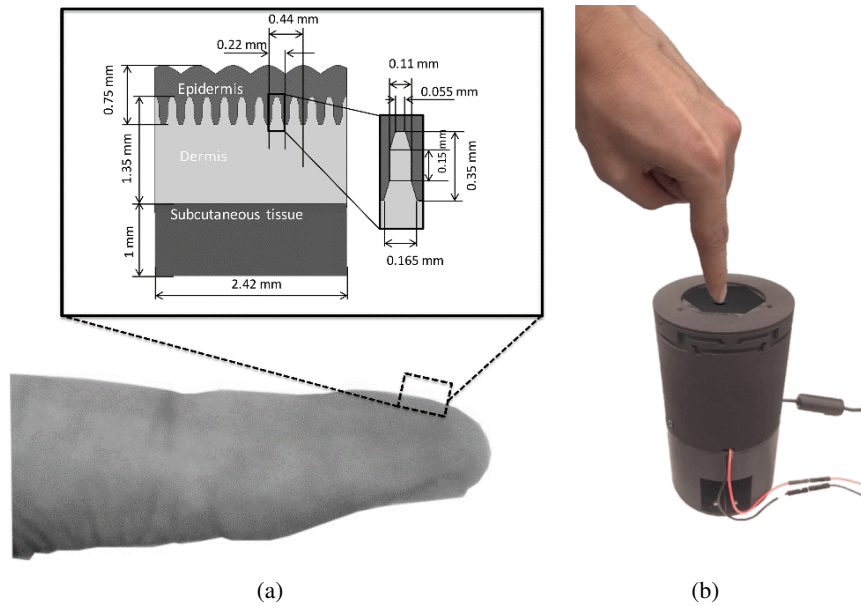


Figure 4.10: (a) A simplified elastic model that mimicks a cut-away view of the human fingertip [121]. (b) The proposed tactile sensor uses numerous tactile elements to mimic the epidermis of the skin. The sensor can be used to detect the pressure and create a 3D-surface reconstruction of the sensor membrane.

with metallic powder. A web-cam (2) is placed at the bottom of the device to capture the deformation of the elastomer. A transparent acrylic sheet with 5 mm thickness (3) is placed beneath the elastomer, known as the supporting plate to provide a solid supporting for the elastomer pins. A white LED array (4) is placed inside the 3D printed shell (5) acting as an internal light source to illuminate the elastomer; the light goes through the light-guiding plate (6) which has a 45-degree angle at the edge towards the pins of the elastomer. The 3D printed sensor base (7) and shell are made of nylon (dyed in black colour). The shell is also known as a force-sensitive structure (so-called flexure) which acts as an elastic structure due to its build-in cantilever beams. With such design, the flexure enables the supporting the elastomer during the contact. A top cap (8) is screwed at the top of the sensor to prevent the elastomer from falling during the interaction with the external environment.

Although the pins in the proposed sensor look similar to the TacTip sensor [167], the mea-

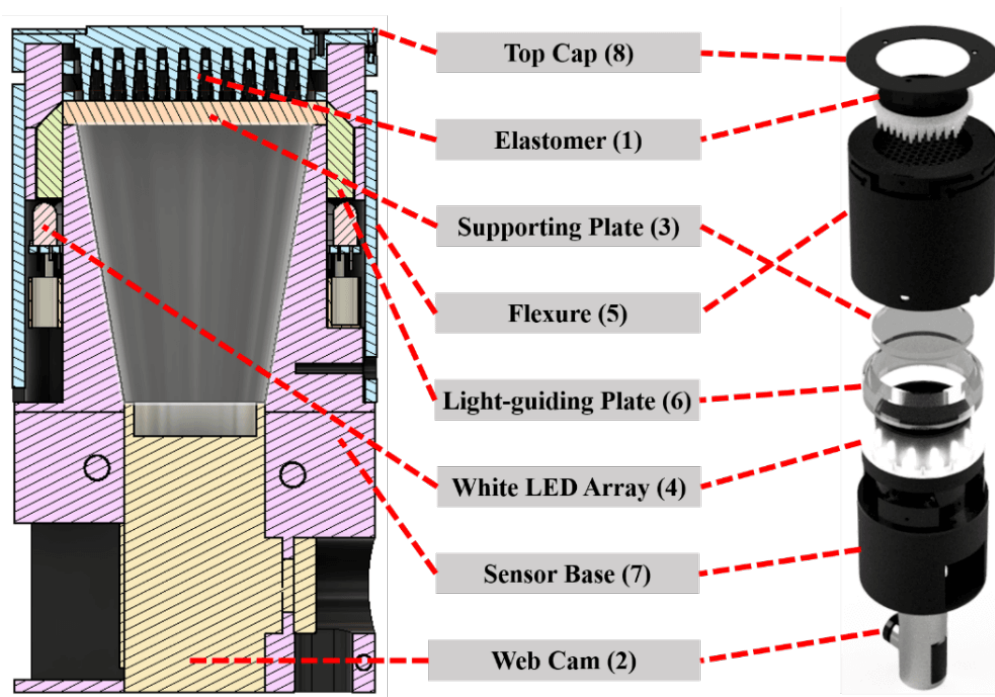


Figure 4.11: An optical-based tactile sensor design. Left is the schematic design and right is the exploded view of the sensor prototype. There are eight core components that make up the sensor.

surement principle of the tactile information is different. The TacTip sensor obtains tactile information from white circular markers on raised pins, and can measure the local shear forces. In our device, the pin deformation and the resultant diameter of the contact area with an acrylic supporting plate depend on the magnitude of the applied normal force. Therefore, we can measure the pressure signal and capture different irregular 3D shapes and patterns by observing the compression of the silicone pins. This sensor cannot measure shear forces.

The elastomer part acts as the touch medium of the device. It is composed of an array of pins on the interior of the soft silicone membrane to translate contact information into the pin deformation, which can be then presented as the visualization of the tactile data. The array of pins performs a similar mechanical response as the dermal papillae of the human skin (See Fig. 4.12).

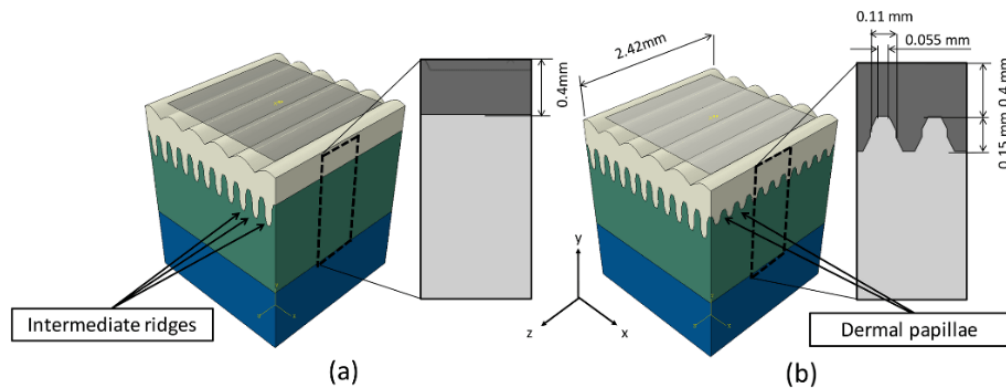


Figure 4.12: Depth configuration of (a) the 2D ridged model and (b) the 3D ridge model [121].

In our work, the elastomer part is composed of two parts: the opaque elastomer base with a hexagonal arrangement of 91 reflective pins underneath and the opaque membrane. The elastomer's properties largely influence the sensitivity of the device, so we have used elastic pins and a thin, flexible and uniform membrane. Fig. 4.13 shows the manufactured elastomer, including both the elastomer base and the membrane together with its 3D printed mould made of polylactic acid (PLA). The layout of the pins is a 2D hexagonal pattern with 91 elements, placed at 1.5 mm distance to each other. Each conical pin has a height of 11 mm, a diameter of 3 mm at the base and a diameter of 1.25 mm at its tip. These tactile pins are in contact with the transparent supporting plate, facing towards the camera when at the rest and pressed into deformation when a load is exerted at the membrane on the top. The deformation of these conical pins is captured by the camera at the sensor base and can be processed to measure the tactile information in the form of visualizing the spatial pressure distribution via applying computer vision techniques.

Fig. 4.14 demonstrates the fabrication process of the elastomer part. The two silicones used in the sensor are Dragon Skin 20 and Ecoflex 00-50 from Smooth-On Company. The properties of both silicones are shown in Tab. 4.2. The silicone is generally stored as two separate liquid parts, known as part A and part B with a ratio of 1:1. During the moulding of the elastomer base with pins, Silicone Thinner and part A of Dragon Skin 20 is pre-mixed with a weight ratio of 1:5. Silicone Thinner is a non-reactive silicone fluid that can lower the viscosity of platinum

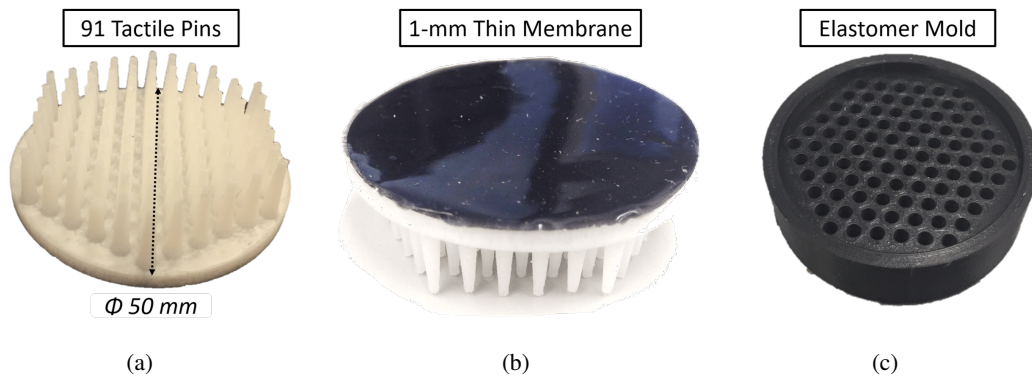


Figure 4.13: (a) View towards the bottom surface of the elastomer where 91 reflective tactile pins are attached at the surface. (b) View towards the top surface of the elastomer where a black opaque coating is mounted. (c) 3D printed mould that is used to produce the elastomer component.

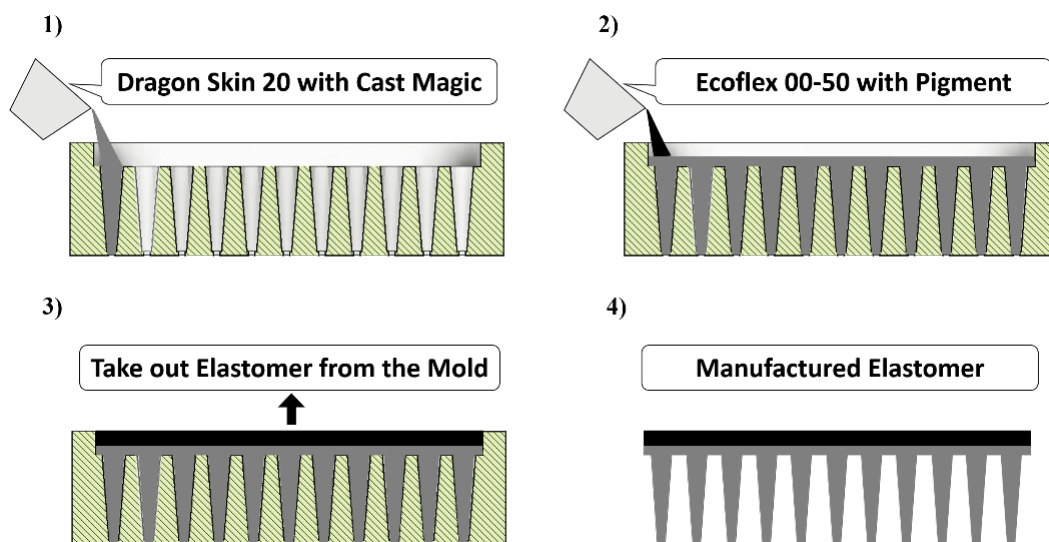


Figure 4.14: The fabrication process of the elastomer component. Firstly we pour the mixture of Dragon Skin 20 with Cast Magic into the pin slots within the mould. Then we pour the mixture of Ecoflex 00-50 with black pigment into the rest space of the mould. Finally, we take out the manufactured elastomer component.

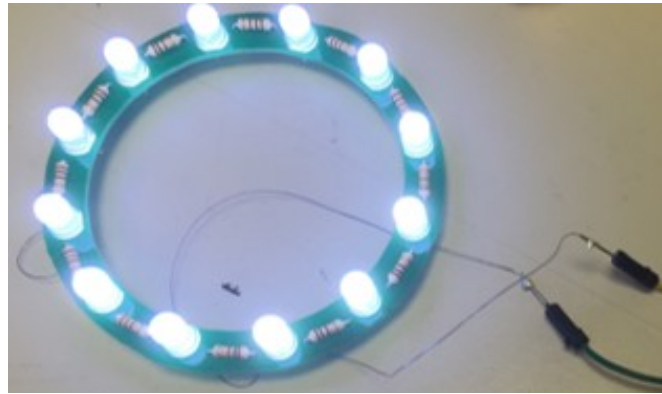
cure silicone (Dragon Skin 20 and Ecoflex 00-50 in this case), enabling the elastomer to de-air faster, and the liquid mixture to flow better over the intricate mould. Then, part B of Dragon

Skin 20 is added into the liquid mixture with the same weight as part A. Silver Bullet Cast Magic Powder is then added to the material with a weight ratio of 1:100 to make the material reflective on its surface. The liquid mixture is put into a planetary conditioning mixer (THINKY ARE-250) to mix and degas. We pour the material into the holes of the mould and wait for about four to five hours for the silicone to cure. For the membrane, the layer is required to be thin and opaque since thinness ensures the high resolution of the sensor, and opacity helps to exclude the light interference coming from the external environment. Silc Pig silicone colour pigment is used to colour the membrane black to avoid external light disturbance. As for the membrane manufacturing, Silc Pig black colourant is added to the part A of Ecoflex 00-50 and mixed well before adding part B. The liquid mixture is then sent to the mixer and poured on the top of the cured elastomer base. After 3 hours of curing time, the manufactured elastomer can be taken out of the mould.

Table 4.2: Elastomer Material Properties

Property	Dragon Skin 20	Ecoflex 00-50
Specific Gravity	1.08 g/cc	1.07 g/cc
Cure Time	4 hours	3 hours
Shore Hardness	20 A	00-50
Tensile Strength	550 psi	315 psi
100% Modulus	49 psi	12 psi
Elongation @ Break	620%	980%
Mix Ratio By Weight	1A:1B	1A:1B
Colour	Translucent	Translucent
Mixed Viscosity	20000 cps	8000 cps

As shown in Fig. 4.15(a), we use an LED array which contains 12 white 5 mm LEDs with 30-degrees viewing angle. All LEDs are soldered on a hollow-ring shaped printed circuit board (PCB) in parallel, and the LED array is placed inside of the sensor to generate an inner light source, powered by a USB TTL cable. In order to completely block the external light interference, an opaque silicone rubber ring made of Ecoflex 0050 (painted black) is placed on top of the light-guiding plate. The size of the hollowed rubber ring is 55 mm of inner diameter and 66 mm



(a) Fabricated LED array



(b) Manufactured opaque rubber ring

Figure 4.15: Core components within the proposed tactile sensor illumination system. (a) LED array for the internal light source. (b) An opaque rubber ring made of silicone to block the external light.

of outer diameter with a 45-degree angle at one end, which is the same as the light-guiding plate dimension. The light-guiding plate is a 3D printed (using transparent material VeroClear) hollowed cylinder with a 45-degree angle on the top end to guide and reflect the light from LED to the transparent supporting plate (shown in Fig. 4.15(b)), and therefore illuminate the reflective elastomer pins. The top cap of the sensor also helps to block the light coming from upwards. We use a webcam (Microsoft LifeCam Studio) with a resolution of 640×480 pixels and 30 fps to capture the visible area of the elastomer pins. Focusing on the centre area of 430×430 pixels cropped from the received raw image, tactile information can be processed and visualised in the

form of pressure distribution.

4.3.2 Working Principle of the Optical-based Tactile Sensor

A MATLAB model determines the activated area of each tactile sensing element (elastomer pins). As is shown in the flowchart of Fig. 4.16, we first read the real-time video information from the webcam. Next, the real-time RGB image is converted to a grey-scale image and is divided into 91 hexagonal parts based on a uniformly distributed honeycomb layout, which enables the detection of activated area for each sensing element. After that, the grey-scale image is further converted into a binary image, and a numeric display calculates the quantity of black and white pixels detected from each hexagonal area. Finally, via an interpolation method applied to the scattered data, we reconstruct a surface of the elastomer membrane based on the activated area of each silicone pin.

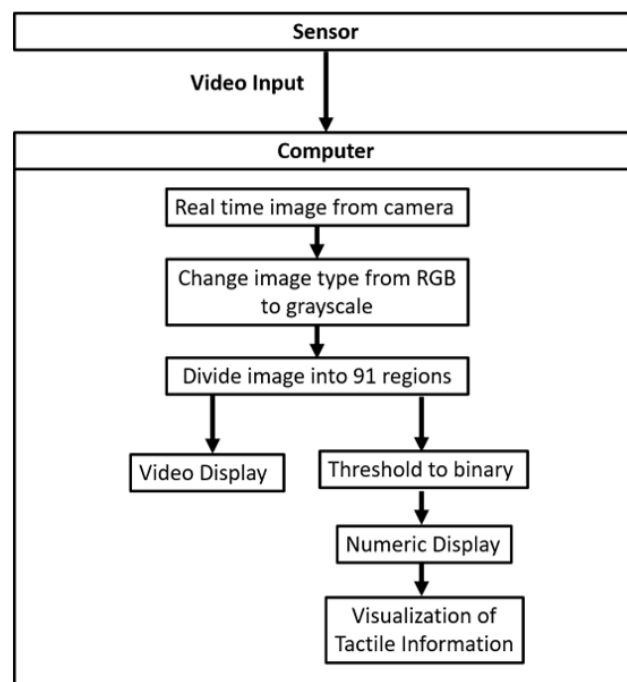


Figure 4.16: A flowchart that explains the process of generating the visualization of the pressure based on analyzing the activated pin areas from the elastomer component.

When switching on the power, the light is transferred from the source to the unloaded elastomer through the light-guiding plate and the supporting plate. The webcam captures the raw images of the illuminated elastomer. The raw unloaded received images are displayed by the video output of Fig. 4.17(a), then the input image is converted to a grey-scale image and is divided into 91 hexagonal parts (with a radius of 23 pixels), see Fig. 4.17(b). Each hexagon represents one sensing element, and all 91 elements can be treated as an array. After thresholding

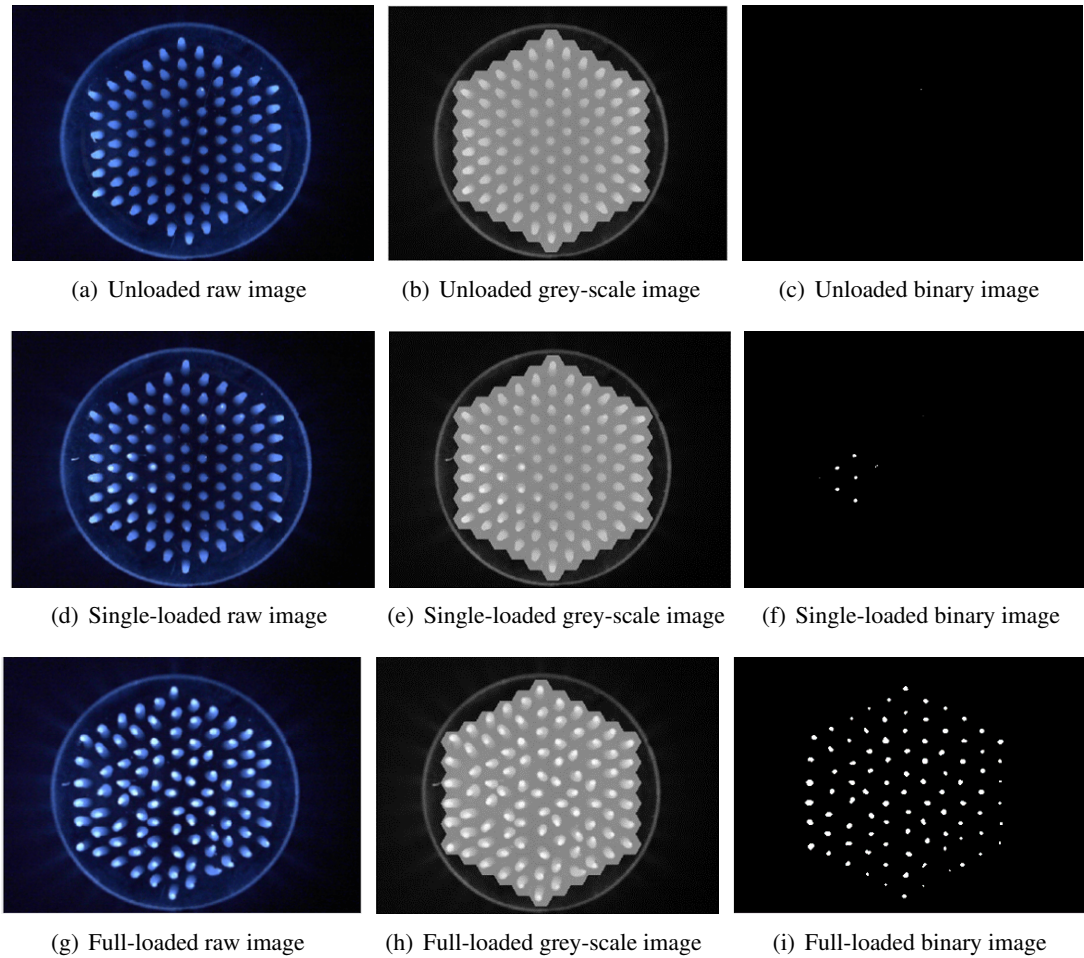


Figure 4.17: The proposed sensor's responses under different force exertion in the form of the raw image, the grey-scale image, and the binary image. Three scenarios are presented: the first row is the unloaded status; the second row is partially touched; the third row is fully touched.

(currently with a manually-set level value, but an adaptive thresholding could also work), the grey-scale image is converted into a binary image, as shown in Fig. 4.17(c), each size of the white blob represents the pressure magnitude (no more than 3 N) for its corresponding sensing element. Once an external contact is applied on the elastomer membrane, the pins are squeezed to the supporting plate, causing an increased contact area of each sensing element. Thus, the corresponding sensing area will receive more activated pixels. Fig. 4.17(d), Fig. 4.17(e), Fig. 4.17(f) show the raw image received by the camera and the corresponding grey-scale image and binary image when part of the membrane is touched. Fig. 4.17(g), Fig. 4.17(h), Fig. 4.17(i) show the raw image received by the camera and the corresponding grey-scale image and binary image when the whole surface of the membrane is touched.

The experimental results of the optical-based tactile sensor will be provided in the next chapter.

4.3.3 Summary

This work introduces an optical-based tactile sensing concept employing a 2D vision system for the acquisition of tactile information. The sensor uses a reflective soft opaque elastomer with 91 thin conical pins at one end made of silicone to obtain the spatial pressure distribution. The conical pins are placed in a 3D printed elastic structure and maintain contact with an inserted transparent acrylic plate. The pressure is detected from analyzing the binary values of bright pixels transduced from the contact area of 91 conical pins.

4.4 CFTS — Camera-based Force/Tactile Sensor

As the previous sensor has proven the proposed optical-method for tactile sensing, following the same sensor architecture, we further implement an optical-based force and tactile sensor (CFTS1) that can sense both modalities within one housing. In addition, the tactile information is measured in the form of pressure distribution from the surface of objects following the same principle as the previous sensor. The proposed sensor has a soft and compliant touching

medium employed with an opaque elastomer. An optical sensing method is used to measure both force and tactile information simultaneously based on the deformation of the reflective elastomer structure and the flexure structure. We will present the design and fabrication process of the sensor in the following subsections.



Figure 4.18: The design of the optical-based force and tactile sensor: (a) manufactured prototype, and (b) the exploded view of the sensor structure.

4.4.1 Sensor Design and Development

The overall design of the proposed optical-based force and tactile sensor CFTS1 is shown in Fig. 4.18. The proposed sensor is composed of the following main components. The soft and flexible elastomer structure (1) is a core part of the sensor used to measure normal force as well as tactile information in the form of spatial pressure distribution. The elastomer is positioned on the 3D printed part – which is the flexure in our design (2). The flexure is acting as a spring

mechanism due to an integrated cantilever structure (3) and is used for support and stabilization of the elastomer structure. In addition, it enables the required displacement for normal force measurements. A CCD camera (4) is used to capture the deformations of the elastomer, then converted to force and tactile information. In addition, a LED array (5) acts as an internal light source to sufficiently illuminate the elastomer via the light plate (6) for effective image capturing. The assembly of the sensor is completed with a top cap (7) to fix the elastomer, and a base part (8) to hold the structure together. The plastic components of the sensor are fabricated from acrylonitrile butadiene styrene (ABS) material using a 3D printer FDM360mc from Stratasys.

Elastomer Part

Soft, flexible elastomers are an important part of the sensor design. In our research, we use a special opaque and reflective elastomer material as the interface between the sensor and the environment to be measured. The elastomer structure is made of silicones of different types to distinguish between tactile and force information. Fig. 4.19 shows the produced elastomer structure together with its 3D-printed mould (Fig. 4.19(a)). Fig. 4.20 shows the fabrication process of the elastomer structure. The elastomer structure is composed of three parts, as it is

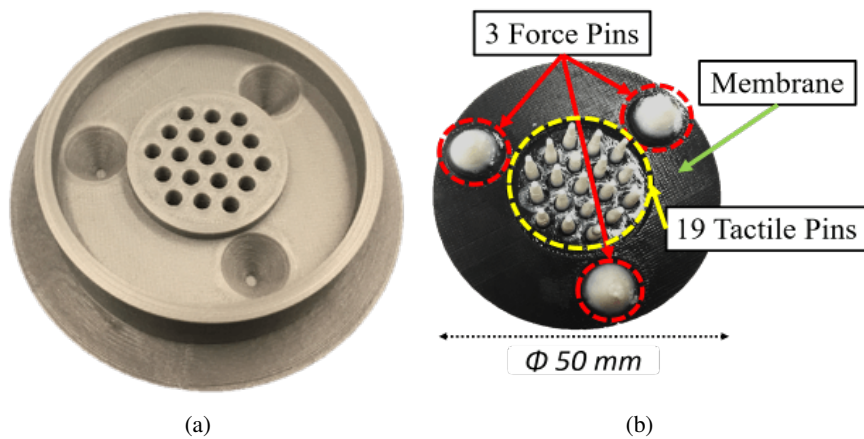


Figure 4.19: The design of the elastomer part: (a) 3D printed mould that is used to produce the elastomer component. (b) View towards the bottom surface of the elastomer where three reflective force pins and 19 reflective tactile pins are attached at the surface.

shown in Fig. 4.19(b). Force pins are used to measure normal force information; tactile pins measure tactile information in the form of spatial pressure distribution, and a membrane is used as the medium for interaction with the environment. The elastomer structure is positioned on a 5 mm thickness transparent supporting plate made from an acrylics sheet (shown in Fig. 4.21).

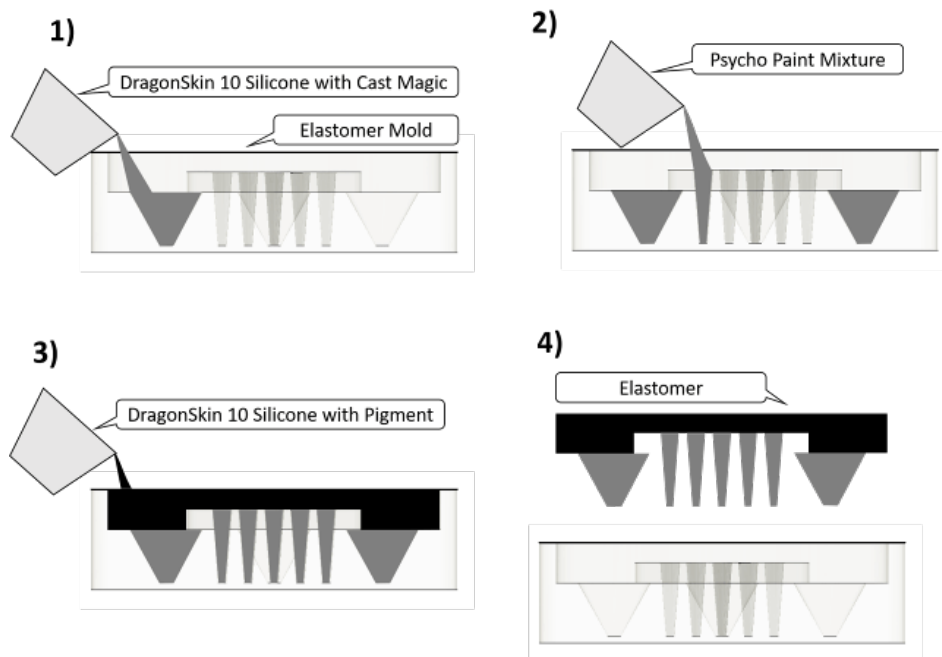


Figure 4.20: The fabrication process of the elastomer component. Firstly we pour the mixture of Dragon Skin 10 with Cast Magic into the three force pin slots within the mould. Then we pour the mixture of Psycho Paint into the tactile pin slots within the mould. Then we pour the mixture of Dragon Skin 10 with black pigment into the rest space of the mould. Finally, we take out the manufactured elastomer component.

Pins for normal force measurement: three grey reflective conical pins are used to measure the normal force. Each pin has a height of 8 mm, a diameter of 11 mm at the base, and a diameter of 2 mm at the tip. The smaller surface of the pins is in contact with the acrylic support plate when at rest. The pins deform and are pushed towards the plate when an external force is exerted onto the sensor. The deformation capturing principle is further explained in the next section.

We use silicone (Dragon Skin 10, Smooth-On, Inc.) with addition of reflective powder (Cast

Magic Silver Bullet, Smooth-On, Inc.) to fabricate the force pins (step 1 in Fig. 4.20). The reflective properties are required for efficient image capturing. The silicone material properties are shown in Tab. 4.3. The silicone is prepared and mixed with a powder with a weight ratio of 50:1. Further on, the mixture is put into a conditioning planetary mixer (THINKY ARE-250) for mixing and degassing. Then, we pour the resultant silicone mixture into the 3 conical holes of the mould. The curing process of force pins takes 5 hours.

Table 4.3: Elastomer Material Properties

Property	Dragon Skin 10	Psycho Paint
Mix Ratio By Volume	1A:1B	1A:1B
Elongation at Break	1,000%	1,000%
Colour	Translucent	Translucent
Shore Hardness	10 A	Not Given
Specific Gravity	1.07 g/cc	1.07 g/cc

Pins for tactile information: the tactile information is measured by 19 grey reflective conical pins - The resultant output is presented in the form of spatially distributed pressure information. Each conical pin has a height of 11 *mm*, a diameter of 3 *mm* at the base, and a diameter of 1.25 *mm* at its tip. The pins are arranged in a honeycomb pattern underneath the membrane. The 19 pins can be treated as a tactile sensing array with a spatial resolution of 5 *mm* \times 5 *mm*. All pins are in contact with the acrylic supporting plate at the rest status and will deform when an external object is in contact with the elastomer membrane.

We use platinum colour silicone (Psycho Paint, Smooth-On, Inc.) with the addition of reflective powder (Cast Magic Silver Bullet, Smooth-On, Inc.) to produce the tactile pins. The material properties of the used silicone are described in Tab. 4.3. The fabrication process is similar to the creation of the force pins, as is shown in step 2 in Fig. 4.20. Toluene (thinning agent) is added to the mixture to reduce the viscosity and to facilitate the pouring of silicone into the small holes of the mould.

Contact membrane: the membrane is a touch interface in contact with the external environment; its making is the final step in the manufacturing of the elastomer structure (as shown

in step 3 in Fig. 4.20). The membrane is fabricated from black silicone to block any interference from the external light. The silicone (Dragon Skin 10, Smooth-On, Inc.) is mixed with black pigment (Silc Pig Black, Smooth-On, Inc.) at a ratio of 100:1. The mixture is degassed and poured into the mould to cure for 5 hours, as is shown in step 3 of Fig. 4.20. Then, the manufactured elastomer part is ready (step 4 of Fig. 4.20).

Illumination and Image Capture

Another critical aspect of the sensing process is the way the elastomeric structure is illuminated. The illumination is implemented using an LED array and is required for good quality image capturing. The array contains 12 white LEDs with an outer diameter of 5 mm and 30-degrees viewing angle. As shown in Fig. 4.21, the LED array is positioned inside the structure of the sensor. To ensure light guidance towards the elastomer structure, the light-guiding plate was designed and 3D printed with Veroclear material. It is a hollow structure with a 45-degree edge at the top. The light travels through the light-guiding plate and is reflected from the top surface towards the centre of the sensor – i.e. towards the transparent acrylic supporting plate. Thus, the elastomer is illuminated, as shown in Fig. 4.21. A USB camera (Microsoft LifeCam Studio), with a resolution of 640×480 pixels and a frame rate of 15 fps, is placed inside the sensor to capture the visible area of the elastomeric structure.

Once the sensor is switched on, the light information is transferred from the light source to the unloaded sensing element (elastomer structure) and then to the camera. The raw images are received by the camera, Fig. 4.22(a). The input image is firstly converted to a grey-scale format. And then split into four regions – one for tactile pins (200×200 pixels), and one for each of the three force pins (80×80 pixels). To process tactile information, the tactile region is divided into 19 parts in a honeycomb pattern, each hexagon representing one sensing element. As a next step, the grey-scale image is converted into a binary image, as shown in Fig. 4.22(b). For visualization purposes, a numeric display is used to show the force magnitude value for each pin. The magnitude is calculated from the quantity of black and white pixels in each region for force measurement, and in each hexagon for the tactile information. Once a force is applied,

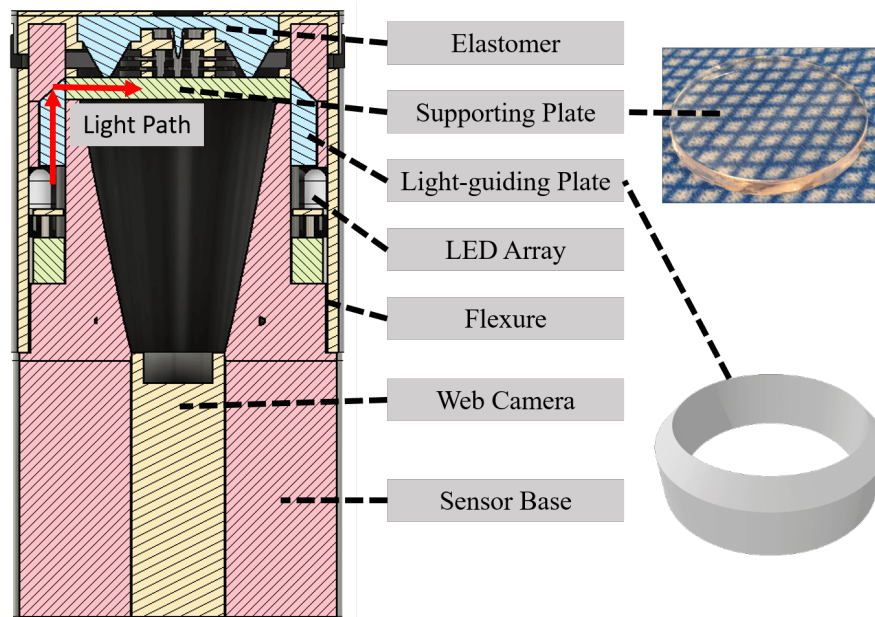


Figure 4.21: Proposed force and tactile sensor illumination system. The left side is the schematic design of the sensor. The right side shows the acrylic supporting plate and the CAD view of the light-guiding plate.

the pins are pushed towards the supporting plate and the pin contact area increases. Hence, the corresponding sensing area receives more activated pixels in the camera image, as are shown in Fig. 4.22(c) and Fig. 4.22(d). This sensing approach is a straightforward way to visualise how applied pressure and its distribution changes. The relationship between the number of activated pixels and applied force can be used to calibrate the sensor and measure force and tactile information. A mathematical model defines the change of contact area for both tactile and force pins. Additionally, we visualise the distribution of tactile information using a grey-scale pressure colourmap on a user interface. More experimental results will be presented in the next chapter.

We have developed another sensor prototype CFTS2 that shares the same sensing principle but some changes have been made to the elastomer part (as shown in sensor 2 of Fig. 4.23). In this sensor, the central area of the elastomer part is replaced with a transparent silicone (the

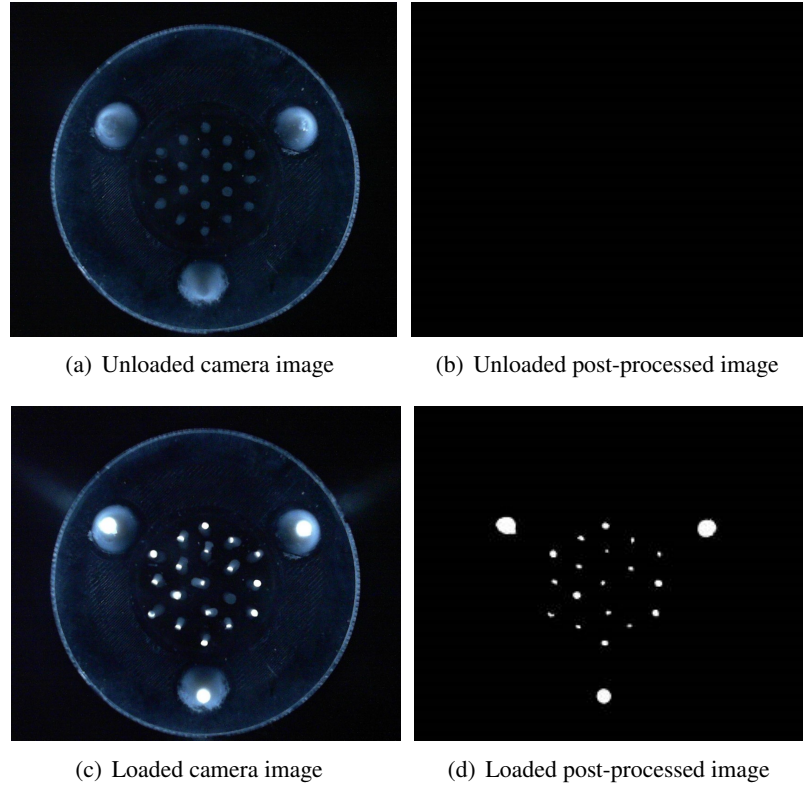


Figure 4.22: The proposed sensor's responses under force exertion in the form of the raw image and the binary image. Two scenarios are presented: the first row is the unloaded status; the second row is exerting a normal force upon the sensor.

procedure to make the transparent silicone will be described in the next section in detail) so that geometry information can be observed. In terms of flexure, illumination and capture system, the rest of the parts remain the same as in the previous CFTS1 sensor. Therefore, this sensor prototype can simultaneously sense both the force information and the tactile information (in the form of geometry observation, as shown in Fig. 4.24).

4.4.2 Summary

In our previous work, we have proposed a tactile sensor CTS that also uses a reflective elastomer with a flexure to measure tactile information in the form of pressure distribution [93].

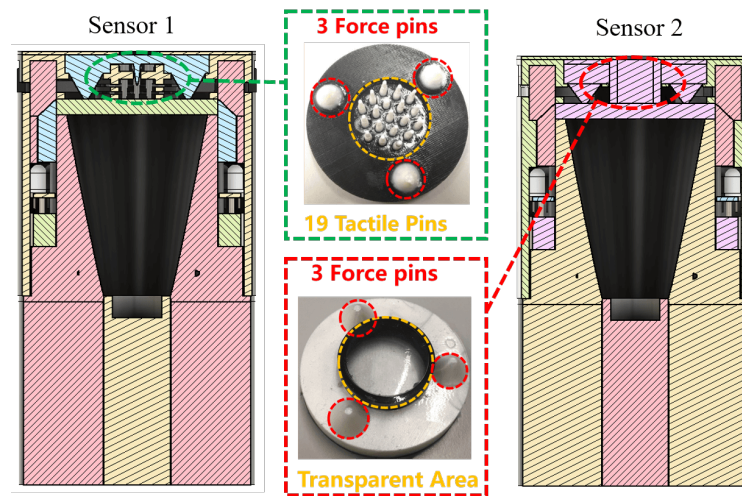


Figure 4.23: Two proposed optical-based force and tactile sensors (CFTS1 and CFTS2). Both sensors share the same sensor architecture but use different elastomer parts. Sensor 1 can sense both force information and pressure distribution; Sensor 2 can sense both force information and geometry information.

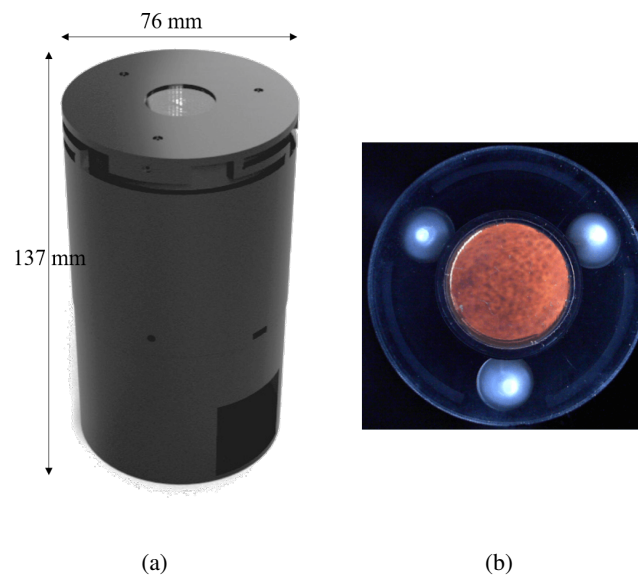


Figure 4.24: CFTS2 sensor that uses a transparent silicone component at elastomer's central area. (a) Sensor prototype. (b) Raw image captured from the bottom camera within the sensor.

However, the previous sensor cannot obtain force information. In this work, we propose an optical-based force and tactile sensor CFTS1 that uses a reflective soft opaque elastomer together with a flexible force-sensitive structure (flexure) to obtain both normal force information and spatial pressure distribution simultaneously. We have also implemented another version (CFTS2) with transparent silicone for texture observation. Our sensing device is easy to manufacture, and benefits from a wide measuring range of normal force (up to 70 N). Moreover, the device is immune to electromagnetic interference, as it uses an elastomeric material, a 3D printed structure and a camera which is situated remotely, away from the sensing area.

4.5 F-TOUCH Sensor — Force and Tactile Optically Unified Coherent Haptics Sensor

The optical-based force and tactile sensor CFTS1 [93] which has been proposed uses an opaque and reflective elastomer layer to measure both force and tactile information. However, the sensing areas of the force and tactile information are separate (Fig. 4.25(a)), which leads to ineffective measurement of both types of information from specific sensing areas. Here, we present a force and tactile sensor system that makes use of one combined area for both force and tactile sensing, as shown in Fig. 4.25(b) for a regular version (F-TOUCH0), and Fig. 4.25(c) for a minimized version (F-TOUCH). The improved sensor system is easy to manufacture, and benefits from a relatively large measuring range of forces compared with other tactile sensors (this is true only for the regular version in Fig. 4.25(b), as the minimized version in Fig. 4.25(c) does not have a wide range due to the use of very small springs). The use of transparent silicone elastomer as the sensing medium is beneficial for two reasons: its softness makes it safe to interact with, while its transparency allows for the observation of the contact object's geometry. We incorporate an elastic structure made from several springs connected to three markers attached underneath the silicone elastomer, for the purpose of measuring force information. Combining the silicone elastomer and the spring-mechanism force structure in a vertical configuration for force/tactile sensing, we focus on the use of an optical method (using a camera) to detect both

force markers and elastomer deformation from one single capture during object interaction.

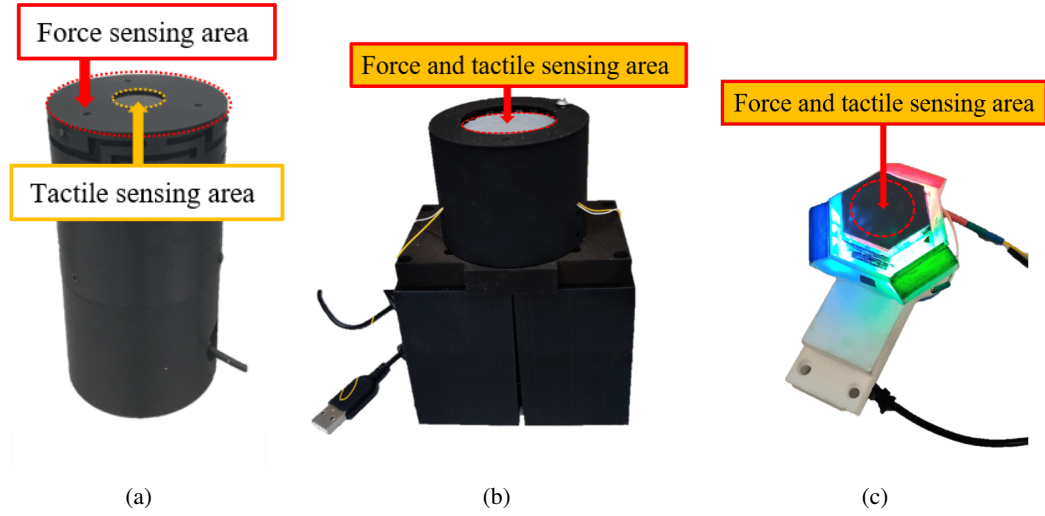


Figure 4.25: Comparison between the CFTS1 and F-TOUCH series (F-TOUCH0 and F-TOUCH). (a) CFTS1 sensor, where force and tactile sensing areas are separate. (b) F-TOUCH0 sensor, where force and tactile sensing share the same sensing area. (c) Miniaturised F-TOUCH sensor.

4.5.1 Sensor Design

In this work, two sensor prototypes will be presented. The first sensor prototype (F-TOUCH0) is an improved version of the optical-based force and tactile sensor (CFTS1) shown in the previous section Sec. 4.4, and both sensors have the same scale. The second sensor prototype (F-TOUCH) is a minimized version. F-TOUCH has a similar scale as the fingertip GelSight sensor [42].

F-TOUCH0 Sensor Design

As is shown in Fig. 4.26, the overall design of the proposed optical-based force and tactile sensor is composed of eight main parts. The soft and transparent silicone elastomer with an opaque coating (1) is an important component of the proposed sensor: it is used to measure the tactile information. The elastomer is integrated into a 3D printed shell. The three-spring structure (2) is incorporated below the silicone elastomer (see Fig. 4.29). The structure is composed

of three compression springs within a 3D printed platform. There are also three 3D printed black markers (3) attached to the upper platform. These markers move when an external force is applied and move on compression of the associated springs and are being used to measure the applied forces. The spring mechanism structure is used for supporting and stabilizing the silicone elastomer component, as well as for measuring the force information depending on the displacement of the markers. At the bottom of the sensor, there is a CCD camera (4) with manual focus to capture the deformation of the silicone elastomer together with the movement of the black markers, the raw image is then converted to force and tactile information. Besides, we incorporate a LED array (5) which contains three colours (red, green and blue) surface-mount-device (SMD) LEDs as an internal light source to effectively illuminate the silicone elastomer via the light plate (6). The light plate has two functionalities: on the one hand, it is used as

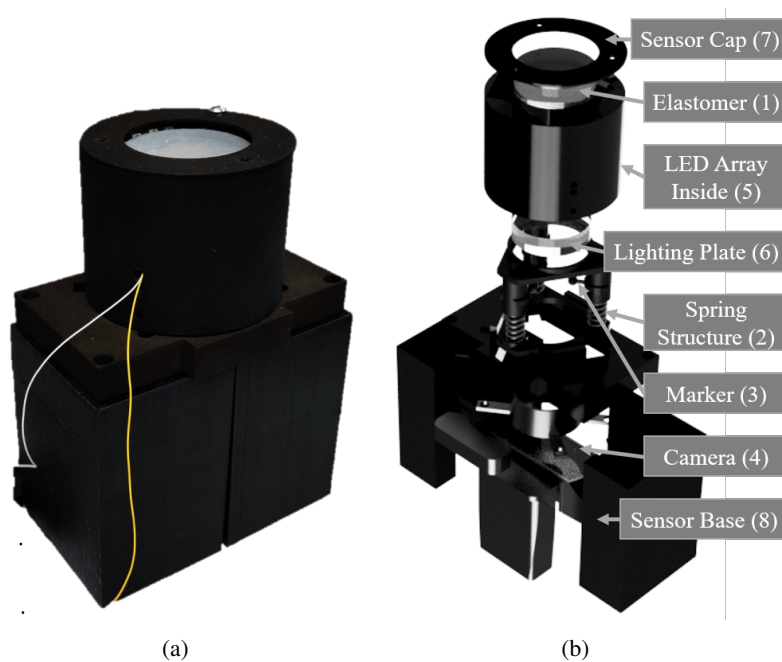
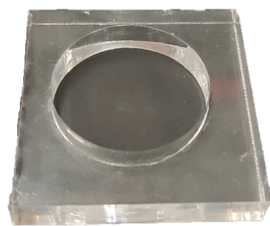


Figure 4.26: F-TOUCH0 sensor that uses a coated transparent silicone component and an elastic structure to sense both force and tactile modalities. (a) Sensor prototype. (b) Exploded view of the sensor structure.

mechanical support to connect the silicone elastomer and the spring mechanism structure. On the other hand, it is used to guide the light and help the camera observe the deformation of the silicone elastomer because of its transparency property. The assembly of the proposed sensor is completed with a top cap (7) to fix the silicone elastomer inside the shell, and the base body (8) holding the camera. The 3D printed bodies are fabricated from nylon material (PA2200) using a 3D printer, EOS P100.

The soft and transparent elastomer is a core part of our proposed sensor design; its properties largely affect the sensitivity of our sensor. The silicone elastomer component is composed of two parts: the transparent elastomer base and the reflective coating membrane. The appropriate elastomer base needs to be of the appropriate hardness and elasticity. The membrane needs to be uniform, thin and smooth.



(a)



(b)

Figure 4.27: Elastomer base description and its fabrication. (a) Mould for the elastomer base. (b) Manufactured clear base from pouring the silicone mixture into the mould.

Sensor elastomer base: as introduced in [178], there are several factors that need to be considered when choosing a transparent elastomer base for the sensor: optical transparency, stretchability, hardness, robustness, and ease of fabrication. We follow the procedure of making our optically clear and stretchable elastomer base based on the guidelines shown in [176]. We wish the sensor elastomer base to work in heavy-loaded environments which requires a relatively hard material, but also to remain sensitive during physical contact. Instead of using thermoplastic elastomers (TPEs), we used silicone elastomer Solaris from Smooth-On with a hardness Shore

A value of 15. The silicone material properties are shown in Tab. 4.4. Solaris always comes in two liquid parts known as Part A and Part B. To make the clear elastomer base, we mixed the two parts with Slacker, which is a liquid additive to adjust the softness. The most appropriate proportion of each part is 1 : 1 : 1 in weight – these proportions were found through a trial and error study. We put the mixture of the silicone into a conditioning planetary mixer (THINKY ARE-250) and mixed the liquids for 1 minute at 1000 revolutions per minute (also known as rpm) and degassed for 1 minute at 1000 rpm. Following that, we poured the resultant silicone mixture into a 38 mm diameter cylinder mould which was laser-cut from a 10 mm thickness clear acrylic sheet (as is shown in Fig. 4.27(a)). The curing process of the elastomer base took 24 hours. In practice, our proposed sensor elastomer (shown in Fig. 4.27(b)) works well (in cooperation with the elastic structure) for heavy contact interaction with the chosen hardness.

Table 4.4: Elastomer Material Properties

Property	Solaris
Mix Ratio By Volume	1A: 1B
Tensile Strength	180 psi
Elongation at Break	290 %
Colour	Clear
Shore Hardness	15 A
Specific Gravity	0.99 g/cc

Sensor coating membrane: it is important to have an additional reflective thin and fine layer above the elastomer base to reflect back deformation information when interacting with the environment. The layer is required to be uniform, smooth, thin and opaque so that external light will not cause interference to the sensor. In general, different reflective properties determine different optical designs. In our design, we choose a matte coating that used 99+% 1-micron aluminium powder as the coating pigment, since it gives a good performance for measuring common shapes grasped by robot end effectors. To make a thin and even coating membrane, we dispersed the pigment in a silicone paint base and added organic solvent toluene to lower the viscosity of the mixed liquids. Then we used an airbrush to evenly distribute the liquid

mixture on the surface of the manufactured elastomer base. A fine elastomer membrane (shown in Fig. 4.28(a)) needs several layers (of around 1 mm thickness in total) of airbrushing, and it required additional careful cleaning of the surface after the airbrushing. A fine and completed membrane can reveal the fine details on the object. Fig. 4.28(b) shows the inside view of the elastomer coating when pressing a USB cable connector against the top surface.

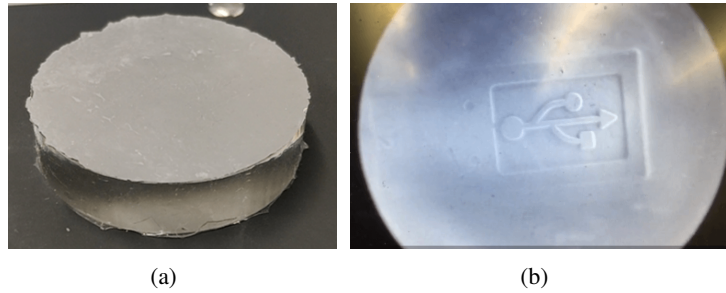


Figure 4.28: Matte coating using aluminium powder. (a) A piece of the manufactured elastomer. (b) View from the bottom surface of the elastomer when a USB cable connector is pressed against the elastomer top surface.

Another key aspect of our proposed sensor is the spring mechanism structure which is placed under the silicone elastomer; the structure contains three compression springs and three markers to measure the force information within an optical way. Assembled and exploded views of the sensor elastic structure are shown in Fig. 4.29. The structure is composed of the following four parts. The upper platform (1) is used to hold and fix the lighting plate and a silicone elastomer component. Three identical $38\text{ mm} \times 12\text{ mm}$, 2 N/mm compression springs (2) are, at one side, connected to the upper platform and, at the other side, attached to the bottom platform (4). Three black markers (3) are attached to the underside of the upper platform (1). All the parts apart from the springs are 3D printed using nylon material and are painted in black.

It is noted that the movement of each marker is coupled with the deformation of the corresponding spring. When the sensor is not interacting with an object surface, the centroid of each spherical marker is at the same height, forming a plane that is in parallel to the elastomer bottom surface. During the interaction with an applied load, the physical contact upon the sens-

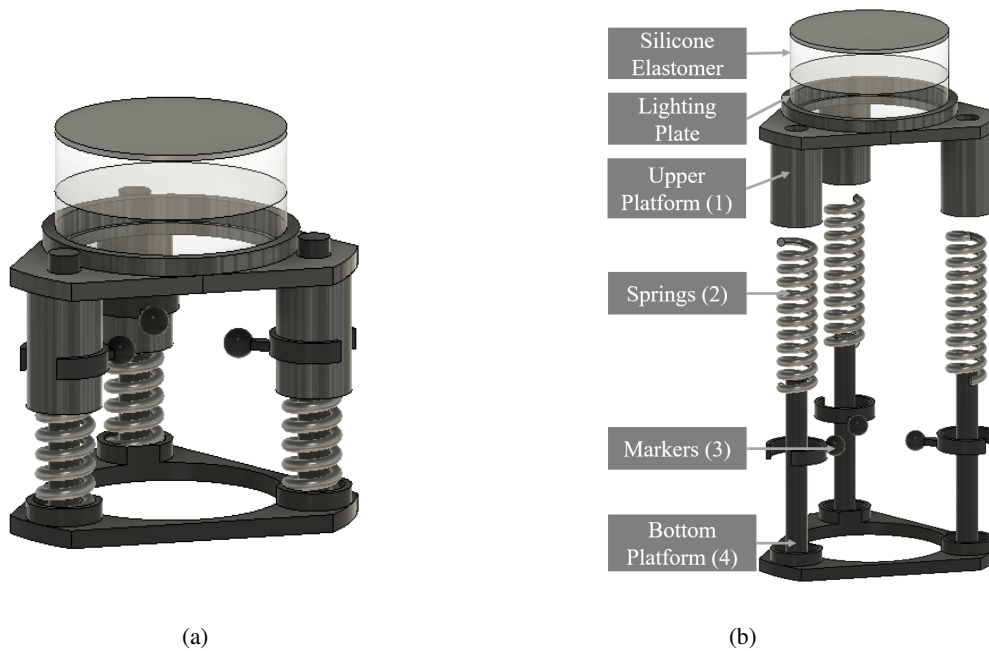


Figure 4.29: CAD drawing of the proposed spring mechanism structure (elastic structure) that is made up of three compression springs and three markers. (a) Assembled view of the structure. (b) Exploded view of the structure.

ing medium leads to a compression of the three springs and results in a movement of the upper platform, in turn, leading to a movement of the related spherical markers. We used a camera underneath the spring mechanism structure to capture the movement of each marker and compute the force information based on the motion of the corresponding centroid and the area changes. We chose the markers to be black in order to create a contrast to the silicone elastomer background so that they can be easily tracked and segmented. It needs to be emphasized that the markers are used to measure the net force since the spring constant of each compression spring is relatively low compared with the hardness of the silicone elastomer component. When an external load is pressing against the sensor, the whole spring mechanism structure will move as an integration together with the elastomer component.

The illumination system within the proposed device also plays an important role during the

sensing process. The illumination is implemented using LEDs in three colours (red, green and blue) in a closed environment since the device requires a sensitive response on image capture for tiny membrane deformation. We use 36 SMD LEDs (Osram Opto Power TOPLED Lens) in total with a viewing angle of 30 degrees of the emitted light. All LEDs are integrated into three individual customized printed circuit boards. In each board, 12 LEDs with the same colour are arranged into a 3×4 array. The three circuit boards are installed inside the sensor shell, as shown in Fig. 4.30. As for the silicone elastomer supporting and image capture, a transparent circular-shape acrylic plate is laser cut and placed under the elastomer base, and is fixed within the upper platform of the spring mechanism structure (Fig. 4.29(b)) as the supporting plate. For the image capture, a USB camera (Logitech C920), with a resolution of 640×480 pixels, manual focus and a frame rate of 30 fps, is mounted inside the sensor base (Fig. 4.26(b)) and is 40 mm away from the supporting plate, allowing for an effective capture of the visible area of both the silicone elastomeric structure and the markers which are attached within the spring-mechanism structure.

When the sensor is connected to a laptop via the USB webcam, and we switch on the power

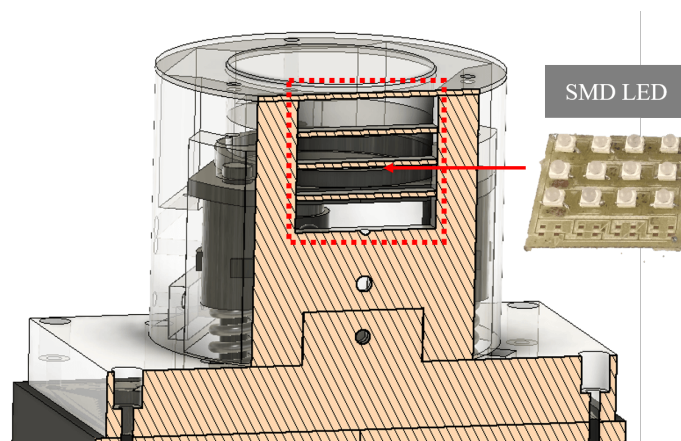


Figure 4.30: CAD drawing of the illumination system within the F-TOUCH0 sensor. Three colours (red, green and blue) of SMD LEDs, each with 12 pieces, are soldered within three individual PCBs, and the PCBs are installed inside the preserved holes within the 3D printed sensor shell.

for LED arrays, three different colours of RGB lights are emitted from different directions to illuminate the unloaded sensing element (silicone elastomer structure and markers within the spring mechanism structure). The raw images are received by the camera at the sensor base, as shown in Fig. 4.31.

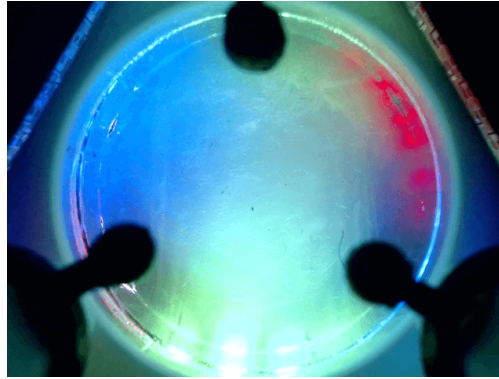


Figure 4.31: Camera view of the unloaded sensing element (the elastomer surface). The circular area (illuminated by the RGB colour) is the elastomer's sensing surface, where texture information can be observed. The three small circular black areas are the markers that are being traced for force measurement.

The procedure of segmenting force-related information from the tactile image can be concluded in the following steps, as shown in Fig. 4.32. The entire process follows what GelSight sensor does [176] but with some different operations. Firstly, we take an initial image when no marker is attached on the spring-mechanism structure. Then we apply a circle-shaped mask on the taken image so that the areas outside the circle mask turn to black (value 0). The new image is saved as Frame0. Then we apply low-pass Gaussian filter (3 by 3) on Frame0 to get a so-called background Frame0_l and save it locally. When we press an object on the surface of the elastomer membrane, the camera captures the raw image. We apply the same circular mask on the image to get the image Frame. Then we do an image subtraction $\text{Difference} = \text{Frame0}_l - \text{Frame}$ to obtain the differential image, in which the three black markers are in a dark colour, and the surface deformation will have a large colour difference. Based on the differential image, we apply a threshold to segment the dark areas from the background, which represents the areas of

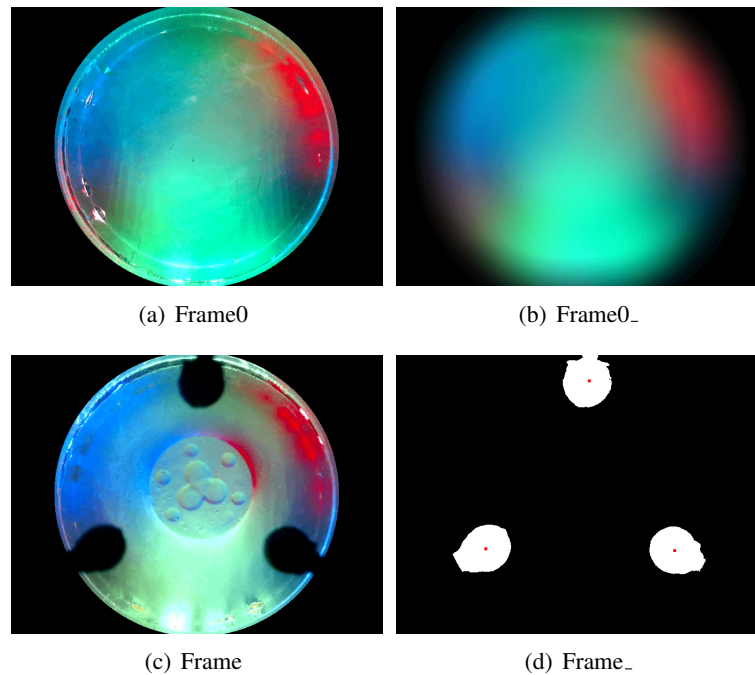


Figure 4.32: The procedure of segmenting force-related information from the tactile image. (a) The initial image with a circular mask Frame0 when no marker is attached to the elastic structure; (b) after applying low-pass Gaussian filter we obtain Frame0_ from Frame0 as the background; (c) apply the same circular mask to the captured image to get the RGB image Frame when an object is in contact with the elastomer membrane; (d) after image subtraction between the background Frame0_ and the current image Frame, we apply thresholding to obtain the mask of the image which includes the three markers, namely Frame_, we calculate the centroid (shown as the red dots) and the area of each marker to record the markers' status for force measurement.

three markers. Then, we calculate the centroid of each marker area from the binary image, and we obtain the image Frame_ with the marker position M , which together with the marker area A , will be used to calculate the force information. Besides, optical flow can also be considered for tracking the change of both the markers and the tactile background.

F-TOUCH Sensor Design

A functional force and tactile sensor should be small in volume in order to be compatible with a robotic hand or gripper. At the same time, it is important that it provides real-time tactile feedback to assist the robot. The fingertip GelSight sensor is a good example of a vision-based

tactile sensor that embodies these characteristics. As described in the previous section, the chief advantage of its design is the size reduction relative to the original prototype [67], i.e. into a miniaturised form factor [179] to fit a jawed gripper. The GelSight sensor obtains the geometry of the contact object together with the contact force, which achieves the integration of multiple modalities within one sensing device. However, a large number of black markers are directly painted onto a transparent elastomeric layer (covered with a reflective-coating membrane). Their intended use is to enable the acquisition of force information, however, this leads to the merging of force and tactile information, which meets the requirement of perceiving multiple modalities, but makes it difficult to separate one information source from the other. This is even more of a hindrance when it comes to sensor calibration, especially for the force/torque modality, as it is influenced by the contact geometry during measurement acquisition [176].

Taking inspiration from the GelSight sensor, we propose the F-TOUCH (force and tactile

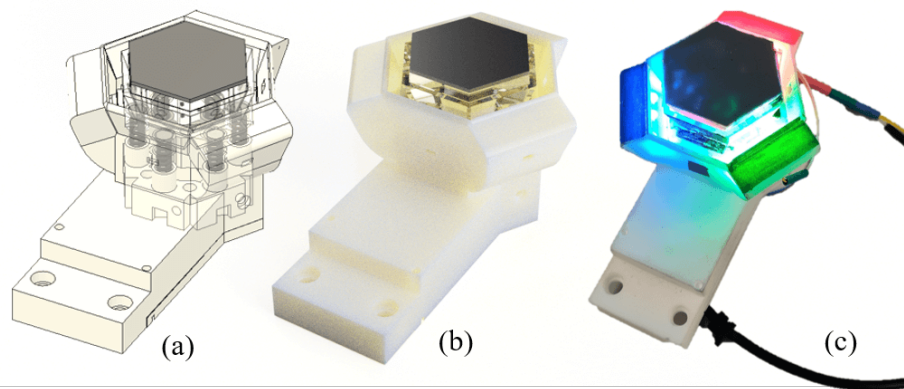


Figure 4.33: The proposed F-TOUCH sensor. From left to right are (a) computer-aided design (CAD) view of the sensor, where an internal spring-mechanism structure with three markers is used to measure six-axis force/torque components. (b) Rendering model of the sensor. (c) The manufactured prototype of the sensor. The internal RGB LED light arrays and the webcam are powered via two USB cables, respectively. Both USB cables are connected to a PC. Our sensor is inspired by the fingertip GelSight sensor.

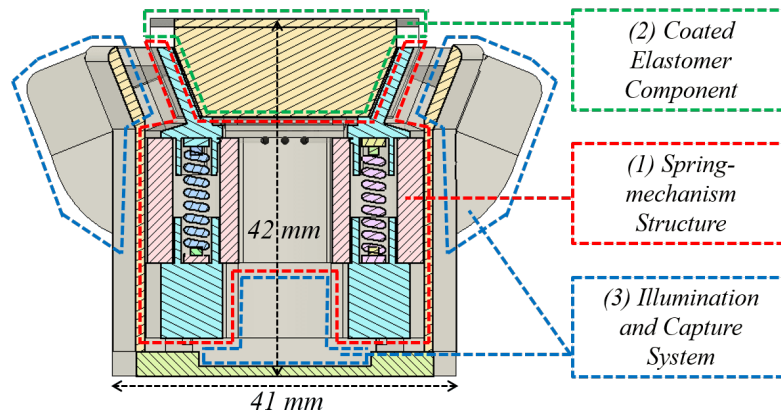


Figure 4.34: Schematic of the design of the proposed sensor. Three parts are needed for the device assembly; (1) the spring-mechanism structure is a six-axis platform that holds the (2) coated elastomer component acting as the sensing medium. A camera at the bottom concurrently captures the marker movements and area changes within the spring-mechanism structure, as well as the deformation of the elastomer surface illuminated by internal LEDs. Both the camera and the LEDs make up the (3) illumination and capture system.

optically unified coherent haptics) sensor, as shown in Fig. 4.33. The F-TOUCH_3.2 sensor is enhanced with a force/torque measurement capability by virtue of an enhanced physical elastic structure and improved calibration method. As shown in Fig. 4.34, the proposed vision-based sensor is composed of three main parts: (1) spring-mechanism structure; (2) coated elastomer component; and (3) illumination and capture system.

The spring-mechanism structure is critical to the proposed sensor design. This force-related elastic structure provides six degrees of freedom (allowing six-axis force/torque measurements) and is placed inside the sensor body (as shown in Fig. 4.36). Having more degrees of freedom, the proposed sensor can compliantly adapt to different types of contact conditions. The spring-mechanism structure is composed of six components (as shown in Fig. 4.35), which can be subdivided into three categories: the upper assembly, the mid-section and the lower assembly.

From the exploded view in Fig. 4.35, the upper assembly consists of the elastomer holder (1) and the black markers (5). The elastomer holder is a transparent hollow hexagonal tray which contains the coated elastomer layer (more details are provided in the next sub-section); a 1-mm-

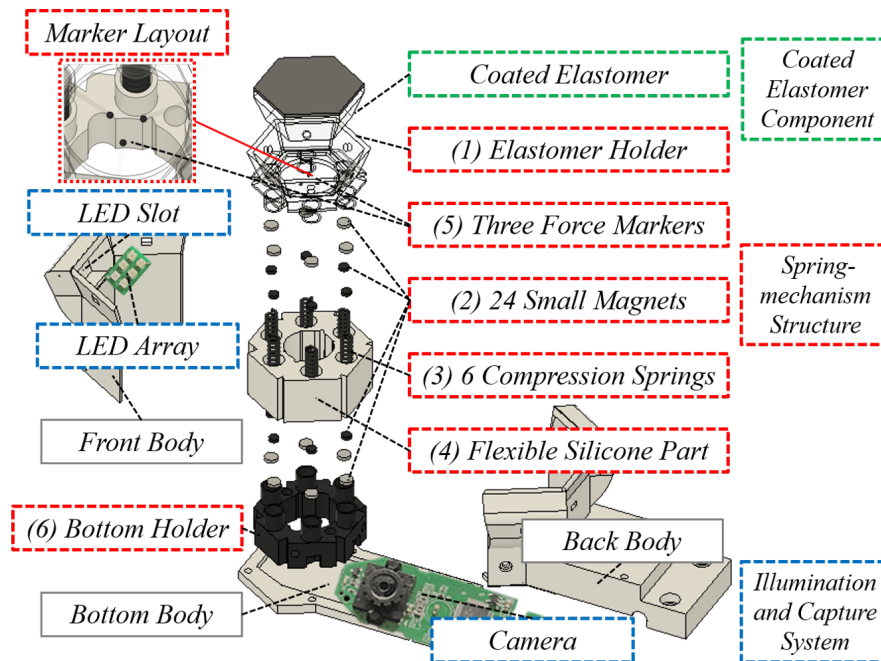


Figure 4.35: Exploded view of the proposed sensor spring-mechanism structure. Six parts (1)-(6) make up the structure: namely, the upper assembly, mid-section and lower assembly: (1) elastomer holder and (5) black markers compose the upper assembly; (3) 6 springs, (2) 24 magnets and (4) a flexible silicone compound compose the mid-section of the structure; (6) bottom holder composes the lower assembly.

thick clear acrylic sheet is laser-cut to fill out the middle of the tray. Three markers are situated in the middle of the elastomer holder, held in place by three thin supports. The elastomer holder together with the three markers is 3D-printed as one contiguous ensemble. It uses clear material (VeroClear®) to facilitate LED illumination. The markers are drawn in black with an acrylic paint pen after fabrication. At the base of the elastomer holder, six 4-mm-diameter magnets are glued inside six reserved apertures to allow connection with the springs of the mid-section. In the mid-section, six compression springs (3) (with a 3-mm-diameter magnet glued to either end of each spring, for a total of 12 magnets) are passed through a white silicone flexible compound (4) to connect the upper assembly and the lower assembly. The compression springs are of 15 mm length, 4 mm in diameter, and of 0.5 mm wire diameter. The connections rely on magnetic attraction (2), which provides a very stable hold. A flexible, hollow silicone component made

from an Ecoflex 00-30 platinum-cure silicone rubber compound (see Tab. 4.5) covers the six springs, for a stable connection between the upper assembly and the lower assembly. Also, it enables a wider range of force/torque measurement. The lower assembly consists of the 3D-printed bottom holder (in nylon material) (6), where another set of six 4-mm-diameter magnets are glued on, in the same way as on the upper assembly's surface plane. The lower assembly cradles the camera lens; the hollow of the bottom holder frames the camera lens and keeps it trained on both the black markers and the coated elastomer surface. The proposed spring-mechanism can sustain a maximum normal load of up to 8 N during testing.

We can view the movements of the three black circular markers as reciprocal with the compression of the six springs. We estimate the six-axis force/torque components by observing the markers' movements and their area changes, as relayed by the camera. When an external force is applied on the elastomer, the exerted force/torque components will cause a compression of the spring-mechanism structure. Because of the connectivity between elastomer and spring

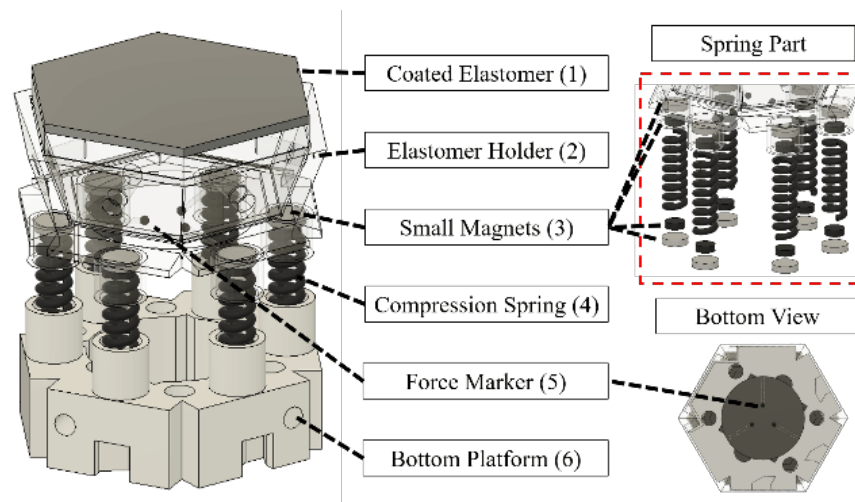


Figure 4.36: CAD drawing of the proposed spring-mechanism structure, which is made of five components shown as (2) to (6). The top section is composed of the elastomer holder which has 6 magnets glued at its downward plane. The middle section includes 6 springs with 12 magnets glued on both ends. The bottom platform has 6 magnets glued on its upward plane.

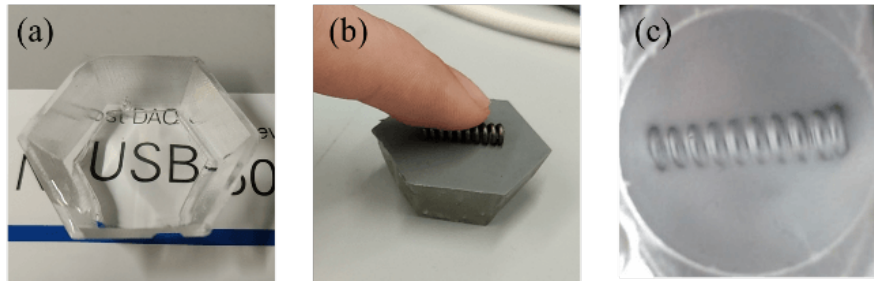


Figure 4.37: Manufactured silicone elastomer component. (a) The transparent silicone base placed on a piece of paper. (b) A small spring is pressed against the coated elastomer component. (c) Camera view from the underside of the coated elastomer capturing the distortion of the elastomer's coated surface.

structure, these movements, as well as the areas of the three circular markers within the spring structure, will be coupled to those of the sensing medium. A more detailed explanation will be provided in the following paragraphs. It is worth noting that the spring-mechanism structure is designed to measure six-axis force/torque information, as the coated elastomer has a relatively high rigidity compared to the low-spring-constant compression springs and soft flexible silicone compound. The state of the captured markers is directly related to the overall force/torque components exerted upon the sensing medium.

Table 4.5: Silicone Material Properties

Property	Ecoflex 00-30	Solaris	Psycho Paint
Mix Ratio By Weight	1A:1B	1A:1B	1A:1B
Elongation at Break	900%	290%	1,000%
Shore Hardness	00-30	15 A	Not Given
Colour	Translucent	Clear	Translucent

The nature of the elastomer component largely determines the sensor's performance. It is made up of two parts: the elastomeric base and coating membrane. To create a suitable elastomeric base for tactile sensing, the materials used need to be optically clear, soft yet robust, and readily available. Li and Adelson [91] recommend a Shore hardness range for the elastomeric base that is between Shore A values 5 and 20. Following this recommendation, we use So-

laris (part A and part B) with Shore A 15 (see Tab. 4.5) and Slacker (used to increase softness) from vendor Smooth-On® to produce the transparent elastomeric base. A ratio of 1:1:1 for each component has proven to be ideal for making an elastomeric base with the appropriate hardness [176]. As for the coating membrane, it is a very thin but reflective layer that covers the upper surface of the transparent elastomer. The layer needs to be thin, uniform and smooth. A matte coating, made by mixing silicone and fine metallic powders [13], is preferable for tactile sensing, as it is effective at revealing detailed shapes on the contact surface. We use a platinum-cure silicone named Psycho Paint (see Tab. 4.5), and we disperse aluminum powder into a silicone paint base for the coating on top of the elastomer base. In practice, an elastomeric component fabricated in this way is able to sustain a moderate force/torque exertion while revealing the fine geometry of the contact object's surface (see Fig. 4.37), which is comparable to the GelSight sensor's elastomer.

The illumination and capture system provides the physical basis for the disaggregation of force-related information from the tactile image. We use RGB SMD LEDs (Osram® Opto Power TOPLED Lens) within the sensor body for internal illumination. The reason for choosing RGB

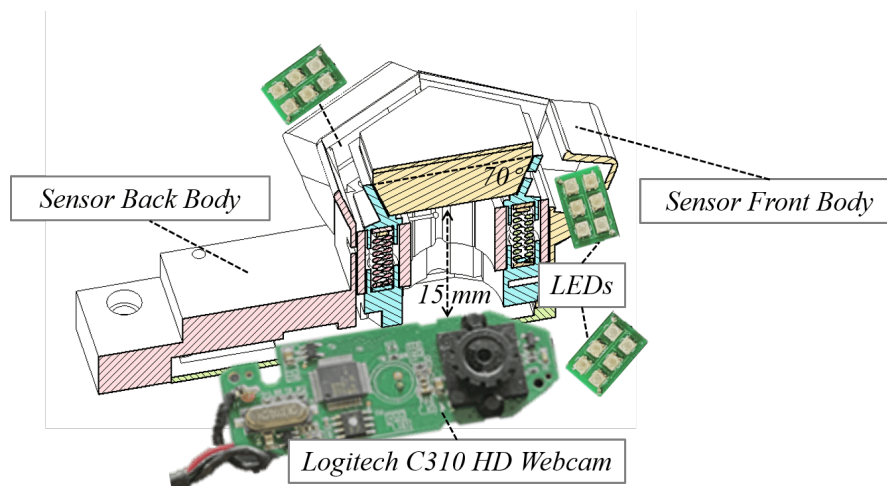


Figure 4.38: Illumination and capture system within F-TOUCH_3.2. Three RGB LED arrays are employed for internal illumination, and an off-the-shelf camera is used for image capturing.

colour is based on the fact that the initial GelSight sensor [67] used monochrome illumination but later switched over to RGB illumination for surface reconstruction [42]. In our view, the illumination scheme that uses RGB colour will be more effective in the future, in particular for geometry reconstruction and recognition in GelSight's case [176]. Besides, it is also easy to extract the black markers from the RGB background via simple thresholding, which enables real-time force and tactile data acquisition. Fig. 4.38 presents the configuration of the proposed illumination and capture system: three PCBs, each with six LEDs (arranged into 2×3 arrays) of the same colour, are installed within predesigned slots on the sensor body. As described above, we use a clear elastomer holder to contain the transparent elastomer component, as the tray can homogenize the LEDs' light while allowing a high transmission rate. An off-the-shelf webcam (Logitech® C920, manual focus, resolution of 640×480 pixels, 30 frames per second) is placed about 15 mm away beneath the elastomer holder. We manually set the focal length so that the camera can capture a high-resolution tactile image, while concurrently capturing the three black circular markers – for acquisition of force-related information.

The key contribution of the proposed sensor is the capability to concurrently and effectively perceive dual modalities. In F-TOUCH_3.2, a unitary force and tactile sensing capability is integrated within a single sensor housing, with signal acquisition being performed by a single monocular camera acting as the transducer.

As elaborated in the above paragraphs, the measurement of the net force/torque components is based on the position and area changes of the three black markers contained within the elastomer holder. Since the elastomer component is glued inside the elastomer holder, we can treat both parts as constituting an integrated whole. Hence, the movement of the elastomer holder can be seen to represent the net external force/torque applied upon the sensing medium. When no contact occurs, the camera captures the illuminated elastomer surface and the markers. The next step is to segment the force-related information from the tactile image background. Since we use RGB light as internal illumination, and the markers are painted black, we convert the raw captured image into greyscale and apply a Gaussian filter for smoothing. We then set a threshold

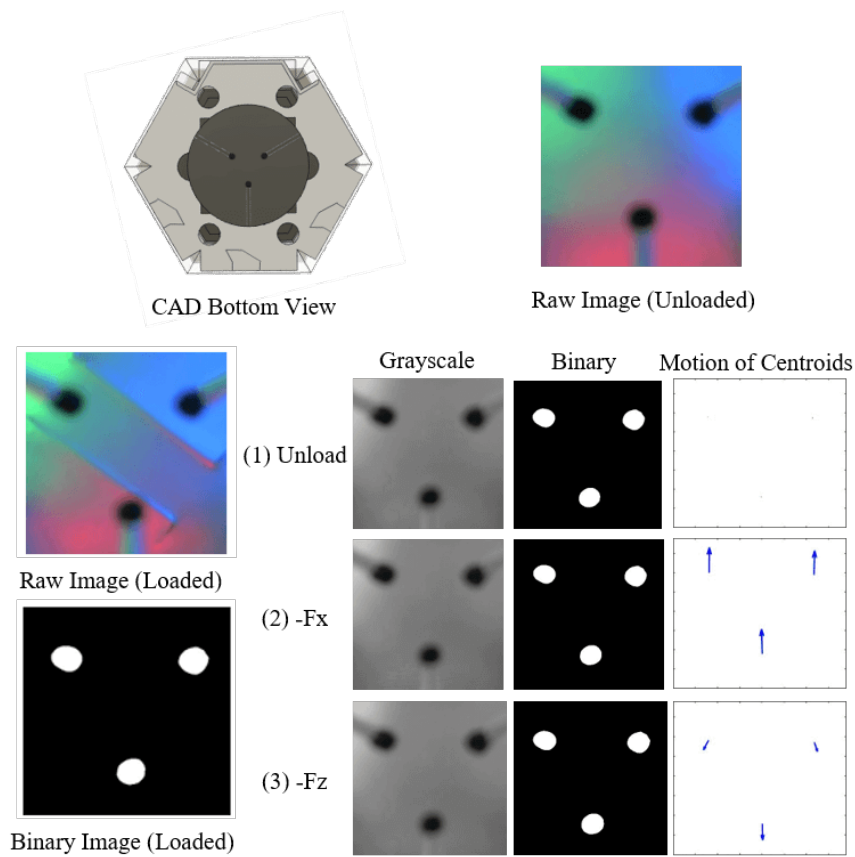


Figure 4.39: Force information segmentation: The top is a bottom view of the CAD spring-mechanism structure, where force markers are circularly attached beneath the coated elastomeric component, and the raw unloaded captured image. The left is the raw loaded captured image. Bottom left is the binary image after filtering and thresholding. The right part shows the sensor's responses under different force exertion in the form of the greyscale image, reverse binary image and the motion of each marker centroids in the vector plot. A scale is multiplied to the marker's centroid movements; therefore, motions are enhanced for better observations.

and reverse the colour back to the filtered greyscale image to obtain a binary image. Fig. 4.39 demonstrates the process of force-related information segmentation from the tactile image and the corresponding sensor responses where unloaded status and loaded status are considered.

As described in the above paragraphs, we assume that the centroids of each of the circular markers are within a plane that is in parallel to the elastomer's surface plane. For example, a normal force acting on the center point of the sensing medium leads to a height difference of

the markers' plane with respect to the reference (unloaded) state. Effectively, the markers come closer to the camera and thus appear larger in the camera images. In other words, a change in distance between a marker and the camera leads to a change in the area covered by the marker's camera image. When normal force and shear force are concurrently applied to the sensing medium (the elastomer plane), the distance between the markers' plane and the camera changes (and the markers' plane experiences a tilt), resulting in a marker area change as well as a marker movement across the camera image. Our aim is to track the movement of the three markers along with their area change, thus we detect and label the markers in the binary image (see Fig. 4.39). We then calculate both centroid positions and areas of the three labelled markers in the image. We set the original x, y coordinate values of each marker in unloaded condition as $x_i(0)$ and $y_i(0)$ and the corresponding area as $a_i(0)$ where i is the label index $i=1,2,3$. During the contact, we calculate the changes of both the markers' centroid positions (all displacements are in Cartesian coordinates $\Delta x_i(j) = x_i(j) - x_i(0)$, $\Delta y_i(j) = y_i(j) - y_i(0)$ and the areas $\Delta a_i(j) = a_i(j) - a_i(0)$ for each frame j , where ($i=1,2,3$). We then visualise the markers' centroid motions as vector plots, along with the respective area changes. Fig. 4.39 depicts the F-TOUCH_3.2 sensor responses in the form of marker motions and area changes under nine different loading conditions, where different force/torques are applied (will be explained in detail in the next chapter). Having obtained values for the nine variables Δx_1 , Δy_1 , Δa_1 , Δx_2 , Δy_2 , Δa_2 , Δx_3 , Δy_3 , Δa_3 from three markers, we can proceed to six-axis force/torque calibration of the sensor.

The calibration process and experimental results of the F-TOUCH sensor will be provided in the next chapter.

4.5.2 Summary

To summarize, force and tactile sensing has experienced a surge of interest over recent decades, as it conveys a range of information through physical interaction between the sensing device and the environment. Tactile sensors aim to obtain tactile information (pressure, geometry etc.) and one popular example is the GelSight sensor. However, tactile sensors normally cannot perform

force measurements as good as force sensors do due to the sensor architecture difference. This work presents a novel design for a vision-based sensor (namely F-TOUCH) inspired by the Gel-Sight sensor. In addition to acquiring tactile information of a geometry nature, our sensor uses an elastic structure (as what force sensors have) that enhances force/torque measurements along multi-axis. The proposed sensor contains three key components: a coated elastomer layer acting as the sensing medium; a spring mechanism acting as an elastic structure; and a camera placed at the foot of the device for image capture. The latter concurrently records the deformation of the elastic structure and the distortion of the elastomer surface to acquire force and tactile information. The sensor is calibrated with the use of a commercial force/torque sensor. In experiments, the F-TOUCH sensor achieves an excellent force performance as a commercial force sensor and captures the contact object's geometry in the meantime.

4.6 Summary of the Chapter

To summarize, we present several force and tactile sensor prototypes based on the proposed optical-based sensing methodology. These use a camera as the transducer to sense both modalities of force and tactile information within a combination of an elastic structure and an elastomer layer. The proposed sensor matches the high fidelity of stand-alone force and tactile sensors. We describe the design and fabrication process in detail for each sensor prototype, and experimental results of the proposed sensors will be presented in Chapter 5.

Chapter 5

Experimental Validation of Sensor Performance

5.1 Introduction

This chapter presents and discusses the experimental results of the proposed optical-based force and tactile sensors described in the previous chapter (Chapter 4). The proposed sensors follow the concept of integrating both tactile sensing and force sensing capabilities within one sensor housing with the use of a combination of an elastomer layer and an elastic structure above a camera. The experimental result of the optical-based tactile sensor CTS is introduced in Sec. 5.2. The experimental result of the optical-based force and tactile sensor CFTS1 is introduced in Sec. 5.3. Finally, the experimental result of the F-TOUCH sensor is introduced in Sec. 5.4.

5.2 CTS — Camera-based Tactile Sensor

As described in Sec. 4.3, this work presents an optical-based tactile sensor CTS that uses a combination of an elastomer layer and an elastic structure (with cantilever beams) above a camera to sense pressure distribution, as shown in Fig. 5.1. The proposed sensor contains three components: a coated elastomer layer (the sensing medium) with 91 tactile elements on its underside surface; a cantilever structure supports the elastomer layer, acting as an elastic structure; and a

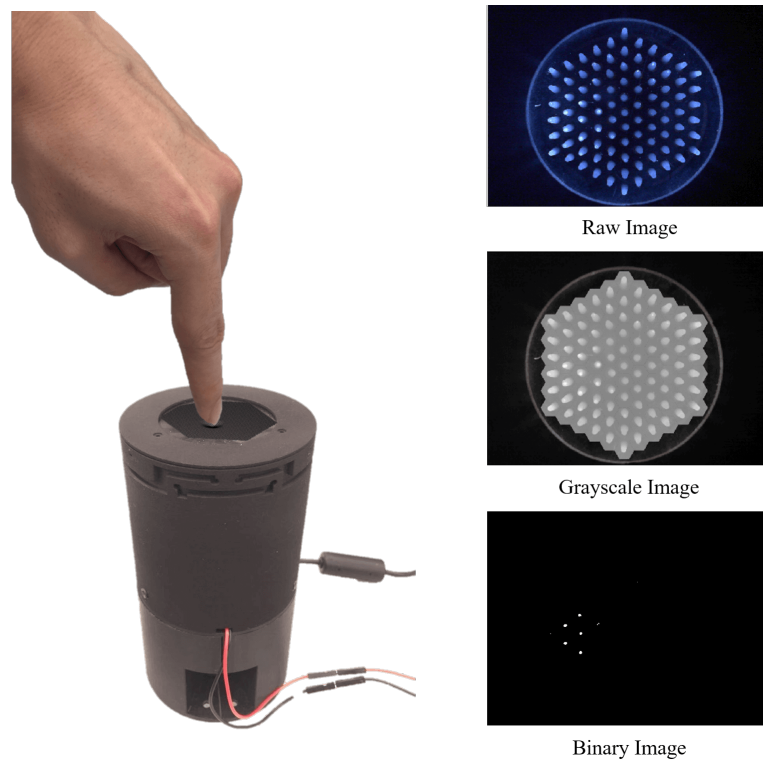


Figure 5.1: Manufactured optical-based tactile sensor and its response when a contact occurs. Left shows a single-point touch and right shows the corresponding raw image, greyscale image and binary image captured from the internal camera.

camera located at the bottom of the sensor for image capture. The camera captures the deformation of the reflective conical tactile elements (illuminated by an internal white light source) of the elastomer layer to obtain the tactile information in the form of pressure distribution. The experimental result proves the viability of the proposed methodology for tactile sensing, and the sensor prototype can detect both single-point touch and multi-point touch.

5.2.1 Visualization of Tactile Information

In our proposed tactile sensor, tactile information is measured in terms of pressure distribution. The pressure distribution is visualised from the number of activated pixels of all 91 tactile element pins. We use the scattered data interpolation method to plot the interpolated surface of

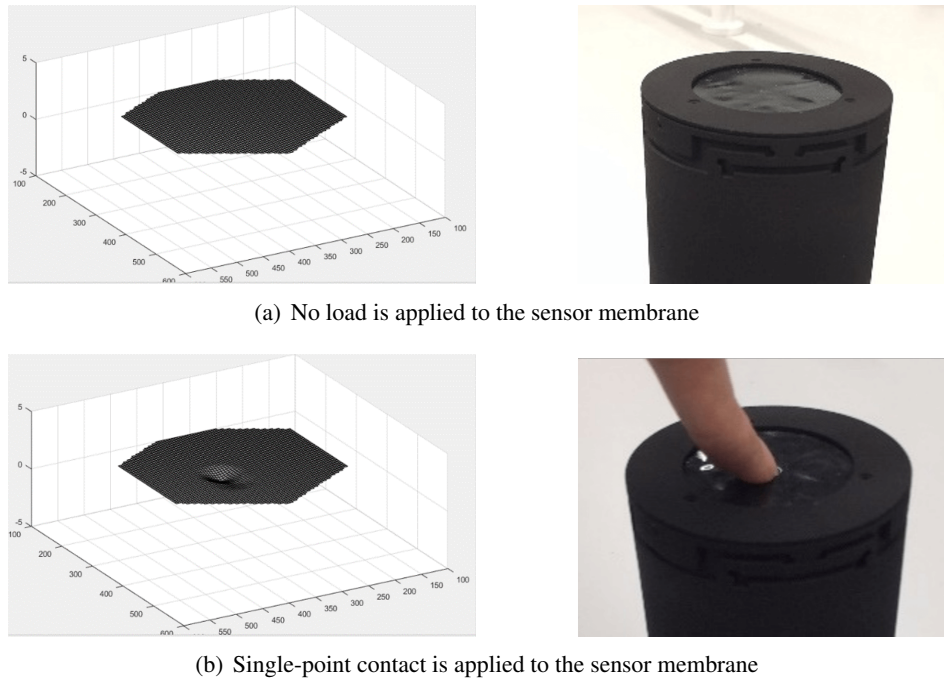


Figure 5.2: Reconstructing surface of the sensor membrane displaying the visualised tactile information in the form of pressure distribution. Two scenarios are presented: (a) unloaded status; (b) single-point contact is applied.

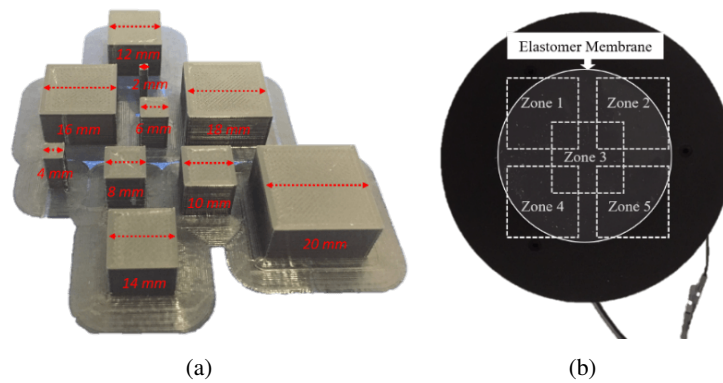


Figure 5.3: Setup for different object test. In (a), 10 cuboids of different sizes are 3D printed to test the sensor touch ability. In (b), 10 cuboids are placed one by one in Zone 1 to Zone 5 (within the sensor membrane) respectively, and the process is repeated for 10 times for each test to evaluate the sensor performance.

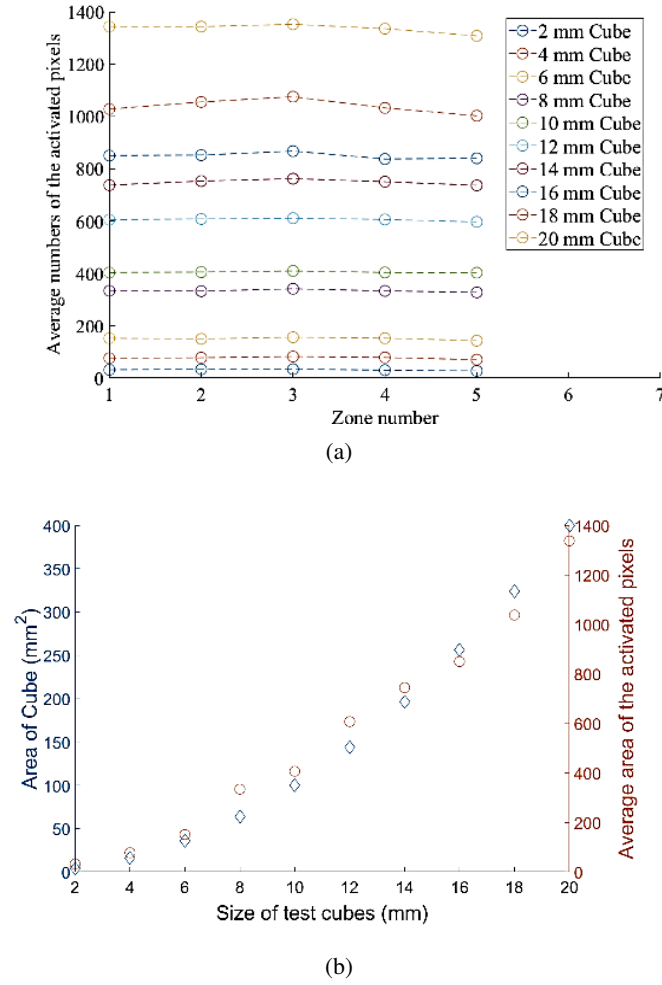


Figure 5.4: Results for different object testing. (a) Average number of the activated pixels while palpating cubes that differ in side length by 2 mm. Each test is repeated for 10 times for data collection. (b) The average number of the activated pixels collected from the sensor camera versus the areas of testing cubes.

the elastomer membrane. We apply triangulation-based natural neighbour interpolation, which is an efficient trade-off between the linear and cubic method to support 3-D interpolation. The greyscale pressure colour map is built when an external contact is applied to the sensor membrane. Moreover, we can also model the physical material by using a thin-plate spline function. When there is no contact, the initial reconstruction status of the surface in our method is shown

in Fig. 5.2(a). To evaluate the tactile response of the proposed sensor, several tests including single-point touch, multiple-points touch is applied to the sensor. These tests aim to verify that the system can detect touch. Firstly, we test the single-point touch to the sensor, as shown in Fig. 5.2(b). The sensor can detect and visualise the pressure on the reconstructed surface.

Then, we test the single-point touch with objects of different dimensions to investigate the touch ability (10 cuboids with a side length of 2 mm to 20 mm with an increment of 2 mm , see Fig. 5.3(a)). We segment the sensor membrane into five zones, as shown in Fig. 5.3(b), then we push each cube into each zone and calculate the sum of the activated pixels of the received images and repeat for ten times. We then calculate the averaged activated pixels of the sensor for each cube under different zones and plot, as shown in Fig. 5.4. The results show that the sensor

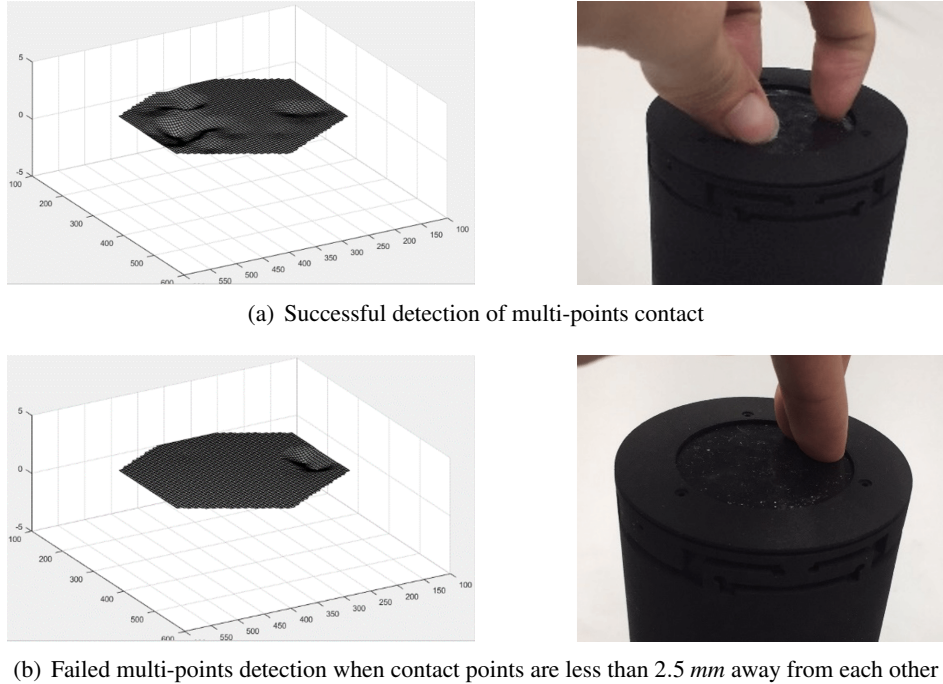


Figure 5.5: Reconstructing surface of the sensor membrane displaying the multi-points contact detection. (a) A successful detect of three-points contact with human fingers. (b) Failed multi-points detection happens when contact points are too closed to each other, specifically less than 2.5 mm .

can detect the different size of cubes over its whole surface and can recognize its corresponding dimensions.

Finally, we test with multi-points touch, and the sensor is able to detect three-fingers touch, as shown in Fig. 5.5(a). However, a misdetection happens when two fingers are very close to each other as the sensor regards the touch as a single-point touch. This is due to the mechanical problem and the minimum spacing distance between multi-points is less than 2.5 mm, as shown in Fig. 5.5(b).

5.2.2 Summary

This work presents an optical-based tactile sensor CTS that uses a coated elastomer layer with 91 tactile element pins to sense the tactile information in the form of pressure distribution. The sensor detects the tactile information via its surface deformation measured based on an optical method. The pressure is detected relying on analyzing the area change of each reflective conical tactile element pin recorded by the internal camera when a load is applied. The fabrication procedure in Sec. 4.3 shows the manufacturing of the elastomer layer using different silicone materials, as well as other components (LED arrays, etc.) of the sensor. Test results show the feasibility of the sensing approach, together with the accuracy of the sensor in detecting different objects. Future work will mainly focus on expanding the sensing capability into the force-related region.

5.3 CFTS1 — Camera-based Force/Tactile Sensor

As described in Sec. 5.2, we have proposed an optical-based tactile sensor CTS that uses an elastomer layer and an elastic structure to detect pressure. Based on this tactile sensor, we then achieve a force measurement functionality upon a similar sensor architecture. The resulting sensor is an optical-based force and tactile sensor named CFTS1.

In this research, we present a novel design for an optical-based tactile and force sensing device (shown in Fig. 5.6) that operate both force and tactile sensing functions within one hous-

ing. In addition, the tactile information is measured in the form of pressure distribution from the surface of objects. The proposed sensor is made of soft and compliant materials (an opaque elastomer) together with a deformable elastic structure (a flexure structure). The optical sensing method is used to measure both force and tactile information simultaneously based on the deformation of the reflective elastomer structure and the flexure structure. We have presented the fabrication process and development principles of the sensor in the previous section Sec. 4.4. The experimental evaluation shall be shown in the following section, and the result shows that the prototype is capable of sensing normal forces up to 70 N with an error of 6.6%.

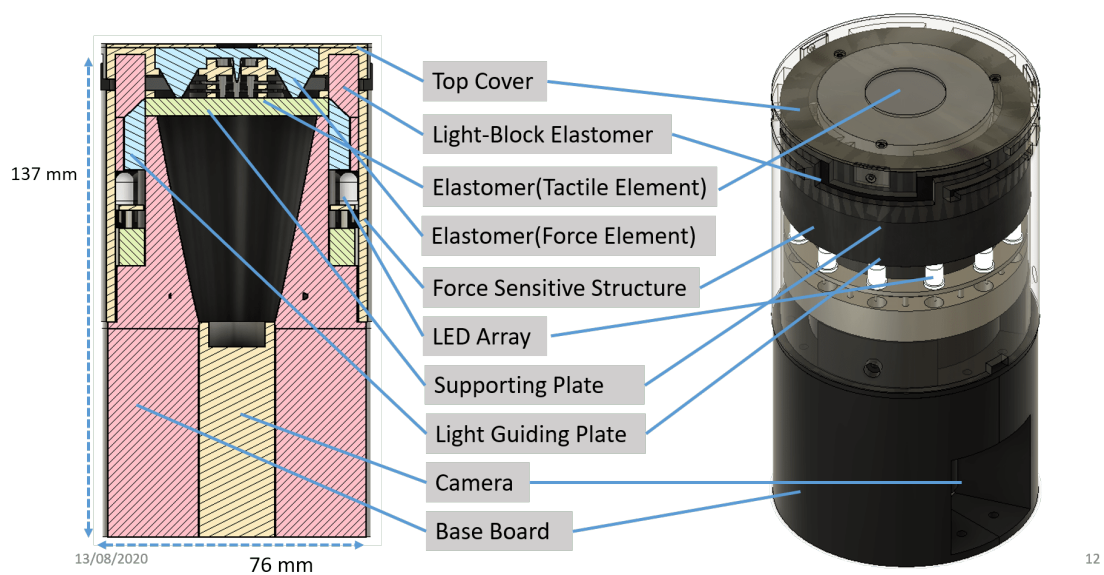


Figure 5.6: The design of the optical-based force and tactile sensor (CFTS1) where the left is the schematic design, and the right is the CAD view of the sensor. An elastomer and a force-sensitive structure are used within the sensor prototype.

5.3.1 Sensor Calibration and Evaluation

The working principle of the sensor is shown in Fig. 5.7. What is more, a calibration process is required for accurate measurement of the normal force in Z-direction. The calibration process aims to obtain a relationship between the output (in the form of activated pixels of the three

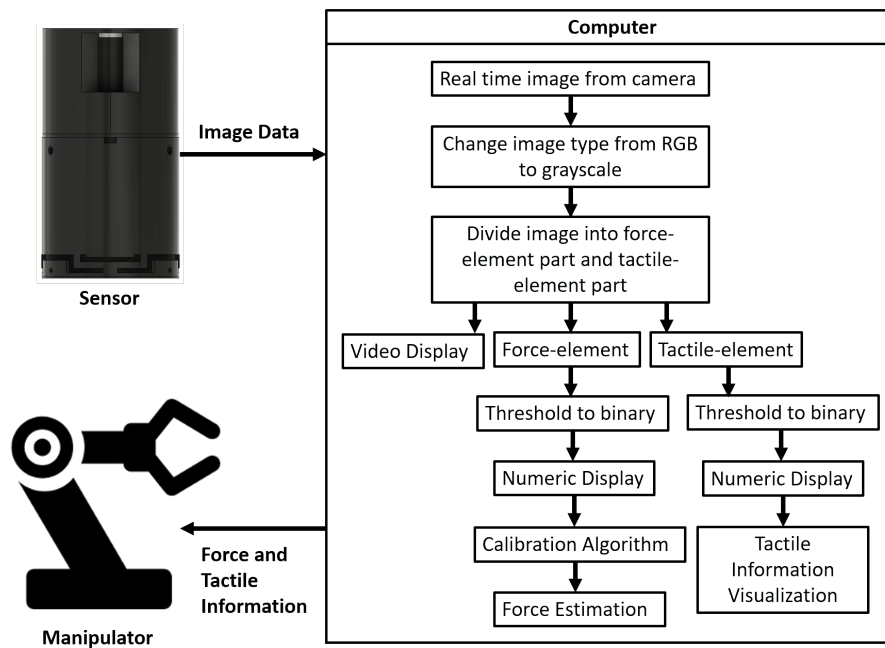


Figure 5.7: A flowchart of the proposed light intensity to force and tactile information sensing system. The system acquires the input video in 30 frames per second, and all the image computations can be processed in real-time.

force pins shown in Fig. 4.19(b)) and the normal force. A set of weights, from 10 N to 70 N with an increment of 5 N, is evenly applied on a plate above the sensor as the normal forces, as is shown in Fig. 5.8. The sensor saturates after the maximum force of 70 N is applied. The test is repeated ten times for each weight, and the relationship between the applied force and the average number of activated pixels for each force pin is shown in Fig. 5.9. A line is fitted to each response, and the coefficients of the linear fitting curves ($y = Ax + B$) are shown in Tab. 5.1. However, Pin 1 and Pin 3 do not really give a good linear response because of the fabrication error of both the elastomer and shell which are shown in Fig. 4.18(b), and the surface of the shell is not perfectly aligned to the elastomer surface, also the three force pins in Fig. 4.19(b)) are not at the exact same heights due to manufacturing errors.

Multiple linear regression (MLR) is applied to find the relationship between the number of activated pixels for each force pin. We assume that they are three independent variables, namely

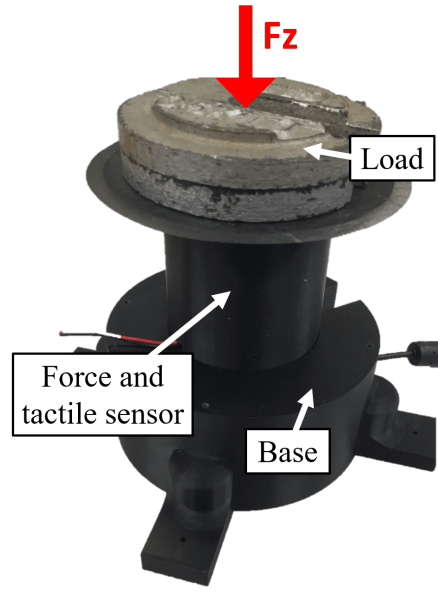


Figure 5.8: Experimental set up for the calibration of normal force F_z .

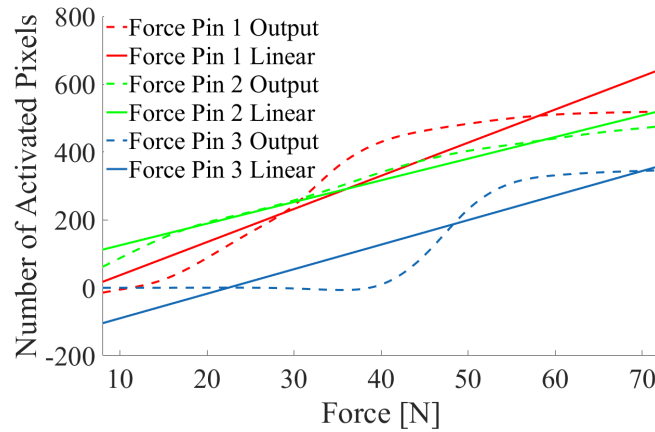


Figure 5.9: Characteristic curves of output activated pixels of force-element of the elastomer. We choose to use a linear fitting in order to fit the commonly-used linear regression in force sensor calibration. non-linear regression can be explored in future experiment.

s_1 , s_2 , s_3 , and the normal force F_z is the dependent variable. The obtained calibration curves are used to generate a 3×1 calibration matrix K . This matrix converts three numbers of activated pixels to one physical value of the normal force. By applying MLR, the matrix K is calculated

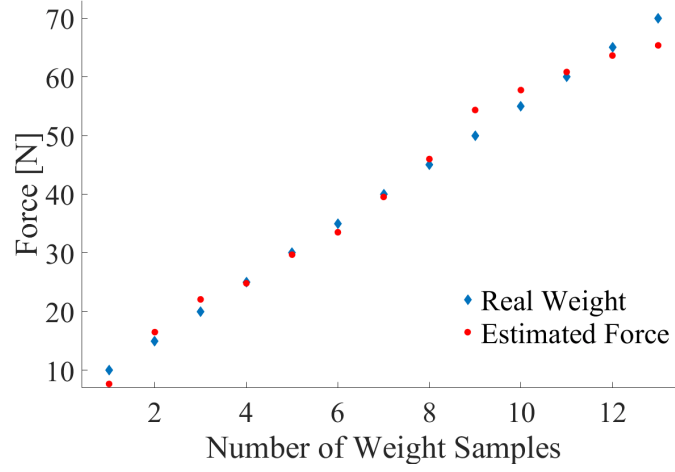


Figure 5.10: Static response of the sensor using weights for loading.

Table 5.1: Coefficient of Linear Fitting Curve

Sensor Element Number	Coefficient	
	A	B
1	9.764	-60.7
2	6.379	61.3
3	7.233	-162.3

as follows:

$$\begin{bmatrix} k_1 & k_2 & k_3 \end{bmatrix} \times \begin{bmatrix} s_1 \\ s_2 \\ s_3 \end{bmatrix} = \begin{bmatrix} F_z \end{bmatrix} \quad (5.1)$$

$$K = \begin{bmatrix} -0.0081 & 0.1375 & 0.0260 \end{bmatrix} \quad (5.2)$$

As shown above, the estimated normal force F_z can be obtained by multiplying the calculated

calibration matrix with the sensor activated pixels s_1 , s_2 and s_3 .

To evaluate the performance of the calibration method, weights are used to apply the increasing step-like force on the sensor gradually. Fig. 5.10 shows the sensor response for the weights ranging from 10 N to 70 N at increments of 5 N. We repeat the test ten times and the maximum error between the estimated and the ground-truth normal force values does not exceed 6.6%, and the root mean square error (RMSE) is 2.25 N.

5.3.2 Visualization of Tactile Information

As described above, the pressure distribution is displayed using the information from the activated pixels of the tactile pins. Fig. 5.11 shows the testing tools for tactile sensing and Fig. 5.12 shows a user interface for the display of the tactile information. The greyscale pressure colourmap is updated when an object comes into contact with the elastomer membrane. The magnitude of the pressure colourmap is calculated using the maximum applied pressure (number of activated pixels) as a reference. Therefore, when no force is applied, the initial colour is dark grey for all sections as the default value. To evaluate the tactile response, several shapes were tested. Firstly, we touch the side of the membrane with a sharp pin of 2 mm in diameter, and the result is shown in Fig. 5.13. It can be seen that the colour-magnitude of the pressure colourmap is updated, with white colour indicating no contact, and black corresponding to the highest pressure

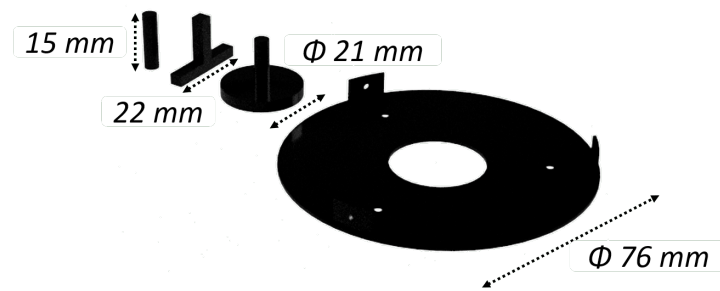


Figure 5.11: Three tools for tactile information tests with the reference of a sensor cap, one edge detection is tested by the left tool, section detection is tested by the middle tool, and non-uniform detection is tested by the right tool which has a non-uniform surface at the bottom.

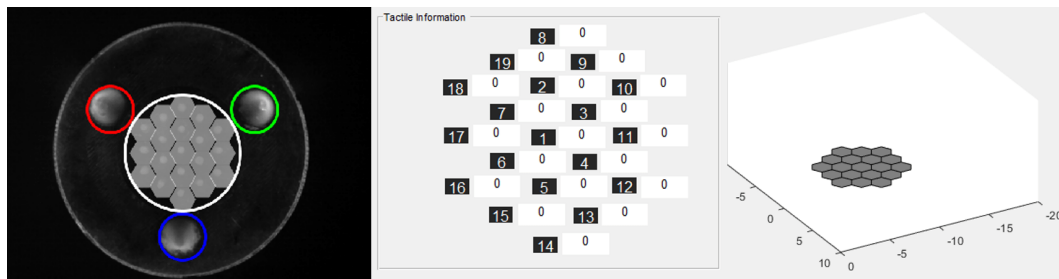


Figure 5.12: User display of the tactile information: No pressure is applied to the membrane. The left plot is the post-processing images of the input videos. Three force pins are highlighted with red, green and blue circles. The white circle in the middle indicates 19 tactile pins which are allocated in a honeycomb arrangement. The middle plot indicates the areas of activated pixels of each 19 tactile pins separately. The right plot shows the visualizations of the tactile information in the form of pressure distribution.

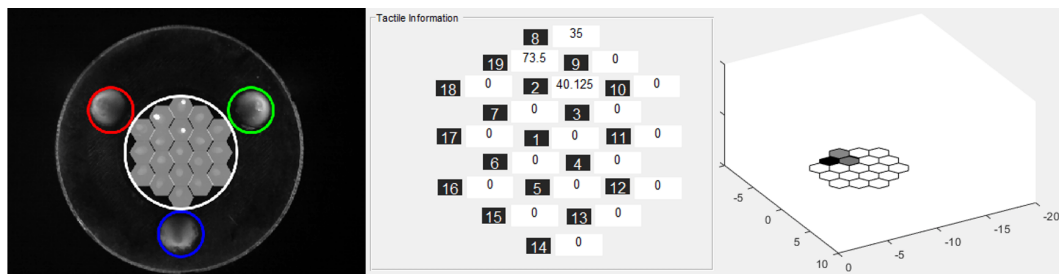


Figure 5.13: Applying pressure at one edge of the membrane.

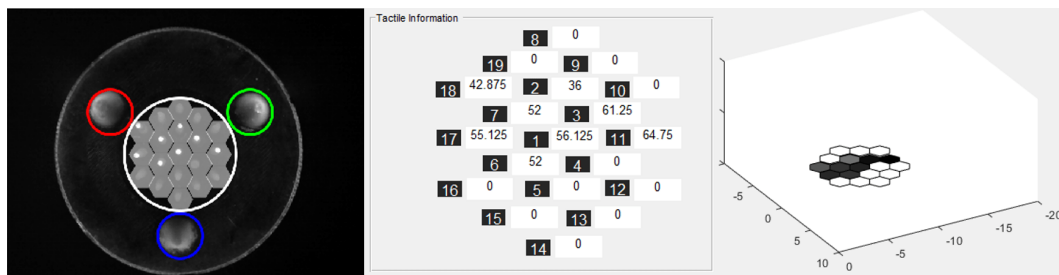


Figure 5.14: Applying pressure to the section of the membrane.

magnitude. The second tested shape is an edge with a width of 1.5 mm. It was pressed at the centre of the membrane. The result is shown in Fig. 5.14. Finally, the pressure was applied to the whole membrane surface. For this purpose, a finger was used in order to observe the irregular

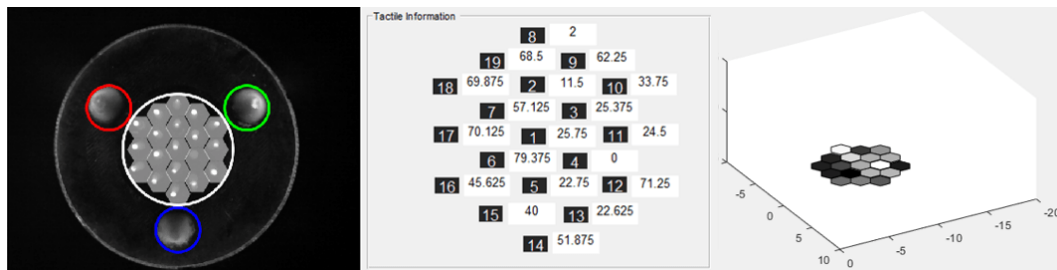


Figure 5.15: Applying non-uniform pressure to the whole membrane.

distribution of the pressure. The result is shown in Fig. 5.15.

5.3.3 Simultaneous Force and Tactile Sensing

In this additional experiment, our sensor is used to measure real-time force and tactile information by attaching a flat surfaced object to the end-effector of Franka Emika Panda robot arm, as is shown in Fig. 5.16 and Fig. 5.17. A normal force of 50 N was continuously applied to the membrane of the sensor via a Franka Emika Panda robot arm. In this experiment, our sensor has demonstrated its ability to measure the continuous and stable normal force over time, as well as

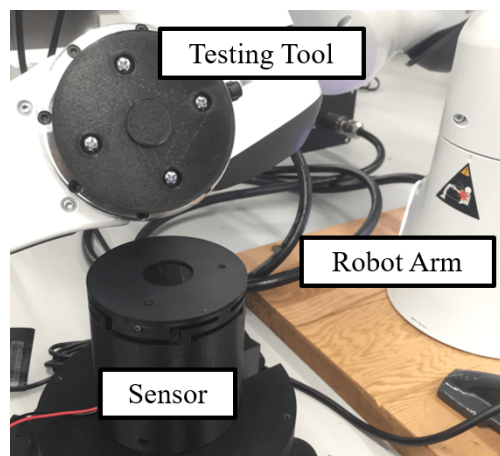


Figure 5.16: A scene of measuring both force information and tactile information using 3D printed object attached on a robot arm. A 3d printed object is attached on a Franka Emika Panda robot arm and then exerted on the top of the sensor.

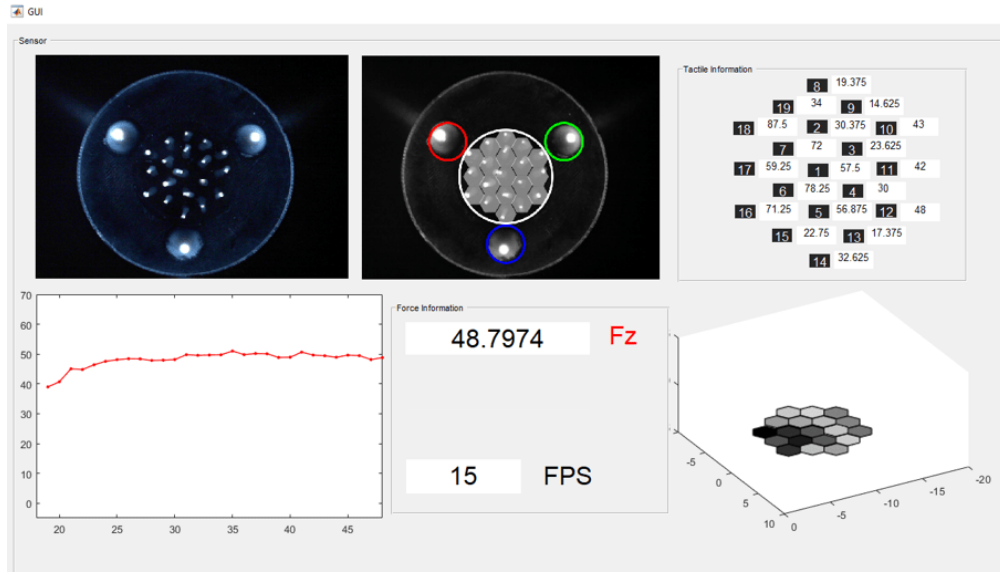


Figure 5.17: User interface illustrating the sensor can measure the real-time normal force (bottom left and middle section) and the pressure distribution (tactile information, shown in bottom right section) simultaneously.

to visualise the pressure distribution applied to the elastomer membrane.

5.3.4 Summary

In this work, we propose a novel design of a force and tactile sensor CFTS1 using a soft structure made from elastomeric material shaped into reflective pins to sense both force and tactile information. The fabrication procedure uses different types of silicone materials, and other required components are presented. Two sensor prototypes are presented. For the first sensor CFTS1, the experimental results demonstrate that the sensor can measure real-time normal forces over a range from 0N to 70 N. The pressure distribution can be visualised at the same time. In the proposed configuration, the sensor can only measure force along one dimension. However, theoretically three-degrees-of-freedom force components can be calculated for the measurement (for example, additional two moments in lateral directions, T_x and T_y) based on the force-sensitive shell design. In the future, we intend to build a customized calibration device using a commercial force sensor, as well as to apply deep learning methods for calibration. We also plan to

improve and formally assess the sensor characteristics. As for the second sensor CFTS2, the sensor uses an elastomer with transparent silicone to replace the reflective tactile pins, and we use the transparency of the silicone to detect the texture of the object.

5.4 F-TOUCH Sensor — Force and Tactile Optically Unified Coherent Haptics Sensor

The optical-based force and tactile sensor that is described above verifies the possibility of measuring both force and tactile information within one housing device with the use of an elastomer layer and an elastic structure. However, there is one issue with this sensor prototype, as mentioned in Sec. 4.5, namely that the sensing areas of the force and tactile information are separate, as shown in Fig. 4.25(a). The result of this is that force and tactile information cannot be effectively measured from a specific sensing area. Therefore, we further proposed an improved optical-based force and tactile sensor named F-TOUCH, as shown in Fig. 5.19, that also uses a combination of an elastomer layer and an elastic structure within a unique configuration so that the sensor can obtain both information at any location of the sensing medium.

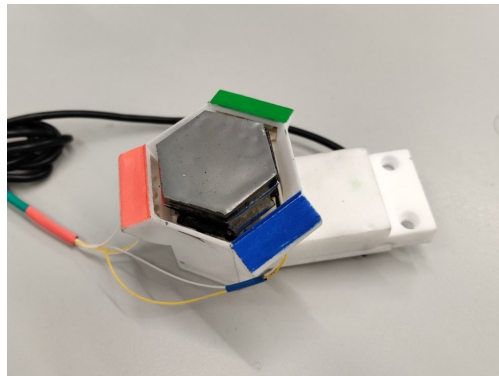


Figure 5.18: The manufactured prototype of the proposed F-TOUCH sensor. The sensor is connected via a USB webcam to capture the real-time image of the coated silicone surface, which is illuminated by RGB LED arrays within the sensor. An internal spring-mechanism structure with markers is used to measure force information.

The key contribution of the proposed F-TOUCH is the capability to concurrently and ef-

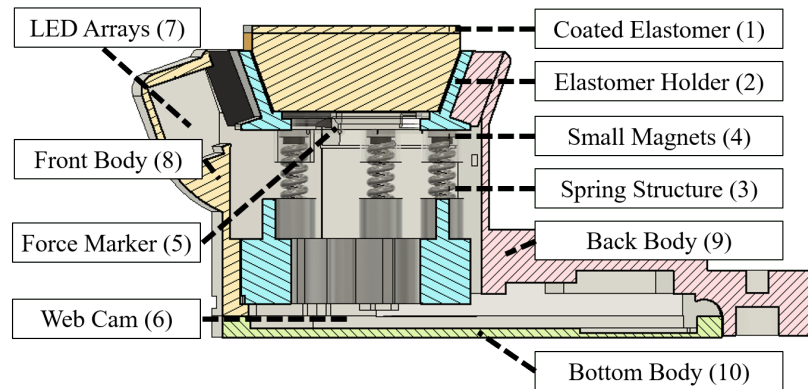


Figure 5.19: Schematic design of the proposed sensor. There are in total of 10 components that make up the device. Details of each component can be seen from Fig. 4.35.

fectively perceive dual modalities. In this sensor, a unitary force and tactile sensing capability is integrated within a single sensor housing, with the signal acquisition being performed by a single monocular camera acting as the transducer.

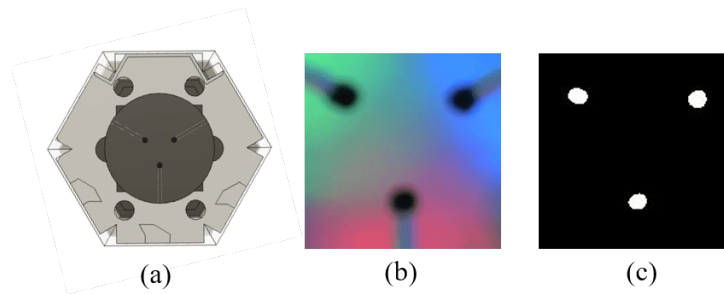


Figure 5.20: Extracting force markers from the tactile image. (a) Bottom view of the CAD spring-mechanism structure, where force markers are circularly attached beneath the coated elastomeric component. (b) The raw captured image from the camera. (c) The binary image after thresholding.

When the sensor is on, RGB lights are emitted from different directions to illuminate our sensing system (for both coated elastomer surface and black markers within the spring structure). When there is a contact occurring on the surface, the raw image is received by the camera at the bottom, as is shown in Fig. 5.20. The procedure of segmenting force information and tactile

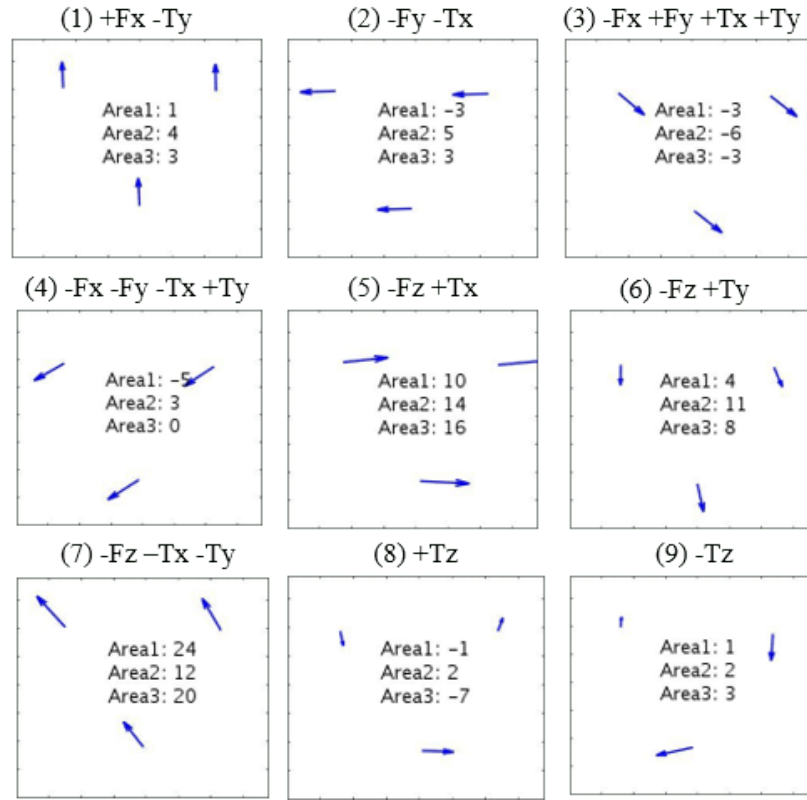


Figure 5.21: Responses of the F-TOUCH sensor under different force/torque loads. The sensor responses are in the form of depicting the motion of three marker centroids as a vector plot, together with the corresponding marker area changes. Each marker's movement vector is scaled for better comprehension of the motions. Nine scenarios of force/torque loading conditions are presented: (1) Shear force $+F_x$ and torque $-T_y$ are applied; (2) Shear force $-F_y$ and torque $-T_x$ are applied; (3) Shear force $-F_x +F_y$ and torque $+T_x +T_y$ are applied; (4) Shear force $-F_x -F_y$ and torque $-T_x +T_y$ are applied; (5) Normal force $-F_z$ and torque $+T_x$ are applied; (6) Normal force $-F_z$ and torque $+T_y$ are applied; (7) Normal force $-F_z$ and torque $-T_x -T_y$ are applied; (8) Torque $+T_z$ is applied; (9) Torque $-T_z$ is applied.

information within the raw image can be fairly simple: there is a distinct colour difference between the contact geometry (only red, green, blue colour can be seen) and the black marker, as shown in Fig. 5.20 (b). We firstly transfer the raw image into a greyscale image and then apply a gaussian filter. After the filtering, we apply a threshold to the filtered greyscale image to segment the marker areas from the background and then do a colour reverse, as is shown in

Fig. 5.20 (c).

As for tracking the markers, we calculate both the centroids positions and areas of each three markers based on the reverse binary image. When under an unloaded status, we record both the x,y coordinate values of the centroids ($x_1(0)$, $y_1(0)$, $x_2(0)$, $y_2(0)$, $x_3(0)$, $y_3(0)$) and areas ($a_1(0)$, $a_2(0)$, $a_3(0)$) of three markers within the binary image. When applying a contact force, we calculate the change of the x,y coordinate values of the centroids as well as the areas changes of each markers at each frame j , as $\Delta x_i(j) = x_i(j) - x_i(0)$, $\Delta y_i(j) = y_i(j) - y_i(0)$ and the areas $\Delta a_i(j) = a_i(j) - a_i(0)$. With the obtained values of variables Δx_1 , Δy_1 , Δa_1 , Δx_2 , Δy_2 , Δa_2 , Δx_3 , Δy_3 , Δa_3 from three markers, we can proceed to multi-axis force/torque calibration. Here, two calibration processes are introduced: the first one is the calibration for three-axis force, and the second one is for six-axis force and torques.

5.4.1 Three-Axis Forces Calibration and Evaluation

After the force-related information segmentation, a calibration process is needed for accurate measurement of forces along 3 axes, including normal force in Z-axis and shear forces in X and Y-axis. This process aims to obtain a relationship between the nine variables outputs of

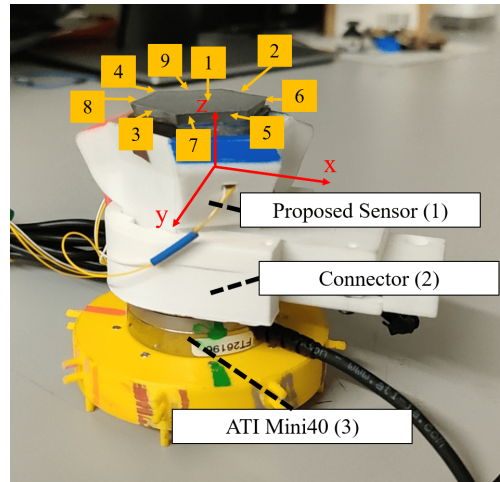


Figure 5.22: Experimental setup for calibration of the proposed three-axis forces. Nine force conditions are applied on the elastomer surface of the sensor.

our proposed sensing device (change of x,y coordinates of three markers' centroids and the corresponding area changes) and the sensor's input forces. To set up the experiment, we use a commercial force sensor (ATI Mini40 six-axis force/torque sensor) as the reference to precisely measure the ground-truth force values. Then we mount our sensor on the sensing surface of ATI Mini40 via a 3d printed connector. The connector is designed to fix with ATI Mini40 by bolts and firmly hold our proposed sensor.

Table 5.2: Applied Force Conditions for Three-Axis Calibration

Applied force	Condition	Applied force	Condition
1	$-F_z \pm F_x \pm F_y$	6	$+F_y -F_x$
2	$+F_y$	7	$-F_y -F_x$
3	$-F_y$	8	$-F_y +F_x$
4	$+F_x$	9	$+F_y +F_x$
5	$-F_x$		

We apply a variety of different force conditions directly on the touch medium of our proposed sensor with our hand applying different forces, as shown in Tab. 5.2 and Fig. 5.22. We merge the data acquisition of ATI Mini40 into our sensor's user interface so that we synchronize both readings from our sensor and the ATI F/T sensor. We record a set of ground truths force data of 8400 samples from ATI Mini40 and marker's centroids, and areas change readings from our sensor with 15 samples per second (due to the restriction of the camera frame rate). From the recorded data, the calibration matrix can be calculated using the Least Squares Regression method [129].

We assume that the nine-variables outputs of our sensor are independent, namely $\Delta x_1, \Delta y_1, \Delta a_1, \Delta x_2, \Delta y_2, \Delta a_2, \Delta x_3, \Delta y_3, \Delta a_3$, and the applied force F_x, F_y, F_z are dependent variables. We can generate a 3-by-9 calibration matrix K based on the 2000 sets of synchronised data from our sensor's input and the ATI F/T sensor's output. This matrix converts nine sensor readings to three physical values of forces. The calculated calibration matrix K is presented in 5.3 and 5.4.

$$\begin{bmatrix} k_{11} & k_{12} & k_{13} & k_{14} & k_{15} & k_{16} & k_{17} & k_{18} & k_{19} \\ k_{21} & k_{22} & k_{23} & k_{24} & k_{25} & k_{26} & k_{27} & k_{28} & k_{29} \\ k_{31} & k_{32} & k_{33} & k_{34} & k_{35} & k_{36} & k_{37} & k_{38} & k_{39} \end{bmatrix} \begin{bmatrix} \Delta x_1 \\ \Delta y_1 \\ \Delta a_1 \\ \Delta x_2 \\ \Delta y_2 \\ \Delta a_2 \\ \Delta x_3 \\ \Delta y_3 \\ \Delta a_3 \end{bmatrix} = \begin{bmatrix} F_x \\ F_y \\ F_z \end{bmatrix} \quad (5.3)$$

$$K = \begin{bmatrix} -9.3e^{-4} & -2.0e^{-3} & 4.5e^{-4} & 3.6e^{-3} & -1.9e^{-3} & -3.8e^{-4} & -2.0e^{-3} & 2.8e^{-4} & -1.8e^{-4} \\ 6.0e^{-3} & -2.9e^{-3} & -1.5e^{-3} & -3.5e^{-3} & 4.1e^{-3} & -1.2e^{-3} & 1.3e^{-3} & -2.0e^{-3} & -2.2e^{-3} \\ 3.0e^{-2} & -3.6e^{-2} & 5.5e^{-3} & 5.7e^{-3} & 6.3e^{-2} & -1.9e^{-3} & -3.5e^{-2} & -2.8e^{-2} & -4.2e^{-4} \end{bmatrix} \quad (5.4)$$

Table 5.3: Three-Axis Forces Measurement Accuracy of the Proposed Sensor

Force	Measurement range	Maximum error	RMSE
F _x	+/- 1 N	11.97%	0.04 N
F _y	+/- 1 N	15.93%	0.05 N
F _z	0 - 8 N	8.77%	0.13 N

As presented above, the estimated three-axis force F_x F_y F_z can be obtained by multiplying the calibration matrix K with the nine outputs of our sensor. To evaluate the calibration matrix, external force components are applied on the membrane of our sensor under two force conditions (apply a shear force to the elastomer with almost zero normal force and apply normal force plus shear force to the elastomer). We compare our sensor force reading with the ground-truth values from ATI Mini40, as is shown in Fig. 5.23 and Tab. 5.3. The root mean square errors (RMSE)

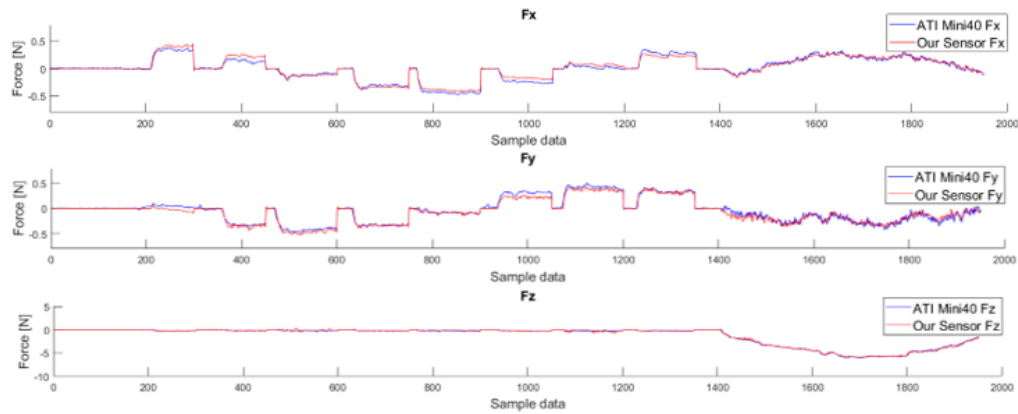


Figure 5.23: Three-axis force comparison between ATI Mini40 sensor and our proposed sensor. The first stage is applying a pure shear force to the elastomer (normal force is tiny and almost to be zero, this can be achieved by the spring-structure) and the second stage is applying normal force plus shear force.

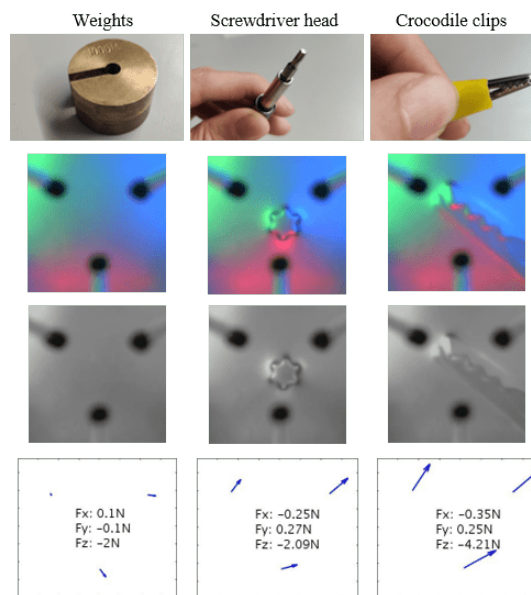


Figure 5.24: Three different testing objects are applied upon our proposed sensor: The first column are weights and the corresponding captured raw image, filtered greyscale image and the force measurement; In the second and third column, we applied screwdriver head and crocodile clips with shear and normal forces.

of F_x F_y F_z are 0.04 N, 0.05 N, 0.13 N respectively.

To explore our proposed sensor's response to different contact, we use different testing objects with different surface shapes. Some of the testing results (including the testing objects, raw capture, filtered greyscale image and marker motions) are shown in Fig. 5.24 where we apply different force condition with the object on our sensor. The proposed sensor has demonstrated its ability to measure both three-axis force values and perceive the contact object geometry at the same time within processing one camera capture.

5.4.2 Six-Axis Forces Calibration and Evaluation

Based on the three-axis calibration method described above, we then further develop a six-axis calibration with the use of a different setup.

As introduced above, the sensor calibration is the process of determining the relationship between the sensor's output variables to the six-axis force and torque input components (F_x F_y F_z T_x T_y T_z). There are various studies [154] on force calibration of vision-based tactile sensors including those using convolutional neural networks (CNNs), that are useful when dealing with images [176, 154]. However, in our case, there are two sensing modalities (force and tactile) presented in each image (for instance, in the force measurement, if we trained with the raw images, the force measurement using CNNs could be influenced by the contact geometry [176], also a great number of data that cover all situations are needed for the training process); hence we cannot use the exact same method as above. Instead, we obtain the force-related numerical values (markers' centriod displacements and area changes) from the image and, given the linearity of the sensor's spring mechanism structure, we apply a conventional force sensor calibration method [16, 108]. The aim is to calculate the calibration matrix K , where the regression coefficients matrix is used to convert the output variables to force and moment loading data. A six-by-nine calibration matrix multiplies the nine-by-one sensor output vector to give the decoupled output force/torque values.

$$\begin{bmatrix} k_{11} & k_{12} & k_{13} & k_{14} & k_{15} & k_{16} & k_{17} & k_{18} & k_{19} \\ k_{21} & k_{22} & k_{23} & k_{24} & k_{25} & k_{26} & k_{27} & k_{28} & k_{29} \\ k_{31} & k_{32} & k_{33} & k_{34} & k_{35} & k_{36} & k_{37} & k_{38} & k_{39} \\ k_{41} & k_{42} & k_{43} & k_{44} & k_{45} & k_{46} & k_{47} & k_{48} & k_{49} \\ k_{51} & k_{52} & k_{53} & k_{54} & k_{55} & k_{56} & k_{57} & k_{58} & k_{59} \\ k_{61} & k_{62} & k_{63} & k_{64} & k_{65} & k_{66} & k_{67} & k_{68} & k_{69} \end{bmatrix} \begin{bmatrix} \Delta x_1 \\ \Delta y_1 \\ \Delta a_1 \\ \Delta x_2 \\ \Delta y_2 \\ \Delta a_2 \\ \Delta x_3 \\ \Delta y_3 \\ \Delta a_3 \end{bmatrix} = \begin{bmatrix} F_x \\ F_y \\ F_z \\ T_x \\ T_y \\ T_z \end{bmatrix} \quad (5.5)$$

Table 5.4: Force/Torque Exertion Conditions On The Sensor Tip

Numbering	F/T Condition	Numbering	F/T Condition
1	$-F_z - T_y$	10	$F_x F_y T_x - T_y$
2	$-F_z - T_x - T_y$	11	$F_x - T_y$
3	$-F_z - T_x$	12	$F_x - F_y - T_x - T_y$
4	$-F_z - T_x T_y$	13	$-F_y - T_x$
5	$-F_z T_y$	14	$-F_x - F_y - T_x T_y$
6	$-F_z T_x T_y$	15	$-F_x T_y$
7	$-F_z T_x$	16	$-F_x F_y T_x T_y$
8	$-F_z T_x - T_y$	17	$\pm T_z$
9	$F_y T_x$		

We set out to calibrate the six-axis force and torque component observations of the improved optical-based force and tactile sensor against a high-grade commercial six-axis force/torque sensor (ATI® Mini40 F/T sensor) as a source of reference values. As the sensing medium of the proposed sensor is made of silicone elastomer which is a soft material, it is impossible to directly mount the ATI® sensor atop the elastomer surface. Neither could we directly place the ATI® sensor underneath our sensor as the torque readings of both sensors would diverge due to the intervening distance between their respective contact surfaces. In order to fulfil the requirements

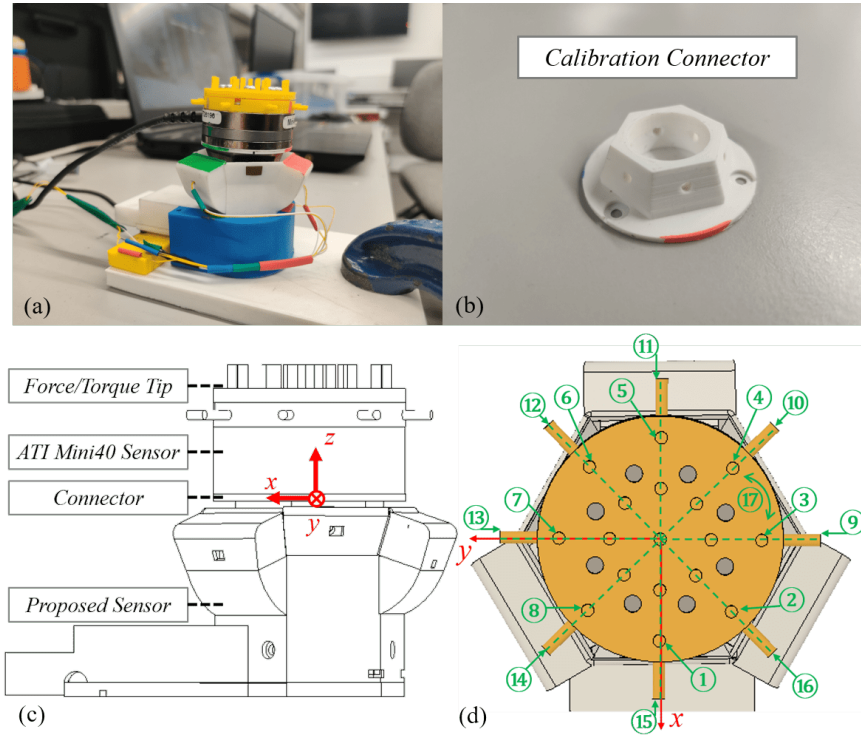


Figure 5.25: Calibration of the F-TOUCH sensor, with the aid of a commercial six-axis force/torque sensor ATI® Mini40 and a specially designed 3D-printed calibration connector. (a) Experimental setup for six-axis force/torque calibration. (b) 3D-printed calibration connector (made of ABS material) that is used to firmly attach our sensor with the ATI force/torque sensor for force calibration. (c) CAD view of the calibration setup. (d) CAD top-down view of the calibration device for applying different force and torque conditions to both ATI® Mini40 sensor (regarded as the ground truth) and our sensor. Seventeen loading conditions (see Tab. 5.4) are applied during the calibration process.

for calibration, a specially designed calibration interface is proposed, as shown in Fig. 5.25. The commercialized ATI® Mini40 sensor provides the ground-truth force and torque magnitudes, while a force/torque cap (3D-printed using polylactic acid (PLA)) is placed on top of it, and a specially designed connector (3D-printed using acrylonitrile butadiene styrene (ABS)) is attached to its underside. The reverse side of the connector attaches to the elastomer holder of the proposed sensor. The force/torque cap enables different forces and torques to be applied to both sensors through the same plane, as shown in Tab. 5.4.

The connector (shown in Fig. 5.25 (b)) is designed to act as ‘connective tissue’ between the two sensors. During the calibration process, we replaced the original elastomer component with the specially designed connector, both having the same height. We deliberately chose the connector to be of white colour so that the final binary images of the illuminated markers would be as closely matched as possible while using either the elastomer or the connector.

The nine output variables returned by the sensor captured image data are synchronized at a sampling rate of 30 samples per second with the six-axis force/torque readings from the ATI® Mini 40 sensor under seventeen different loading conditions. We manually exert the force and torque loads on the force/torque cap, as shown in Fig. 5.25 (d). The calibration matrix K is then calculated with the least squares method (LSM).

$$K = \begin{bmatrix} -3.9e^{-4} & 1.0e^{-2} & -3.5e^{-4} & 2.0e^{-4} & -8.6e^{-3} & -3.5e^{-4} & -8.1e^{-5} & 3.4e^{-3} & -1.7e^{-4} \\ -2.8e^{-4} & -3.2e^{-3} & -3.8e^{-4} & 3.0e^{-3} & 2.5e^{-3} & 8.5e^{-5} & 8.3e^{-4} & -6.9e^{-6} & 8.5e^{-5} \\ 1.6e^{-2} & -6.0e^{-2} & -3.9e^{-3} & -3.1e^{-4} & 1.0e^{-1} & -1.4e^{-4} & -1.5e^{-2} & -4.4e^{-2} & 2.6e^{-4} \\ 5.6e^{-2} & 8.4e^{-3} & -6.5e^{-2} & -6.2e^{-3} & 3.6e^{-2} & -1.9e^{-2} & 2.3e^{-2} & -4.6e^{-2} & -2.1e^{-2} \\ -2.0e^{-1} & 7.6e^{-1} & 1.9e^{-2} & 2.8e^{-2} & -1.5e^0 & -6.8e^{-3} & 1.7e^{-1} & 6.6e^{-1} & -3.5e^{-2} \\ -3.8e^{-2} & -1.6e^{-1} & -1.5e^{-2} & 7.3e^{-2} & 4.4e^{-2} & -7.4e^{-3} & -3.8e^{-2} & 1.2e^{-1} & -9.5e^{-3} \end{bmatrix} \quad (5.6)$$

Fig. 5.26 compares the six-axis force/torque performance between the proposed sensor and the ATI® Mini40 sensor when the connector is used. Due to the use of a camera, the response time of our sensor is 30 Hz, or 33 ms. The RMSE (root mean square error), the corresponding normalized RMSE and the coefficient of determination of fit, R^2 , of F/T components from both our sensor and GelSight sensor are listed in Tab. 5.5. It can be seen from the table that our sensor exhibits superior force and torque performance over GelSight when comparing with the ground truth measured by the ATI F/T sensor.

As the proposed sensor can also perceive the geometry of the contact object’s surface, we

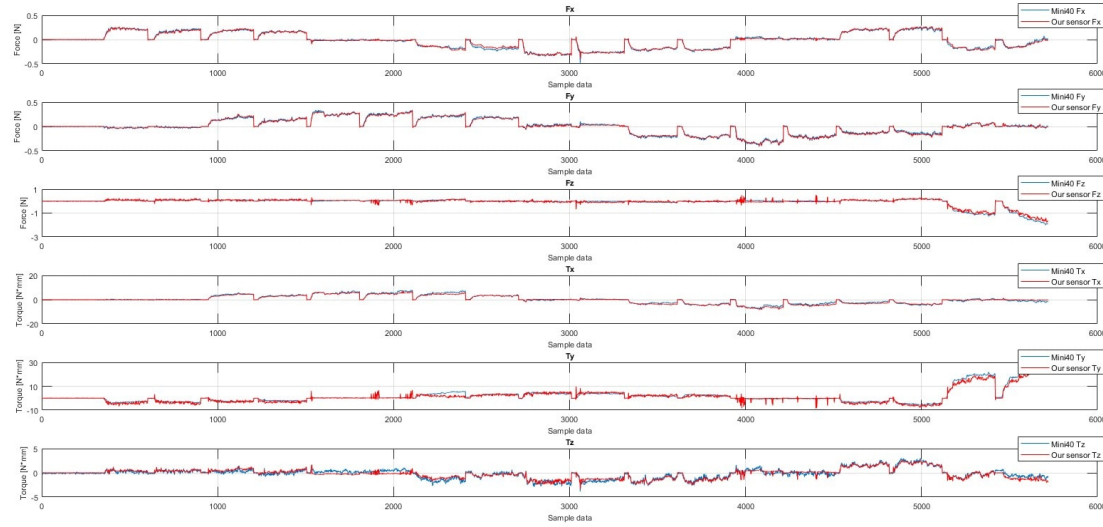


Figure 5.26: Comparison of six-axis force/torque performance between ATI® Mini40 sensor and our proposed sensor using a calibration connector.

Table 5.5: Proposed Sensor's Force/Torque Calibration Accuracy

F/T	Range of our sensor	RMSE, normalized RMSE and R-squared in our sensor	RMSE, normalized RMSE and R-squared in GelSight sensor
Fx	+/- 1 N	0.018 N (1.8%) $R^2=0.99$	0.187 N (4.7%) $R^2=0.94$
Fy	+/- 1 N	0.016 N (1.6%) $R^2=0.99$	0.162 N (4.0%) $R^2=0.93$
Fz	0 - 8 N	0.094 N (1.2%) $R^2=0.94$	0.668 N (3.3%) $R^2=0.97$
Tx	+/- 20 N · mm	0.657 N · mm (3.3%) $R^2=0.96$	-
Ty	+/- 20 N · mm	1.566 N · mm (7.8%) $R^2=0.94$	-
Tz	+/- 20 N · mm	0.407 N · mm (2.0%) $R^2=0.85$	3.72 N · mm (2.5%) $R^2=0.84$

further explore the proposed sensor's performance by investigating different contact conditions with objects having different surface geometries, as shown in Fig. 5.27 below, where raw tactile images and six-axis force/torque measurements are presented. In view of the above, we feel justified in concluding that the proposed improved optical-based force and tactile sensor has the capability concurrently to perceive two modalities: six-axis force/torque components measurement and perception of contact surface geometry, all by processing a single captured image.

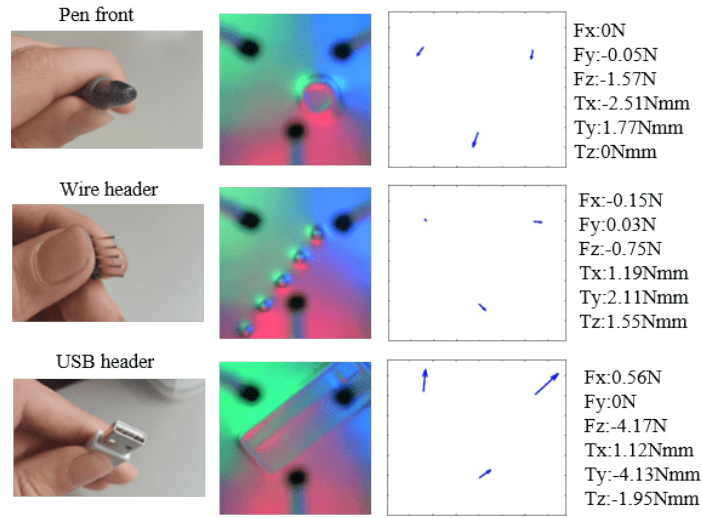


Figure 5.27: The improved optical-based force and tactile sensor's performance across dual modalities (six-axis force/torque information and contact object's surface geometry). Three different objects are pressed against our sensor's membrane surface. The first row presents the sensor performance when a pen's front tip is tested; the second row is testing with a wire header; the third row is testing with a USB header.

5.4.3 Summary

In this work, we have introduced a unified vision-based sensor (F-TOUCH), that can concurrently sense two modalities: six-axis force/torque components and tactile information (in the form of geometry and texture perception) using a single image capturing device. In other words, the proposed sensor can be regarded as a unitary device combining the capabilities of both a force sensor and a tactile sensor. The proposed sensor is designed to fit robot grippers and takes inspiration from the fingertip GelSight tactile sensor. The novelty and original contribution of the work are in the use of a coated transparent elastomer layer combined with spring-based deformable structural elements to measure tactile and 6-axis force information within a single sensor housing. We are able to extract translational and rotational force information (based on the status of the markers integrated with the deformable structural elements) as well as tactile information (based on the deformation of the illuminated elastomer surface) in real-time. Moreover, we have designed a specific implement to assist with the six-axis force/torque calibration

of the F-TOUCH_{3.2} sensor. Our experiments show an accuracy of force/torque measurements (F_x , F_y , F_z , T_x , T_y , T_z with RMSE of 0.018 N, 0.016 N, 0.094 N, $0.657\text{ N} \cdot \text{mm}$, $1.566\text{ N} \cdot \text{mm}$ and $0.407\text{ N} \cdot \text{mm}$ respectively) that is superior to the GelSight sensor's force/torque sensing performance.

Chapter 6

Conclusion and Future Work

This chapter presents a summary of the main contributions that have been achieved within the thesis, that are:

1. Dual-modal sensor for force and tactile sensing in one sensor structure completed
2. The miniaturisation of dual-modality force/tactile sensor for integration with robot arm end effector realised
3. Concurrent and real-time force and tactile sensing using a single camera sensor achieved
4. Extension from normal force measurement to three degrees of freedom forces measurement, to six degrees of freedom forces/torques measurement
5. Experimental study conducted to validate the approach

Several sensor prototypes have been developed and tested to validate the above contributions.

6.1 Summary

It is well accepted that the acquisition of high-quality force and tactile sensor signals during a mechanical interaction between a robot and an object provides the opportunity to largely enhance the handling and manipulation capability of the robotic system. Currently, there is a clear distinction between a typical force sensor and a tactile sensor. Multi-axis force sensors are developed to measure forces and torques that occur in more than one direction within the robotic force and tactile sensing system. Force sensors usually include a mechanical structure, and by sensing the deformation of the structure under external load, multi-axis force/torque (F/T) quantities can be measured along with different directions. Chapter 2 presented an overview of current popular sensing methods that include strain sensing technology (semiconductor strain gauges, capacitive strain gauging, fibre Bragg gratings, electrical resistance strain gauges), and optical-based sensing technology. Mechanical structures include cross-beam structure, Stewart platform, cantilever structure and spring structure. There has been a surge of research interest in tactile sensor development in recent decades. Different technologies have been explored to acquire tactile information that includes mechanical stimulus detection of contact, slip, pressure, and geometry. Typical technologies are electrical-based (piezoresistive, piezoelectric, capacitive, and magnetic) and optical-based. To conclude, force sensors can only measure touchpoint multi-axis force/torque components without tactile perception (for example geometry or pressure distribution), while tactile sensors can perceive tactile information but cannot precisely measure multi-axis F/T components.

Our contribution in this thesis is to integrate the capabilities of both a force sensor and a tactile sensor into one sensor structure which uses a combination of an elastomer layer and an elastic structure (as shown in Fig. 3.3). The sensing principle is based on an optical method that uses a single vision transducer (a camera) to sense both force and tactile modalities according to the deformation of the elastic structure and elastomer layer, as described in Chapter 3.

The sensor prototypes presented in Chapter 4 follow the same sensing methodology that is introduced in Chapter 3. ICFTS (Initial Camera-based Force/Tactile Sensor) is presented with

finite element analysis (FEA) of both the elastomer layer and the elastic structure. Then CTS (Camera-based Tactile Sensor) that uses an elastomer layer with reflective feet and an elastic structure with cantilever structure is presented. We improved on this sensor which can only detect pressure, by developing CFTS1 (Camera-based Force/Tactile Sensor) with a different elastomer layer component which can simultaneously measure the normal force and the pressure distribution in real-time. CFTS was further improved on by developing the F-TOUCH (Force and Tactile Optically Unified Coherent Haptics) sensor which use a combination of a coated transparent elastomer layer and a spring-mechanism structure to measure multi-axis force/torque information and perceive the contact geometry information at the same time. F-TOUCH resolved the issues of the CFTS design, namely its separate force and tactile sensing areas. In addition, the size was also drastically reduced.

Chapter 5 shows the experimental results of the prototypes that are introduced in Chapter 4. It is noted that the measurement of force/torque components using an elastomer-based tactile sensor is complicated. In Sec. 5.4, we have developed a force and tactile sensor architecture that integrates a coated transparent silicone elastomer with a six-degree-of-freedom spring-mechanism force structure. Tracking a trio of markers within the force structure, using a conventional force sensor calibration method, and a specially designed connector and commercial force/torque sensor (ATI® Mini40 sensor), allows six-axis force/torque components to be extracted, calibrated and measured. Moreover, the deformation of the illuminated elastomer surface reflects the contact surface geometry in the same image capture containing the force information. Thus observation data for the two modalities can be acquired at the same time with an integrated force and tactile sensing device. In our experiments, the positions of marker centroids together with marker area changes were shown to effectively represent the net normal force, shear force and torque. With the aid of a commercial F/T sensor and a specially designed connector attached to our sensor, a 6-by-9 calibration matrix was computed using the least squares regression method. However, there still remain deviations between the estimated force/torque and ground truth (from the ATI® Mini40 sensor). A plausible explanation for the discrepancy

may be that since we use both an elastomer component and springs in the sensor structure, hysteresis will inevitably creep in due to the responsiveness of these materials. Thus, the accuracy of the calibration matrix may be affected. Moreover, using a high-quality camera with a higher input rate can reduce image noise. These noises can also be improved with a more advanced filtering algorithm. There is always a trade-off between image quality and sensor response rate.

6.2 Future Work and Directions

The proposed optical-based force and tactile sensing method has promising applications in the field of robotic manipulations, especially in grasping. An outline of potential directions for future work on this optical-based force and tactile sensor is listed as follows.

- **Reduction of sensor size**

The current sensor can be further miniaturised as it is still relatively large (it is designed for a gripper end) when compared with a human or robot finger. To further reduce the sensor prototype size, a smaller camera can be used (however, the image quality can be reduced), and the illumination system shall be modified to save more space. Also, it is possible to fabricate smaller elastomer layer with small 3D printed mould. The DIGIT sensor [86] can be a good reference to move forwards.

- **Integration of dense markers for local force measurement**

Based on current F-TOUCH sensor, we also plan to integrate dense markers on the membrane surface of the elastomer (as GelSight sensor) for local force measurement. Therefore, the new sensor can have additional functionalities of local stress measurement and slip detection.

- **Hardness perception**

As the current optical-based force and tactile sensor can obtain both multi-axis force quantity and contact geometry information at the same time, it is possible to mount the sensor to an end-effector to conduct active sensing, for example, estimating contact object proper-

ties such as hardness. Objects with different hardness can produce a different tactile image (different depth information) when the same forces are exerted on them. Furthermore, a soft object can cause more deformation compared with the stiff one giving the same force condition. Therefore, by observing and calculating the ratio between the force value and the depth value (the depth value can be calculated from the colour intensity of the tactile image), it is possible to distinguish between soft objects and stiff objects.

- **Slip detection**

Slip detection can also be achieved by observing the changes of both the force values and the tactile image. When a slip occurs, there will be an apparent change between normal and shear forces (there shall be an increase of the ratio between the shear force over the normal force). At the same time, we can also observe a displacement of the object within the tactile image due to the slip. Therefore, we can combine the calculations of the force values and the detection of the object displacement to detect the slip effectively.

- **Object shape recognition**

The proposed force and tactile sensor can also be applied to detect the shape of an object if mounted on a robot arm. Since there is a six-degree-of-freedom spring mechanism structure within the sensor, it is possible to estimate the spatial pose of the sensor's contact surface (the rigid acrylic board surface) with the use of vision technique upon the markers. With the obtained pose and force information, a robot arm can be controlled to adjust the sensor's pose to be consistently at a specific condition (for example, a steady pose) when touching an unknown object. Therefore, we can track the pose of the end of the robot arm to recognise the object's shape while filling the shape with textures that are acquired from the sensor's tactile images.

References

- [1] Allegro hand profiles. <http://wonikrobotics.com/Allegro-Hand.htm>.
- [2] Ati multi-axis force/torque sensors profiles. <https://www.ati-ia.com>.
- [3] Force/torque sensors expand robotic capabilities. https://www.photonics.com/Articles/Force_Torque_Sensors_Expand_Robotic_Capabilities/a63234.
- [4] Hex force/torque sensor profiles. <https://www.universal-robots.com/plus/urplus-components/accessories/hex-forcetorque-sensing-package/>.
- [5] Introduction to load cell profiles. <https://www.omega.co.uk/prodinfo/load-cells.html>.
- [6] Introduction to strain gauge profiles. <https://www.omega.co.uk/prodinfo/straingauges.html>.
- [7] Optoforce 3d-force sensor profiles. <https://optoforce.com/3d-force-sensor-omd>.
- [8] Pressure profile systems inc., robotouch — overview. <http://www.pressureprofile.com/products-robotouch>.
- [9] Rg2 gripper profiles. <https://www.universal-robots.com/plus/urplus-components/handling-grippers/rg2-gripper/>.
- [10] Shadow dexterous hand profiles. <https://www.shadowrobot.com/products/dexterous-hand/>.

- [11] Understanding pressure sensor accuracy. <https://www.dwyer-inst.com/articles/industry/powderbulk/understanding-pressure-sensor-accuracy/understanding-pressure-sensor-accuracy.cfm#:~:text=Hysteresis%20is%20the%20maximum%20difference,a%20full%20span%20pressure%20cycle.>
- [12] Universal robot arm profiles. [https://www.universal-robots.com/products/ur5-robot/.](https://www.universal-robots.com/products/ur5-robot/)
- [13] A. C. Abad and A. Ranasinghe. Visuotactile sensors with emphasis on gelsight sensor: A review. *IEEE Sensors Journal*, 2020.
- [14] T. Abe, H. Nakaji, and R. Nakamura. Development of the bending mechanism for forceps with least-incision transformable end-effector mechanism for endoscopic surgery: Development of the operating interface and in vivo experiment. In *2012 4th IEEE RAS & EMBS International Conference on Biomedical Robotics and Biomechatronics (BioRob)*, pages 919–923. IEEE, 2012.
- [15] O. Al-Mai, M. Ahmadi, and J. Albert. A compliant 3-axis fiber-optic force sensor for biomechanical measurement. *IEEE Sensors Journal*, 17(20):6549–6557, 2017.
- [16] O. Al-Mai, M. Ahmadi, and J. Albert. Design, development and calibration of a lightweight, compliant six-axis optical force/torque sensor. *IEEE Sensors Journal*, 18(17):7005–7014, 2018.
- [17] A. Alfadhel, M. A. Khan, S. Cardoso, D. Leitao, and J. Kosel. A magnetoresistive tactile sensor for harsh environment applications. *Sensors*, 16(5):650, 2016.
- [18] D. Arciniegas, M. A. Herrera, K. Táutiva, L. M. Bermudez, J. S. Castellanos, and J. Angulo. Automation process modeling of a electric cars production line through petri nets and grafcet. In *2017 IEEE 3rd Colombian Conference on Automatic Control (CCAC)*, pages 1–6. IEEE, 2017.

- [19] K. Bae, S. Pyo, and J. Kim. Crosstalk-free mesh-embedded tactile sensor array with electrically isolated sensing cells. In *2020 IEEE 33rd International Conference on Micro Electro Mechanical Systems (MEMS)*, pages 673–676. IEEE, 2020.
- [20] S. Begej. Planar and finger-shaped optical tactile sensors for robotic applications. *IEEE Journal on Robotics and Automation*, 4(5):472–484, 1988.
- [21] R. Bekhti, V. Duchaine, and P. Cardou. Miniature capacitive three-axis force sensor. In *2014 IEEE/RSJ International Conference on Intelligent Robots and Systems*, pages 3939–3946. IEEE, 2014.
- [22] P. J. Berkelman, L. L. Whitcomb, R. H. Taylor, and P. Jensen. A miniature microsurgical instrument tip force sensor for enhanced force feedback during robot-assisted manipulation. *IEEE Transactions on Robotics and Automation*, 19(5):917–921, 2003.
- [23] S. Bhavikatti, R. Ranganath, and A. Ghosal. A near-singular, flexure jointed, moment sensitive stewart platform based fore-torque sensor. In *13th National Conference on Mechanisms and Machines*, 2007.
- [24] A. Bicchi and V. Kumar. Robotic grasping and contact: A review. In *Proceedings 2000 ICRA. Millennium Conference. IEEE International Conference on Robotics and Automation. Symposia Proceedings (Cat. No. 00CH37065)*, volume 1, pages 348–353. IEEE, 2000.
- [25] L. Bohan, W. Xiaoliang, L. Shan, L. Junqin, and Z. Guangshang. Design and analysis of a novel miniature two-axis force sensor. In *2019 2nd World Conference on Mechanical Engineering and Intelligent Manufacturing (WCMEIM)*, pages 328–334. IEEE, 2019.
- [26] E. Bosman, B. Van Hoe, J. Missinne, G. Van Steenberge, S. Kalathimekkad, and P. Van Daele. Unobtrusive packaging of optoelectronic devices for optical tactile and shear sensors. In *2011 Fifth International Conference on Sensing Technology*, pages 504–509. IEEE, 2011.
- [27] D. G. Caldwell, G. A. Medrano-Cerda, and C. J. Bowler. Investigation of bipedal robot

- locomotion using pneumatic muscle actuators. In *Proceedings of International Conference on Robotics and Automation*, volume 1, pages 799–804. IEEE, 1997.
- [28] P. Cantillon-Murphy, M. Ryou, S. N. Shaikh, D. Azagury, M. Ryan, C. C. Thompson, and J. H. Lang. A magnetic retrieval system for stents in the pancreaticobiliary tree. *IEEE Transactions on Biomedical Engineering*, 57(8):2018–2025, 2010.
- [29] M. G. Catalano, G. Grioli, E. Farnioli, A. Serio, C. Piazza, and A. Bicchi. Adaptive synergies for the design and control of the pisa/iit soft hand. *The International Journal of Robotics Research*, 33(5):768–782, 2014.
- [30] L.-P. Chao and K.-T. Chen. Shape optimal design and force sensitivity evaluation of six-axis force sensors. *Sensors and Actuators A: Physical*, 63(2):105–112, 1997.
- [31] L.-P. Chao and C.-Y. Yin. The six-component force sensor for measuring the loading of the feet in locomotion. *Materials & design*, 20(5):237–244, 1999.
- [32] M. T. Ciocarlie and P. K. Allen. Hand posture subspaces for dexterous robotic grasping. *The International Journal of Robotics Research*, 28(7):851–867, 2009.
- [33] P. Cosseddu, A. Bonfiglio, R. Neelgund, and H. W. Tyrer. Arrays of pressure sensors based on organic field effect: A new perspective for non invasive monitoring. In *2009 Annual International Conference of the IEEE Engineering in Medicine and Biology Society*, pages 6151–6154. IEEE, 2009.
- [34] M. R. Cutkosky, R. D. Howe, and W. R. Provancher. Force and tactile sensors. *Springer Handbook of Robotics*, 100:455–476, 2008.
- [35] R. S. Dahiya, G. Metta, M. Valle, and G. Sandini. Tactile sensing—from humans to humanoids. *IEEE transactions on robotics*, 26(1):1–20, 2009.
- [36] J. Dai and D. Kerr. A six-component contact force measurement device based on the stewart platform. *Proceedings of the Institution of Mechanical Engineers, Part C: Journal of Mechanical Engineering Science*, 214(5):687–697, 2000.

- [37] D. V. Dao, T. Toriyama, J. Wells, and S. Sugiyama. Six-degree of freedom micro force-moment sensor for application in geophysics. In *Technical Digest. MEMS 2002 IEEE International Conference. Fifteenth IEEE International Conference on Micro Electro Mechanical Systems (Cat. No. 02CH37266)*, pages 312–315. IEEE, 2002.
- [38] G. Darlinski, U. Böttger, R. Waser, H. Klauk, M. Halik, U. Zschieschang, G. Schmid, and C. Dehm. Mechanical force sensors using organic thin-film transistors. *Journal of applied physics*, 97(9):093708, 2005.
- [39] K. Dautenhahn, C. L. Nehaniv, M. L. Walters, B. Robins, H. Kose-Bagci, N. A. Mirza, and M. Blow. Kaspar—a minimally expressive humanoid robot for human–robot interaction research. *Applied Bionics and Biomechanics*, 6(3-4):369–397, 2009.
- [40] A. B. Dawood, H. Godaba, and K. Althoefer. Modelling of a soft sensor for exteroception and proprioception in a pneumatically actuated soft robot. In *Annual Conference Towards Autonomous Robotic Systems*, pages 99–110. Springer, 2019.
- [41] K. M. Deutsch and K. M. Newell. Noise, variability, and the development of children’s perceptual-motor skills. *Developmental Review*, 25(2):155–180, 2005.
- [42] S. Dong, W. Yuan, and E. H. Adelson. Improved gelsight tactile sensor for measuring geometry and slip. In *2017 IEEE/RSJ International Conference on Intelligent Robots and Systems (IROS)*, pages 137–144. IEEE, 2017.
- [43] E. Donlon, S. Dong, M. Liu, J. Li, E. Adelson, and A. Rodriguez. Gelslim: A high-resolution, compact, robust, and calibrated tactile-sensing finger. In *2018 IEEE/RSJ International Conference on Intelligent Robots and Systems (IROS)*, pages 1927–1934. IEEE, 2018.
- [44] V. Duchaine. Why tactile intelligence is the future of robotic grasping. *IEEE Spectrum: Blogs*, 2016.
- [45] O. Duran, K. Althoefer, and L. D. Seneviratne. Automated sewer pipe inspection through

- image processing. In *Proceedings 2002 IEEE International Conference on Robotics and Automation (Cat. No. 02CH37292)*, volume 3, pages 2551–2556. IEEE, 2002.
- [46] T. Dwarakanath, B. Dasgupta, and T. Mruthyunjaya. Design and development of a stewart platform based force–torque sensor. *Mechatronics*, 11(7):793–809, 2001.
- [47] C. Edussooriya, H. Hapuachchi, D. Rajiv, R. Ranasinghe, and S. Munasinghe. Analysis of grasping and slip detection of the human hand. In *2008 4th international conference on information and automation for sustainability*, pages 261–266. IEEE, 2008.
- [48] L. Feng, G. Lin, W. Zhang, H. Pang, and T. Wang. Design and optimization of a self-decoupled six-axis wheel force transducer for a heavy truck. *Proceedings of the Institution of Mechanical Engineers, Part D: Journal of Automobile Engineering*, 229(12):1585–1610, 2015.
- [49] C. Ferraresi, S. Pastorelli, and M. S. N. Zhmud'. State and dynamic behavior of a high stiffness stewart platform-based force/torque sensor. *Journal of robotic systems*, 12(12):883–893, 1995.
- [50] J. A. Fishel and G. E. Loeb. Sensing tactile microvibrations with the biotac—comparison with human sensitivity. In *2012 4th IEEE RAS & EMBS international conference on biomedical robotics and biomechatronics (BioRob)*, pages 1122–1127. IEEE, 2012.
- [51] M. Fontana, S. Marcheschi, F. Salsedo, and M. Bergamasco. A three-axis force sensor for dual finger haptic interfaces. *Sensors*, 12(10):13598–13616, 2012.
- [52] J. Fras and K. Althoefer. Soft biomimetic prosthetic hand: Design, manufacturing and preliminary examination. In *2018 IEEE/RSJ International Conference on Intelligent Robots and Systems (IROS)*, pages 1–6. IEEE, 2018.
- [53] E. Fujiwara, F. D. Paula, Y. T. Wu, M. F. Santos, E. A. Schenkel, and C. K. Suzuki. Optical fiber tactile sensor based on fiber specklegram analysis. In *2017 25th Optical Fiber Sensors Conference (OFS)*, pages 1–4. IEEE, 2017.

- [54] M. Gobbi, G. Previati, P. Guarneri, and G. Mastinu. A new six-axis load cell. part ii: error analysis, construction and experimental assessment of performances. *Experimental Mechanics*, 51(3):389–399, 2011.
- [55] D. M. Gorinevsky, A. M. Formalsky, and A. Y. Schneider. *Force control of robotics systems*. Formalskii Alexander, 1997.
- [56] D. Gouaillier, V. Hugel, P. Blazevic, C. Kilner, J. Monceaux, P. Lafourcade, B. Marnier, J. Serre, and B. Maisonnier. Mechatronic design of nao humanoid. In *2009 IEEE International Conference on Robotics and Automation*, pages 769–774. IEEE, 2009.
- [57] K. Grattan and T. Sun. Fiber optic sensor technology: an overview. *Sensors and Actuators A: Physical*, 82(1-3):40–61, 2000.
- [58] A. Gruebele, J.-P. Roberge, A. Zerbe, W. Ruotolo, T. M. Huh, and M. R. Cutkosky. A stretchable capacitive sensory skin for exploring cluttered environments. *IEEE Robotics and Automation Letters*, 5(2):1750–1757, 2020.
- [59] K. O. Hill and G. Meltz. Fiber bragg grating technology fundamentals and overview. *Journal of lightwave technology*, 15(8):1263–1276, 1997.
- [60] A. C. Holgado, J. A. A. Lopez, A. Schmitz, T. P. Tomo, S. Somlor, L. Jamone, and S. Sugano. An adjustable force sensitive sensor with an electromagnet for a soft, distributed, digital 3-axis skin sensor. In *2018 IEEE/RSJ International Conference on Intelligent Robots and Systems (IROS)*, pages 2582–2588. IEEE, 2018.
- [61] K. Hosoda, Y. Tada, and M. Asada. Anthropomorphic robotic soft fingertip with randomly distributed receptors. *Robotics and Autonomous Systems*, 54(2):104–109, 2006.
- [62] R. D. Howe. Tactile sensing and control of robotic manipulation. *Advanced Robotics*, 8(3):245–261, 1993.
- [63] C.-B. Hu, C. Zhang, X. Xie, J.-Y. He, et al. Real-time marker recognition using vision-based tactile sensor. In *2018 14th IEEE International Conference on Solid-State and Integrated Circuit Technology (ICSICT)*, pages 1–3. IEEE, 2018.

- [64] Y. Ito, Y. Kim, and G. Obinata. Robust slippage degree estimation based on reference update of vision-based tactile sensor. *IEEE Sensors Journal*, 11(9):2037–2047, 2011.
- [65] J. W. James, N. Pestell, and N. F. Lepora. Slip detection with a biomimetic tactile sensor. *IEEE Robotics and Automation Letters*, 3(4):3340–3346, 2018.
- [66] L. Jamone, L. Natale, G. Metta, and G. Sandini. Highly sensitive soft tactile sensors for an anthropomorphic robotic hand. *IEEE sensors Journal*, 15(8):4226–4233, 2015.
- [67] X. Jia, R. Li, M. A. Srinivasan, and E. H. Adelson. Lump detection with a gelsight sensor. In *2013 World Haptics Conference (WHC)*, pages 175–179. IEEE, 2013.
- [68] M. K. Johnson and E. H. Adelson. Retrographic sensing for the measurement of surface texture and shape. In *2009 IEEE Conference on Computer Vision and Pattern Recognition*, pages 1070–1077. IEEE, 2009.
- [69] M. K. Johnson, F. Cole, A. Raj, and E. H. Adelson. Microgeometry capture using an elastomeric sensor. *ACM Transactions on Graphics (TOG)*, 30(4):1–8, 2011.
- [70] K. Kamiyama, H. Kajimoto, N. Kawakami, and S. Tachi. Evaluation of a vision-based tactile sensor. In *IEEE International Conference on Robotics and Automation, 2004. Proceedings. ICRA'04. 2004*, volume 2, pages 1542–1547. IEEE, 2004.
- [71] K. Kamiyama, K. Vlack, T. Mizota, H. Kajimoto, K. Kawakami, and S. Tachi. Vision-based sensor for real-time measuring of surface traction fields. *IEEE Computer Graphics and Applications*, 25(1):68–75, 2005.
- [72] C.-G. Kang. Closed-form force sensing of a 6-axis force transducer based on the stewart platform. *Sensors and Actuators A: Physical*, 90(1-2):31–37, 2001.
- [73] A. Ke, J. Huang, L. Chen, Z. Gao, J. Han, C. Wang, J. Zhou, and J. He. Fingertip tactile sensor with single sensing element based on fsr and pvdf. *IEEE Sensors Journal*, 19(23):11100–11112, 2019.
- [74] C. C. Kemp, A. Edsinger, and E. Torres-Jara. Challenges for robot manipulation in hu-

- man environments [grand challenges of robotics]. *IEEE Robotics & Automation Magazine*, 14(1):20–29, 2007.
- [75] G.-S. Kim. Design of a six-axis wrist force/moment sensor using fem and its fabrication for an intelligent robot. *Sensors and Actuators A: Physical*, 133(1):27–34, 2007.
- [76] G.-S. Kim, D.-I. Kang, and S.-H. Rhee. Design and fabrication of a six-component force/moment sensor. *Sensors and Actuators A: Physical*, 77(3):209–220, 1999.
- [77] G.-S. Kim, D.-I. Kang, S.-H. Rhee, and K.-W. Um. Design and fabrication of a three-component force/moment sensor using plate-beams. *Measurement Science and Technology*, 10(4):295, 1999.
- [78] G.-S. Kim, H.-J. Shin, and J. Yoon. Development of 6-axis force/moment sensor for a humanoid robot’s intelligent foot. *Sensors and Actuators A: Physical*, 141(2):276–281, 2008.
- [79] M. Kimmerle, L. Mainwaring, and M. Borenstein. The functional repertoire of the hand and its application to assessment. *American Journal of Occupational Therapy*, 57(5):489–498, 2003.
- [80] S. Koh, B. Cho, J.-K. Park, C.-H. Kim, and S. Lee. A fundamental experiment on contact position estimation on vision based dome-type soft tactile sensor using ready-made medium. In *2019 13th International Conference on Sensing Technology (ICST)*, pages 1–5. IEEE, 2019.
- [81] J. Konstantinova, G. Cotugno, A. Stilli, Y. Noh, and K. Althoefer. Object classification using hybrid fiber optical force/proximity sensor. In *2017 IEEE SENSORS*, pages 1–3. IEEE, 2017.
- [82] J. Konstantinova, A. Stilli, and K. Althoefer. Force and proximity fingertip sensor to enhance grasping perception. In *2015 IEEE/RSJ International Conference on Intelligent Robots and Systems (IROS)*, pages 2118–2123. IEEE, 2015.

- [83] J. Konstantinova, A. Stilli, and K. Althoefer. Fingertip fiber optical tactile array with two-level spring structure. *Sensors*, 17(10):2337, 2017.
- [84] J. Krüger, T. K. Lien, and A. Verl. Cooperation of human and machines in assembly lines. *CIRP annals*, 58(2):628–646, 2009.
- [85] C. Lam, Y. Noh, M. Howard, S. Luo, S. Han, and K. Rhode. Human finger inspired grasping structure using tactile sensing array with single type optoelectronic sensor. In *2017 IEEE SENSORS*, pages 1–3. IEEE.
- [86] M. Lambeta, P.-W. Chou, S. Tian, B. Yang, B. Maloon, V. R. Most, D. Stroud, R. Santos, A. Byagowi, G. Kammerer, et al. Digit: A novel design for a low-cost compact high-resolution tactile sensor with application to in-hand manipulation. *IEEE Robotics and Automation Letters*, 5(3):3838–3845, 2020.
- [87] S. B. Lang and S. Muensit. Review of some lesser-known applications of piezoelectric and pyroelectric polymers. *Applied Physics A*, 85(2):125–134, 2006.
- [88] C. Laschi. Octobot-a robot octopus points the way to soft robotics. *IEEE Spectrum*, 54(3):38–43, 2017.
- [89] R. Lazzarini, R. Magni, and P. Dario. A tactile array sensor layered in an artificial skin. In *Proceedings 1995 IEEE/RSJ International Conference on Intelligent Robots and Systems. Human Robot Interaction and Cooperative Robots*, volume 3, pages 114–119. IEEE, 1995.
- [90] H.-K. Lee, J. Chung, S.-I. Chang, and E. Yoon. Normal and shear force measurement using a flexible polymer tactile sensor with embedded multiple capacitors. *Journal of Microelectromechanical Systems*, 17(4):934–942, 2008.
- [91] R. Li and E. H. Adelson. Sensing and recognizing surface textures using a gelsight sensor. In *Proceedings of the IEEE Conference on Computer Vision and Pattern Recognition*, pages 1241–1247, 2013.
- [92] R. Li, R. Platt, W. Yuan, A. ten Pas, N. Roscup, M. A. Srinivasan, and E. Adelson. Lo-

- calization and manipulation of small parts using gelsight tactile sensing. In *2014 IEEE/RSJ International Conference on Intelligent Robots and Systems*, pages 3988–3993. IEEE, 2014.
- [93] W. Li, J. Konstantinova, A. Alomainy, and K. Althoefer. Elastomer-based touch sensor: Visualization of tactile pressure distribution. In *Annual Conference Towards Autonomous Robotic Systems*, pages 87–98. Springer, 2019.
- [94] M. Liu, Y. Zhao, Y. Shao, Q. Zhang, and C. Liu. 3d printed force sensor with inkjet printed piezoresistive based strain gauge. In *2018 IEEE SENSORS*, pages 1–4. IEEE, 2018.
- [95] M. Luo, X. Luo, and C. Pan. A stewart platform-based 3-axis force sensor for robot fingers. In *2011 Second International Conference on Mechanic Automation and Control Engineering*, pages 37–40. IEEE, 2011.
- [96] D. Ma, E. Donlon, S. Dong, and A. Rodriguez. Dense tactile force estimation using gelslim and inverse fem. In *2019 International Conference on Robotics and Automation (ICRA)*, pages 5418–5424. IEEE, 2019.
- [97] V. Maheshwari and R. Saraf. Tactile devices to sense touch on a par with a human finger. *Angewandte Chemie International Edition*, 47(41):7808–7826, 2008.
- [98] P. Maiolino, F. Mastrogiovanni, G. Cannata, et al. Skinning a robot: design methodologies for large-scale robot skin. *IEEE Robotics & Automation Magazine*, 23(4):150–159, 2016.
- [99] S. C. Mannsfeld, B. C. Tee, R. M. Stoltenberg, C. V. H. Chen, S. Barman, B. V. Muir, A. N. Sokolov, C. Reese, and Z. Bao. Highly sensitive flexible pressure sensors with microstructured rubber dielectric layers. *Nature materials*, 9(10):859–864, 2010.
- [100] I. Manunza and A. Bonfiglio. Pressure sensing using a completely flexible organic transistor. *Biosensors and Bioelectronics*, 22(12):2775–2779, 2007.
- [101] I. Manunza, A. Sulis, and A. Bonfiglio. Pressure sensing by flexible, organic, field effect transistors. *Applied Physics Letters*, 89(14):143502, 2006.
- [102] W. Mason and R. Thurston. Use of piezoresistive materials in the measurement of

- displacement, force, and torque. *The Journal of the Acoustical Society of America*, 29(10):1096–1101, 1957.
- [103] G. Mastinu, M. Gobbi, and G. Previati. A new six-axis load cell. part i: Design. *Experimental mechanics*, 51(3):373–388, 2011.
- [104] S. Matyunin and O. Babaev. Fiber-optic sensor of tactile force for anthropomorphic robot grips. In *IOP Conference Series: Materials Science and Engineering*, volume 302, page 012040. IOP Publishing, 2018.
- [105] S. J. Mihailov. Fiber bragg grating sensors for harsh environments. *Sensors*, 12(2):1898–1918, 2012.
- [106] A. Mohammadi, Y. Xu, Y. Tan, P. Choong, and D. Oetomo. Magnetic-based soft tactile sensors with deformable continuous force transfer medium for resolving contact locations in robotic grasping and manipulation. *Sensors*, 19(22):4925, 2019.
- [107] Y. Noh, J. Bimbo, S. Sareh, H. Wurdemann, J. Fraś, D. S. Chathuranga, H. Liu, J. Housden, K. Althoefer, and K. Rhode. Multi-axis force/torque sensor based on simply-supported beam and optoelectronics. *Sensors*, 16(11):1936, 2016.
- [108] Y. Noh, L. Lindenroth, S. Wang, R. J. Housden, A. Wingerden, W. Li, and K. Rhode. A2-piece six-axis force/torque sensor capable of measuring loads applied to tools of complex shapes. In *IEEE International Conference on Intelligent Robots and Systems*, volume 2019, pages 7976–7981. IEEE, 2020.
- [109] Y. Noh, H. Liu, S. Sareh, D. S. Chathuranga, H. Würdemann, K. Rhode, and K. Althoefer. Image-based optical miniaturized three-axis force sensor for cardiac catheterization. *IEEE Sensors Journal*, 16(22):7924–7932, 2016.
- [110] Y. Noh, S. Sareh, J. Back, H. A. Würdemann, T. Ranzani, E. L. Secco, A. Faragasso, H. Liu, and K. Althoefer. A three-axial body force sensor for flexible manipulators. In *2014 IEEE International Conference on Robotics and Automation (ICRA)*, pages 6388–6393. IEEE, 2014.

- [111] Y. Noh, S. Sareh, H. Würdemann, H. Liu, J. Back, J. Housden, K. Rhode, and K. Althoefer. Three-axis fiber-optic body force sensor for flexible manipulators. *IEEE Sensors Journal*, 16(6):1641–1651, 2015.
- [112] M. Ohka, H. Kobayashi, J. Takata, and Y. Mitsuya. Sensing precision of an optical three-axis tactile sensor for a robotic finger. In *ROMAN 2006-The 15th IEEE International Symposium on Robot and Human Interactive Communication*, pages 214–219. IEEE, 2006.
- [113] M. Ohka, Y. Mitsuya, I. Higashioka, and H. Kabeshita. An experimental optical three-axis tactile sensor for micro-robots. *Robotica*, 23(4):457–465, 2005.
- [114] M. Ohka, Y. Mitsuya, S. Takeuchi, H. Ishihara, and O. Kamekawa. A three-axis optical tactile sensor (fem contact analyses and sensing experiments using a large-sized tactile sensor). In *Proceedings of 1995 IEEE International Conference on Robotics and Automation*, volume 1, pages 817–824. IEEE, 1995.
- [115] M. Ohka, Y. Yamamoto, H. Yussof, and S. C. Abdullah. All-in-type optical three-axis tactile sensor. In *2014 IEEE International Symposium on Robotics and Manufacturing Automation (ROMA)*, pages 74–79. IEEE, 2014.
- [116] R. Ouyang and R. Howe. Low-cost fiducial-based 6-axis force-torque sensor. *arXiv preprint arXiv:2005.14250*, 2020.
- [117] G. Palli, L. Moriello, U. Scarcia, and C. Melchiorri. Development of an optoelectronic 6-axis force/torque sensor for robotic applications. *Sensors and Actuators A: Physical*, 220:333–346, 2014.
- [118] T. V. Papakostas, J. Lima, and M. Lowe. A large area force sensor for smart skin applications. In *SENSORS, 2002 IEEE*, volume 2, pages 1620–1624. IEEE, 2002.
- [119] K. E. Pennywitt. Robotic tactile sensing. *Byte, Jan*, 14, 1986.
- [120] N. Pestell, J. Lloyd, J. Rossiter, and N. F. Lepora. Dual-modal tactile perception and exploration. *IEEE Robotics and Automation Letters*, 3(2):1033–1040, 2018.

- [121] T. Q. Pham, T. Hoshi, Y. Tanaka, and A. Sano. Effect of 3d microstructure of dermal papillae on sed concentration at a mechanoreceptor location. *Plos one*, 12(12):e0189293, 2017.
- [122] H.-P. Phan, D. V. Dao, K. Nakamura, S. Dimitrijevic, and N.-T. Nguyen. The piezoresistive effect of sic for mems sensors at high temperatures: a review. *Journal of Microelectromechanical systems*, 24(6):1663–1677, 2015.
- [123] J. P. Piek, G. B. Baynam, and N. C. Barrett. The relationship between fine and gross motor ability, self-perceptions and self-worth in children and adolescents. *Human movement science*, 25(1):65–75, 2006.
- [124] J. P. Piek, L. Dawson, L. M. Smith, and N. Gasson. The role of early fine and gross motor development on later motor and cognitive ability. *Human movement science*, 27(5):668–681, 2008.
- [125] K. Pont, M. Wallen, A. Bundy, and J. Case-Smith. Reliability and validity of the test of in-hand manipulation in children ages 5 to 6 years. *American Journal of Occupational Therapy*, 62(4):384–392, 2008.
- [126] P. Puangmali, K. Althoefer, L. D. Seneviratne, D. Murphy, and P. Dasgupta. State-of-the-art in force and tactile sensing for minimally invasive surgery. *IEEE Sensors Journal*, 8(4):371–381, 2008.
- [127] J. A. C. Ramón, F. T. Medina, and V. Perdereau. Finger readjustment algorithm for object manipulation based on tactile information. *International Journal of Advanced Robotic Systems*, 10(1):9, 2013.
- [128] R. Ranganath, P. Nair, T. Mruthyunjaya, and A. Ghosal. A force–torque sensor based on a stewart platform in a near-singular configuration. *Mechanism and machine theory*, 39(9):971–998, 2004.
- [129] J. F. Rauthmann, D. Gallardo-Pujol, E. M. Guillaume, E. Todd, C. S. Nave, R. A. Sherman, M. Ziegler, A. B. Jones, and D. C. Funder. The situational eight diamonds: A tax-

- onomy of major dimensions of situation characteristics. *Journal of Personality and Social Psychology*, 107(4):677, 2014.
- [130] R. A. Romeo and L. Zollo. Methods and sensors for slip detection in robotics: A survey. *IEEE Access*, 8:73027–73050, 2020.
- [131] A. Romiti and M. Sorli. Force and moment measurement on a robotic assembly hand. *Sensors and Actuators A: Physical*, 32(1-3):531–538, 1992.
- [132] T. Sakuma, F. Von Drigalski, M. Ding, J. Takamatsu, and T. Ogasawara. A universal gripper using optical sensing to acquire tactile information and membrane deformation. In *2018 IEEE/RSJ International Conference on Intelligent Robots and Systems (IROS)*, pages 1–9. IEEE, 2018.
- [133] X. Y. Sandoval-Castro, M. A. Gracia-Murillo, J. P. Zavala-De Paz, and E. Castillo-Castaneda. Hex-piderix: A six-legged walking climbing robot to perform inspection tasks on vertical surfaces. In *Nature-Inspired Mobile Robotics*, pages 399–407. World Scientific, 2013.
- [134] R. Sargeant, H. Liu, L. D. Seneviratne, and K. Althoefer. An optical multi-axial force/torque sensor for dexterous grasping and manipulation. In *2012 IEEE International Conference on Multisensor Fusion and Integration for Intelligent Systems (MFI)*, pages 144–149. IEEE, 2012.
- [135] R. Sargeant, L. D. Seneviratne, and K. Althoefer. A 2-axis optical force–torque fingertip sensor for dexterous grasping using linear polarizers. *IEEE Transactions on Instrumentation and Measurement*, 61(12):3363–3377, 2012.
- [136] K. Sato, K. Kamiyama, N. Kawakami, and S. Tachi. Finger-shaped gelforce: sensor for measuring surface traction fields for robotic hand. *IEEE Transactions on Haptics*, 3(1):37–47, 2009.
- [137] V. D. Scheinman. Design of a computer controlled manipulator. Technical report, Stanford Univ Calif Dept of Computer Science, 1969.

- [138] A. Schmitz, M. Maggiali, M. Randazzo, L. Natale, and G. Metta. A prototype fingertip with high spatial resolution pressure sensing for the robot icub. In *Humanoids 2008-8th IEEE-RAS International Conference on Humanoid Robots*, pages 423–428. IEEE, 2008.
- [139] J. L. Schneider and T. B. Sheridan. An optical tactile sensor for manipulators. *Robotics and computer-integrated manufacturing*, 1(1):65–71, 1984.
- [140] U. Seibold, B. Kubler, and G. Hirzinger. Prototype of instrument for minimally invasive surgery with 6-axis force sensing capability. In *Proceedings of the 2005 IEEE International Conference on Robotics and Automation*, pages 496–501. IEEE, 2005.
- [141] W. Shi and S. D. Hall. A novel six axis force sensor for measuring the loading of a racing tyre on track. In *Proceedings of the First International Conference on Sensing Technology*. Citeseer, 2005.
- [142] M. Sorli and N. Zhmud. Investigation of force and moment measurement system for a robotic assembly hand. *Sensors and Actuators A: Physical*, 37:651–657, 1993.
- [143] R. J. Stein, W. M. White, R. K. Goel, B. H. Irwin, G. P. Haber, and J. H. Kaouk. Robotic laparoendoscopic single-site surgery using gelport as the access platform. *European urology*, 57(1):132–137, 2010.
- [144] C. Steinem and A. Janshoff. *Piezoelectric sensors*, volume 5. Springer Science & Business Media, 2007.
- [145] R. J. Stephen, K. Rajanna, V. Dhar, K. K. Kumar, and S. Nagabushanam. Thin-film strain gauge sensors for ion thrust measurement. *IEEE sensors journal*, 4(3):373–377, 2004.
- [146] D. Stewart. A platform with six degrees of freedom. *Proceedings of the institution of mechanical engineers*, 180(1):371–386, 1965.
- [147] J. Summers, D. Larkin, and D. Dewey. Activities of daily living in children with developmental coordination disorder: dressing, personal hygiene, and eating skills. *Human movement science*, 27(2):215–229, 2008.

- [148] Y. Sun, Y. Liu, M. Jin, and H. Liu. Design and optimization of a novel six-axis force/torque sensor with good isotropy and high sensitivity. In *2013 IEEE International Conference on Robotics and Biomimetics (ROBIO)*, pages 631–638. IEEE, 2013.
- [149] S. Takamuku, G. Gomez, K. Hosoda, and R. Pfeifer. Haptic discrimination of material properties by a robotic hand. In *2007 IEEE 6th International Conference on Development and Learning*, pages 1–6. IEEE, 2007.
- [150] J. O. Templeman, B. B. Sheil, and T. Sun. Multi-axis force sensors: A state-of-the-art review. *Sensors and Actuators A: Physical*, 304:111772, 2020.
- [151] G. Tholey and J. P. Desai. A compact and modular laparoscopic grasper with tridirectional force measurement capability. *Journal of Medical Devices*, 2(3), 2008.
- [152] M. I. Tiwana, S. J. Redmond, and N. H. Lovell. A review of tactile sensing technologies with applications in biomedical engineering. *Sensors and Actuators A: physical*, 179:17–31, 2012.
- [153] L. Torsi, M. Magliulo, K. Manoli, and G. Palazzo. Organic field-effect transistor sensors: a tutorial review. *Chemical Society Reviews*, 42(22):8612–8628, 2013.
- [154] C. Trueeb, C. Sferrazza, and R. D’Andrea. Towards vision-based robotic skins: a data-driven, multi-camera tactile sensor. In *2020 3rd IEEE International Conference on Soft Robotics (RoboSoft)*, pages 333–338. IEEE, 2020.
- [155] J. Ueda, Y. Ishida, M. Kondo, and T. Ogasawara. Development of the naist-hand with vision-based tactile fingertip sensor. In *Proceedings of the 2005 IEEE International Conference on Robotics and Automation*, pages 2332–2337. iee, 2005.
- [156] P. Valdastri, S. Roccella, L. Beccai, E. Cattin, A. Menciassi, M. Carrozza, and P. Dario. Characterization of a novel hybrid silicon three-axial force sensor. *Sensors and Actuators A: Physical*, 123:249–257, 2005.
- [157] H. Van Brussel, I. H. Belien, and I. H. Thielemans. Force sensing for advanced robot control. *Robotics*, 2(2):139–148, 1986.

- [158] J. F. Veneman, R. Kruidhof, E. E. Hekman, R. Ekkelenkamp, E. H. Van Asseldonk, and H. Van Der Kooij. Design and evaluation of the lopes exoskeleton robot for interactive gait rehabilitation. *IEEE Transactions on Neural Systems and Rehabilitation Engineering*, 15(3):379–386, 2007.
- [159] S. Wang, K.-H. Huang, and Y.-J. Yang. A highly sensitive capacitive pressure sensor with microdome structure for robot tactile detection. In *2019 20th International Conference on Solid-State Sensors, Actuators and Microsystems & Eurosensors XXXIII (TRANSDUCERS & EUROSENSORS XXXIII)*, pages 458–461. IEEE, 2019.
- [160] B. Ward-Cherrier, N. Pestell, L. Cramphorn, B. Winstone, M. E. Giannaccini, J. Rossiter, and N. F. Lepora. The tactip family: Soft optical tactile sensors with 3d-printed biomimetic morphologies. *Soft robotics*, 5(2):216–227, 2018.
- [161] H. Wei, Y. Cai, H. Li, D. Li, and T. Wang. Sambot: A self-assembly modular robot for swarm robot. In *2010 IEEE International Conference on Robotics and Automation*, pages 66–71. IEEE, 2010.
- [162] K. Weiß and H. Worn. The working principle of resistive tactile sensor cells. In *IEEE International Conference Mechatronics and Automation, 2005*, volume 1, pages 471–476. IEEE, 2005.
- [163] P. M. Wensing, A. Wang, S. Seok, D. Otten, J. Lang, and S. Kim. Proprioceptive actuator design in the mit cheetah: Impact mitigation and high-bandwidth physical interaction for dynamic legged robots. *IEEE Transactions on Robotics*, 33(3):509–522, 2017.
- [164] N. Wettels, J. A. Fishel, and G. E. Loeb. Multimodal tactile sensor. In *The Human Hand as an Inspiration for Robot Hand Development*, pages 405–429. Springer, 2014.
- [165] N. Wettels, V. J. Santos, R. S. Johansson, and G. E. Loeb. Biomimetic tactile sensor array. *Advanced Robotics*, 22(8):829–849, 2008.
- [166] B. Winstone, G. Griffiths, C. Melhuish, T. Pipe, and J. Rossiter. Tactip—tactile fingertip device, challenges in reduction of size to ready for robot hand integration. In *2012 IEEE*

- International Conference on Robotics and Biomimetics (ROBIO)*, pages 160–166. IEEE, 2012.
- [167] B. Winstone, G. Griffiths, T. Pipe, C. Melhuish, and J. Rossiter. Tactip-tactile fingertip device, texture analysis through optical tracking of skin features. In *Conference on Biomimetic and Biohybrid Systems*, pages 323–334. Springer, 2013.
- [168] B. Wu and P. Cai. Decoupling analysis of a sliding structure six-axis force/torque sensor. *Measurement Science Review*, 13(4):187–193, 2013.
- [169] X. Wu and J. Huang. Array of organic field-effect transistor for advanced sensing. *IEEE journal on emerging and selected topics in circuits and systems*, 7(1):92–101, 2016.
- [170] H. Xie, A. Jiang, H. A. Wurdemann, H. Liu, L. D. Seneviratne, and K. Althoefer. Magnetic resonance-compatible tactile force sensor using fiber optics and vision sensor. *IEEE Sensors Journal*, 14(3):829–838, 2013.
- [171] L. Xiong, G. Jiang, Y. Guo, and H. Liu. A three-dimensional fiber bragg grating force sensor for robot. *IEEE Sensors Journal*, 18(9):3632–3639, 2018.
- [172] Y. Xu, F. Jiang, S. Newbern, A. Huang, C.-M. Ho, and Y.-C. Tai. Flexible shear-stress sensor skin and its application to unmanned aerial vehicles. *Sensors and Actuators A: Physical*, 105(3):321–329, 2003.
- [173] Z. Xu and E. Todorov. Design of a highly biomimetic anthropomorphic robotic hand towards artificial limb regeneration. In *2016 IEEE International Conference on Robotics and Automation (ICRA)*, pages 3485–3492. IEEE, 2016.
- [174] T. Yoshino, K. Kurosawa, K. Itoh, and T. Ose. Fiber-optic fabry-perot interferometer and its sensor applications. *IEEE Transactions on Microwave Theory and Techniques*, 30(10):1612–1621, 1982.
- [175] H. Yousef, M. Boukallel, and K. Althoefer. Tactile sensing for dexterous in-hand manipulation in robotics—a review. *Sensors and Actuators A: physical*, 167(2):171–187, 2011.

- [176] W. Yuan, S. Dong, and E. H. Adelson. Gelsight: High-resolution robot tactile sensors for estimating geometry and force. *Sensors*, 17(12):2762, 2017.
- [177] W. Yuan et al. *Tactile measurement with a gelsight sensor*. PhD thesis, Massachusetts Institute of Technology, 2014.
- [178] W. Yuan, R. Li, M. A. Srinivasan, and E. H. Adelson. Measurement of shear and slip with a gelsight tactile sensor. In *2015 IEEE International Conference on Robotics and Automation (ICRA)*, pages 304–311. IEEE, 2015.
- [179] W. Yuan, Y. Mo, S. Wang, and E. H. Adelson. Active clothing material perception using tactile sensing and deep learning. In *2018 IEEE International Conference on Robotics and Automation (ICRA)*, pages 1–8. IEEE, 2018.
- [180] W. Yuan, M. A. Srinivasan, and E. H. Adelson. Estimating object hardness with a gelsight touch sensor. In *2016 IEEE/RSJ International Conference on Intelligent Robots and Systems (IROS)*, pages 208–215. IEEE, 2016.
- [181] J. Zhenlin, G. Feng, and Z. Xiaohui. Design and analysis of a novel isotropic six-component force/torque sensor. *Sensors and Actuators A: Physical*, 109(1-2):17–20, 2003.